

# Measurement of the Coulomb dissociation cross sections of the neutron rich nitrogen isotopes $^{20,21}\text{N}$

## DISSERTATION

zur Erlangung des akademischen Grades

**Doctor rerum naturalium**

(Dr. rer. nat.)

vorgelegt

der Fakultät Mathematik und Naturwissenschaften

der Technischen Universität Dresden

von

**Dipl.-Phys. Marko Röder**

geboren am 08.01.1984 in Wolfen

Erster Gutachter: Professor Dr. Kai Zuber

Zweiter Gutachter: Professor Dr. Thomas Aumann

Tag der Einreichung: 03.07.2014

Tag der Verteidigung: 28.11.2014

---

---

## Abstract

Many neutron rich nuclei are involved in the astrophysical r-process (rapid neutron capture process). The r-process forms an important path for heavy element nucleosynthesis and runs along the neutron drip line. Astrophysicists suggested core-collapse supernovae within a neutrino-driven wind scenario where the neutrino wind dissociates all previously formed elements into protons, neutrons and  $\alpha$  particles, to be a possible astrophysical scenario for the r-process. Furthermore, reaction network calculations reported a high impact of light neutron rich nuclei to the r-process abundance. Reactions on these exotic nuclei can only be studied with radioactive ion beams as their half lives, in the order of a few hundred milliseconds ( $T_{1/2,^{19}\text{N}}=330\text{ ms}$ ), are too low to fabricate target material out of them.

Two examples of reactions along the path of the r-process are the  $^{19}\text{N}(n,\gamma)^{20}\text{N}$  and the  $^{20}\text{N}(n,\gamma)^{21}\text{N}$  reactions. Using  $^{20}\text{N}$  (resp.  $^{21}\text{N}$ ) as a beam, these reactions were studied at the GSI Fragment Separator (FRS) in time-reversed conditions via Coulomb dissociation in the S393 experiment exploiting the virtual gamma field of a lead target. The experiment was performed at the LAND/R3B setup (Large Area Neutron Detector, Reactions with Relativistic Radioactive Beams) in a kinematically complete measurement, i.e., detecting all particles leaving the nuclear reaction.

The neutrons flying at relativistic velocity were observed by the LAND detector, the calibration of which plays a crucial role for the present reaction. The Smiley effect, meaning that the measured energy of impinging particles in long scintillators is not independent of the hit position of the particle, has been investigated. It will be shown that reflections of the light traveling through the scintillator and the resulting longer path length of the light when not emitted directly towards the ends of the bar were identified to cause the Smiley effect.

Gamma spectra in coincidence with outgoing  $^{19}\text{N}$  (resp.  $^{20}\text{N}$ ) were generated. These fit well to recent publications and were utilized to separate transitions of the projectile nucleus into the ground state or first excited state of the ejectile nucleus. The Coulomb dissociation cross section was calculated for the total reaction, transitions into the ground state and the first excited state of the ejectile nucleus. Furthermore, excitation energy spectra were derived for both reactions separately for ground state transitions and for the dominating transitions into the first excited state.

In order to facilitate future experiments on exotic nuclei, two detector solutions for the NeuLAND detector (the successor of LAND) were investigated. Utilizing minimum ionizing electrons of 30 MeV at the ELBE facility, time resolutions and detection efficiencies were studied for an MRPC (Multi-gap Resistive Plate Chamber) based neutron detector with passive iron converters, on the one hand, and a pure scintillator based neutron ToF detector on the other hand. The ELBE data show good time resolutions ( $\sigma_{t,\text{electron}} \leq 120\text{ ps}$ ) and detection efficiencies ( $\epsilon_{\text{electron}} \geq 90\%$ ) for both systems. Small MRPC prototypes were irradiated with 175 MeV quasi-monochromatic neutrons at The Svedberg Laboratory (TSL) in Uppsala measuring efficiencies of  $\epsilon_{\text{MRPC,neutron}} \approx 1.0\%$ . It will be shown that MRPCs with passive steel converters may be included as neutron detectors in experiments where a lower multi-neutron capability than the one needed for NeuLAND is sufficient.

---

## Zusammenfassung

Viele neutronenreiche Kerne sind im schnellen Neutroneneinfangprozess (r-Prozess, engl. für rapid) involviert. Der r-Prozess bildet einen wichtigen Pfad für die Nukleosynthese schwerer Elemente und verläuft entlang der Neutronen-Dripline. Astrophysiker schlugen Kernkollaps-Supernovae innerhalb eines neutrinogetriebenen Windes als mögliches astrophysikalisches Szenario für den r-Prozess vor. Dabei werden alle zuvor gebildeten Elemente in Protonen, Neutronen und Alphapartikel dissoziiert. Außerdem ist von Berechnungen mit Reaktionsnetzwerken bekannt, dass leichte neutronenreiche Kerne einen hohen Einfluss auf die Elementverteilung des r-Prozesses haben. Reaktionen dieser exotischen Kerne können nur mit radioaktiven Ionenstrahlen studiert werden, da ihre Halbwertszeiten im Bereich von wenigen hundert Millisekunden ( $T_{1/2,^{19}\text{N}}=330\text{ ms}$ ) zu gering sind, um Probenmaterial daraus herzustellen.

Zwei Beispiele solcher Reaktionen, die auf dem Pfad des r-Prozesses liegen, sind die  $^{19}\text{N}(n,\gamma)^{20}\text{N}$  und die  $^{20}\text{N}(n,\gamma)^{21}\text{N}$  Reaktionen. Unter Verwendung von  $^{20}\text{N}$  (bzw.  $^{21}\text{N}$ ) als Strahl wurden diese Reaktionen am Fragment Separator (FRS) der GSI unter zeitumgekehrten Bedingungen mittels Coulomb-Aufbruch gemessen, indem das virtuelle Photonenfeld einer Bleiprobe ausgenutzt wurde. Das Experiment wurde am LAND/R3B Aufbau (Large Area Neutron Detector, Reactions with Relativistic Radioactive Beams) in einer kinematisch vollständigen Messung durchgeführt, d.h. alle ausgehenden Reaktionsprodukte wurden detektiert.

Die relativistischen Neutronen wurden mit dem LAND-Detektor untersucht. Dessen Kalibration spielt eine wichtige Rolle für die hier analysierten Reaktionen. Dabei wurde der Smiley-Effekt studiert, welcher beinhaltet, dass die gemessene Energie von einfallenden Teilchen mittels langen Szintillatorstreifen nicht unabhängig von der Position ist, an der die Teilchen auf den Detektor treffen. Es wird gezeigt, dass Reflexionen des Lichtes beim Durchgang durch den Szintillator und die größere Weglänge, die das Licht zurücklegen muss, wenn es nicht direkt in Richtung der Enden des Szintillators emittiert wird, den Smiley-Effekt verursachen.

Gamma-Spektren in Koinzidenz mit ausgehenden  $^{19}\text{N}$  (bzw.  $^{20}\text{N}$ ) wurden gewonnen und stimmen gut mit früheren Veröffentlichungen überein. Diese Spektren wurden dazu verwendet, die Übergänge des Projektilkerns in den Grundzustand und den ersten angeregten Zustand des Ejektilkerns zu identifizieren. Die Wirkungsquerschnitte des Coulombaufbruchs der Projektilkerne und die Anregungsenergiespektren beider Reaktionen wurden berechnet und separiert in Übergänge in den Grundzustand und die dominierenden Übergänge in den ersten angeregten Zustand.

Um künftige Experimente an exotischen Kernen zu ermöglichen, wurden zusätzlich zwei Detektorkonzepte für NeuLAND (Nachfolger von LAND) untersucht. Mit minimal ionisierenden Elektronen mit Energien von 30 MeV aus dem Elektronenbeschleuniger ELBE wurden die Zeitauflösungen und Detektionseffizienzen zum einen für einen MRPC (Multi-gap Resistive Plate Chamber) basierenden Neutronendetektor mit passiven Stahlkonverter und zum anderen für einen reinen szintillatorbasierenden Neutronendetektor studiert. Die ELBE-Daten zeigen gute Zeitauflösungen ( $\sigma_{t,\text{electron}} \leq 120\text{ ps}$ ) und Detektionseffizienzen ( $\epsilon_{\text{electron}} \geq 90\%$ ) für beide Systeme. Kleine MRPC-Prototypen wurden mit quasi-monochromatischen Neutronen mit einer Energie von 175 MeV am TSL (The Svedberg Laboratory) in Uppsala bestrahlt. Dabei wurden Effizienzen von  $\epsilon_{\text{MRPC,neutron}} \approx 1.0\%$  gemessen. Es wird gezeigt, dass MRPCs mit passiven Stahlkonvertern als Neutronendetektoren bei Experimenten, bei denen eine geringere Multineutronenfähigkeit als für NeuLAND ausreichend ist, eingesetzt werden können.

---

Parts of the data presented in section 2, i.e. in the subsections 2.2.1 and 2.2.2 have already been published in a peer-reviewed journal:

**M. Röder**, Z. Elekes, T. Aumann, D. Bemmerer, K. Boretzky, C. Caesar, T.E. Cowan, J. Hehner, M. Heil, M. Kempe, V. Maroussov, O. Nusair, A. V. Prokofiev, M. Sobiella, R. Reifarth, D. Stach, A. Wagner, D. Yakorev, A. Zilges, and K. Zuber for the R3B collaboration

*Efficiency determination of resistive plate chambers for fast quasi-monoenergetic neutrons*  
European Physical Journal, Volume 50, Issue 7, pp. 112 (2014)

DOI: 10.1140/epja/i2014-14112-0

**M. Röder**, T. Aumann, D. Bemmerer, K. Boretzky, C. Caesar, T.E. Cowan, J. Hehner, M. Heil, Z. Elekes, M. Kempe, V. Maroussov, T.P. Reinhardt, H. Simon, M. Sobiella, D. Stach, A. Wagner, J. Wüstenfeld, D. Yakorev, A. Zilges, and K. Zuber for the R3B collaboration

*Prototyping a  $2\text{ m} \times 0.5\text{ m}$  MRPC-based neutron TOF-wall with steel converter plates*  
Journal of Instrumentation, Volume 7, Issue 11, pp. P11030 (2012)

DOI: 10.1088/1748-0221/7/11/P11030

This work was supported in part by GSI F&E (DR-ZUBE), NupNET NEDENSAA (05 P09 CRFN5), and Plattform für Detektortechnologie und -systeme.

---

# Contents

<b>1</b>	<b>Motivation – Nucleosynthesis processes</b>	<b>9</b>
<b>2</b>	<b>Development Work for NeuLAND</b>	<b>11</b>
2.1	General Design Goals . . . . .	11
2.2	MRPC Concept . . . . .	11
2.2.1	Tests of Small MRPC Prototypes with 175 MeV Neutrons . . . . .	13
2.2.2	Tests of Large MRPC Prototypes at ELBE . . . . .	20
2.3	Scintillator Concept . . . . .	25
2.4	Summary and Conclusion . . . . .	29
<b>3</b>	<b>Experimental Methods &amp; Techniques at the LAND/R3B Setup</b>	<b>33</b>
3.1	Radioactive Ion Beam Production at the FRS . . . . .	33
3.2	Overview of the LAND/R3B-Setup . . . . .	36
3.3	Detectors for Identifying the Incoming Particles . . . . .	36
3.3.1	S8 at FRS . . . . .	37
3.3.2	POS . . . . .	38
3.3.3	PSP . . . . .	38
3.3.4	ROLU . . . . .	39
3.3.5	DSSSD . . . . .	39
3.4	Reaction Targets . . . . .	40
3.5	Detectors for Identifying the Reaction Products . . . . .	40
3.5.1	DSSSD . . . . .	40
3.5.2	NaI Crystal Ball . . . . .	40
3.5.3	ALADIN . . . . .	41
3.5.4	GFI . . . . .	41
3.5.5	TFW . . . . .	41
3.5.6	LAND . . . . .	42
3.5.7	land02 Framework . . . . .	43
3.5.8	Calibration Procedures of Long Scintillators . . . . .	43
3.6	Energy Measurement in Long Scintillators – The Smiley-Effect . . . . .	46
3.6.1	Light Attenuation in Scintillators . . . . .	46
3.6.2	Extracting Energy and Position of Impinging Cosmic Muons . . . . .	47
3.6.3	Simple Smiley Calculations in 2D . . . . .	48
3.6.4	Conclusion and Discussion . . . . .	49
<b>4</b>	<b>Data Analysis for <math>^{20}\text{N}(\gamma, n)^{19}\text{N}</math> Reaction</b>	<b>53</b>
4.1	Incoming Particle Identification . . . . .	53
4.2	Identifying the Charge of the Outgoing Particle . . . . .	54
4.3	Exclude Scattered Neutron Hits in LAND . . . . .	55
4.4	Empirical Identification of the Outgoing Fragment Masses . . . . .	56
4.5	Outgoing Particle Identification by the Generic Tracker . . . . .	61
4.5.1	Calibration of the Detector Positions . . . . .	61
4.5.2	Checking the Calibration of the Tracker . . . . .	64
4.5.3	Mass Distribution derived by the Tracker . . . . .	66
4.6	Comparison of the two Methods for Mass Identification . . . . .	67
4.7	LAND Efficiency Correction . . . . .	68
4.8	Gamma Spectra . . . . .	70

4.9	Coulomb Dissociation Cross Section . . . . .	73
4.9.1	Data Normalization and Reaction Probabilities . . . . .	73
4.9.2	Scaling Factor . . . . .	74
4.9.3	Error Estimation . . . . .	76
4.9.4	Results of the Coulomb Dissociation Cross Section . . . . .	76
4.10	Excitation Energy Spectrum . . . . .	79
4.11	Discussion . . . . .	80
4.12	Photo Absorption and Neutron Capture Cross Section . . . . .	83
<b>5</b>	<b>Data Analysis for <math>^{21}\text{N}(\gamma, n)^{20}\text{N}</math> reaction</b>	<b>85</b>
5.1	Gamma Spectra . . . . .	86
5.2	Coulomb Excitation Cross Section . . . . .	88
5.2.1	Data Normalization and Reaction Probabilities . . . . .	88
5.2.2	Scaling Factor . . . . .	88
5.2.3	Error Estimation . . . . .	88
5.2.4	Results of the Coulomb Excitation Cross Section . . . . .	89
5.3	Excitation Energy Spectrum . . . . .	91
5.4	Discussion . . . . .	91
5.5	Photo Absorption and Neutron Capture Cross Section . . . . .	95



# 1 Motivation – Nucleosynthesis processes

One of the major questions nuclear astrophysics deals with is: How were the chemical elements created? So far, several processes were identified which contribute to an answer of this question. But they are not yet understood that well to explain the observed abundance of the elements on earth, in the entire solar system or in our galaxy.

The earliest process of the creation of the elements was fusion during Big Bang nucleosynthesis. Here, 75 % H, 25 % He and traces of Li and Be were created. Later on, heavier elements up to iron were formed by fusion in stars. As fusion of heavier elements is hindered by the Coulomb-barrier and by energetics of the reactions, elements heavier than iron can only be formed by neutron capture processes. These can be separated into two types.

In the slow neutron capture process (s-process) a neutron is captured by a stable nucleus (A), until becoming unstable (B) and undergoing beta-minus decay into a stable nucleus with higher proton number (C). The newly formed nucleus (C) has higher mass and proton number than the mother nucleus before the neutron was captured (A). After this beta decay, another neutron is captured and the process continues. Typical timescales are 100 years for one neutron capture and 1 minute for the beta decay. Thus, the beta decay occurs almost always before another neutron can be captured. That is where its name, slow neutron capture, comes from. Accordingly, the path of the s-process leads along the neutron rich side of the valley of stability. Passing decades between successive neutron capture processes, the time scale of the s-process is believed to be of thousands of years [1]. In this way, many of the elements heavier than iron can be built up subsequently. This process takes place in sites with a low neutron density (up to  $n_n = 10^{10} \text{ cm}^{-3}$ ) and intermediate temperature (0.1 GK) [1], i.e. Asymptotic Giant Branch stars (AGB stars), while stellar winds and supernovae may lead to the emission of the created s-process elements. But there are limits for the s-process. If beta-minus decaying unstable nuclei surround a stable nucleus (e.g.  $^{82}\text{Se}$  surrounded by  $^{81}\text{Se}$  and  $^{82}\text{Br}$  or  $^{104}\text{Ru}$  surrounded by  $^{103}\text{Ru}$  and  $^{104}\text{Rh}$ ) they form a kind of gap, the s-process can hardly bridge. Therefore, the s-process ends at  $^{209}\text{Bi}$ , not being able to explain the abundance of, e.g., the stable  $^{82}\text{Se}$ ,  $^{104}\text{Ru}$ ,  $^{124}\text{Sn}$ , or all radioactive elements like uranium and thorium.

The second neutron capture process is the rapid neutron capture process (r-process) taking place at high neutron densities of  $n_n > 10^{20}$  neutrons per  $\text{cm}^3$  and high ambient temperatures of 1 GK [1]. Here, the neutron density is high enough, that after one neutron was captured by a nucleus, another neutron is captured before the nucleus can undergo beta-minus decay. That means the neutron capture rate is higher than the rate of the beta-minus decay (the origin of “rapid”). After the beta decay, the nucleus is still unstable but having a higher half life than the previous one, so it might capture more neutrons as long as its half life becomes too small again. Thus, all heavier elements, even the radioactive ones, can be created independently of barriers formed by unstable isotopes like in the s-process.

The astrophysical sites of the r-process are not unambiguously identified. One possible astrophysical site for the r-process are core-collapse supernovae with a neutrino-driven wind scenario [2], where the r-process lasts only a few seconds. Here, the neutrino wind dissociates all previously formed elements into protons, neutrons and  $\alpha$  particles [1, 3]. This could explain why the abundance of r-process nuclei of old halo stars are similar to our solar r-process abundances [4].

But as the r-process involves many nuclei far away from stability, its path in the chart of

---

nuclides is unknown and hard to investigate. Previously, detailed simulations on network reactions for the r-process nucleosynthesis were performed concentrating on reaction of heavy nuclei including only a few light nuclei. Terasawa et al. [5] were among the first who included all light nuclei and all nuclei up to the neutron drip-line in their reaction networks. The calculation performed with the larger network were the first to find satisfactory results on the abundance of nuclei with  $A < 200$  but abundances for nuclei with  $A \geq 200$  were underestimated. These simulations further indicate that the inclusion of light elements in the r-process nucleosynthesis has a critical impact on the r-process nucleosynthesis [3, 5]. Therefore, precise measurements of the neutron capture cross sections of (light) nuclei close to the neutron drip-line are of high importance. Afterwards, these can be included in reaction network codes in order to simulate the r-process nucleosynthesis and its path along the chart of nuclides.

Three examples of nuclei on the potential path of the r-process nucleosynthesis are  $^{19}\text{N}$ ,  $^{20}\text{N}$ , and  $^{21}\text{N}$  with their astrophysically important neutron capture reactions:  $^{19}\text{N}(n, \gamma)^{20}\text{N}$  and  $^{20}\text{N}(n, \gamma)^{21}\text{N}$ . As no target material can be produced out of these exotic nuclei (half life  $\tau_{^{19}\text{N}} \approx 330$  ms, half life  $\tau_{^{20}\text{N}} \approx 142$  ms), they have to be produced in beam. Using  $^{20}\text{N}$  (respectively  $^{21}\text{N}$ ) as projectile the  $^{20}\text{N}(\gamma, n)^{19}\text{N}$  (respectively  $^{21}\text{N}(\gamma, n)^{20}\text{N}$ ) reaction will be studied via Coulomb dissociation employing the virtual gamma field of a lead target.

## 2 Development Work for NeuLAND – New Large Area Neutron Detector

Currently, a new accelerator complex is under construction at the GSI Helmholtzzentrum für Schwerionenforschung GmbH in Darmstadt. The Facility for Antiproton and Ion Research (FAIR) will enable a large program for basic research. Also a new setup for Reactions with Relativistic Radioactive Beams (R3B) is planned for research in the fields of nuclear structure and nuclear astrophysics [6]. It will consist of several detector subsystems for a kinematically complete measurement of all the reaction ejectiles. This will allow to reproduce the excitation energy spectrum via the invariant mass method. The NeuLAND spectrometer (New Large Area Neutron Detector) for detecting neutrons with kinetic energies between 200 MeV and 1 GeV will be a key component of the R3B setup [7].

### 2.1 General Design Goals

In order to determine the momenta of high energetic neutrons with high precision, a time-of-flight detector with high resolution is needed. A time resolution of  $\sigma_t \leq 150$  ps and a spatial resolution of  $\sigma_x \leq 1.5$  cm is required. In the high-resolution mode, placing the detector at a distance of 35 m from the target, this will enable a momentum resolution of  $\Delta p/p \leq 10^{-3}$ .

In order to fulfill the goal of measuring all ejectiles in a kinematically complete setup, a high neutron detection efficiency  $\epsilon \geq 95\%$  (similar to the existing LAND) needs to be achieved. In addition, a good multi-neutron response allowing to simultaneously detect and separate up to 5 neutrons per one impinging particle is important for investigating reactions in which more than one neutron is emitted.

In front of the NeuLAND detector, the GLAD magnet (GSI Large Acceptance Dipole) deflects the charged particles, produced in the nuclear reactions, from the neutron branch. In order to cover the full angular acceptance of GLAD of  $\pm 80$  mrad, the NeuLAND detector can be placed at a distance of 15.5 m from the target in the high acceptance mode requiring an active area of  $2.5 \text{ m} \times 2.5 \text{ m}$  [8].

MRPCs (Multi-gap Resistive Plate Chambers) are known for their good time resolution (e.g., [9]). Therefore, a possible NeuLAND concept based on passive steel converters and active MRPC structures is investigated in the framework of this thesis. Beside that, also a pure scintillator based solution for the NeuLAND spectrometer is studied here.

### 2.2 MRPC Concept

RPCs are excellent timing detectors and widely used in high-energy physics experiments, e.g., STAR, RICK, CMS, ATLAS [10]. The CERN group showed time resolutions with  $\sigma_t \approx 50$  ps using multi-gap resistive plate chambers (MRPC) [9]. Ref. [11] reported 20 ps time resolution, utilizing a 24 gaps MRPC. They also can be assembled to large detector arrays with a high granularity. [12] have built an MRPC with dimensions of  $160 \text{ cm} \times 10 \text{ cm}$  achieving a time resolution  $\sigma_t \approx 50..70$  ps and a position resolution  $\sigma_{\text{pos}} = 1.2$  cm along the strips (via the time-difference method). Beside that, a detection efficiency for minimum ionizing particles of  $\epsilon > 95\%$  could be achieved. Therefore, intensive tests were performed to study the feasibility of MRPCs as neutron ToF detector. Within that work, we developed the largest MRPC ever published with dimensions of  $200 \times 50 \text{ cm}^2$ .

Beside that, it is the first MRPC with a massive central iron anode, which acts both as converter and as signal pickup anode.

This development work was done in several steps:

1. Small prototypes with an active area of  $20 \times 40 \text{ cm}^2$  were designed and tested with 30 MeV electrons provided by the ELBE accelerator. Within that phase, several design parameters were varied, for example, the inter strip spacing, number of active gas gaps, differential or single-ended read out, thickness of the readout anodes, and the width of the strips (reported in [13]).
2. The small prototypes were tested with fast quasi-monoenergetic neutrons with a peak energy of 175 MeV at “The Svedberg Laboratory” in Uppsala, Sweden (reported in chapter 2.2.1, [14], and [15]).
3. Based on these tests, the best design parameters for achieving the goals mentioned in chapter 2.1 were extracted to build a large area prototype of  $200 \times 50 \text{ cm}^2$  which is the largest MRPC known from any publications. This prototype was again intensively tested with 30 MeV electrons. Further optimization and the construction of a second prototype of same area was done (reported in chapter 2.2.2, [14], and [16]).
4. Monte Carlo Simulations were performed in order to study the response of the  $200 \times 50 \text{ cm}^2$  prototypes and the final detector array with an area of  $200 \times 200 \text{ cm}^2$  to neutrons with an energy of 200 to 1000 MeV and to study the multi-neutron event identification. Therefore, calibration parameters, especially the space charge effect, interplay of avalanches (merging of signals), and threshold for the final electric signal, were extracted by comparing the experimental results of step 1 with the simulation (reported in [16] and [14]).
5. The  $200 \times 50 \text{ cm}^2$  prototypes were irradiated with fast neutrons, originating from deuteron breakup reactions, at GSI in Darmstadt (not analyzed within this thesis).

## Design and Working Principle

During these studies, the following structure turned out to be optimal for the design of the large prototype. A layout of the large MRPC (named HZDR201b) with an active area of  $2 \text{ m} \times 0.5 \text{ m}$  can be seen in figure 1.

When neutrons impinge onto the steel converter plates, they are converted into charged particles (mainly protons and pions) by quasi-elastic scattering and hadronic interactions. The charged particles generate electron avalanches inside the RPC gas mixture consisting of 85 % Freon (R134a), 10 %  $\text{SF}_6$  and 5 % i-Butane (layer F in figure 1). Due to an applied electric field of 110 kV/cm (at layer E), the avalanches are amplified, before they are induced onto the read out strips (anode (I) made of stainless steel, cathode (D) made of copper) and transferred to dedicated Front End Electronics (FEE). This detector is operated in the Geiger-Müller mode.

A gas gap structure of  $2 \times 2$  was sufficient to achieve a time resolution of  $\sigma_t < 100 \text{ ps}$ , and an efficiency of  $\epsilon > 90 \%$ . The thickness of the gaps of 0.3 mm was provided by polyamid fishing lines. The resistive plates consisted of 1 mm thick soda lime glass. A resistivity of  $\rho = 1 \cdot 10^{13} \Omega \text{ cm}$  was measured. The signal anode and converter strips were made of commercially available stainless steel with dimensions of  $25 \text{ mm} \times 4 \text{ mm} \times 200 \text{ cm}$ . The width of 25 mm turned out to be an optimal compromise between spacial resolution by granularity and the amount of read out channels, which are quite cost-intensive. An inter strip spacing of 1.5 mm was chosen to minimize the crosstalk. The high voltage layer was provided by prefabricated mylar foil ( $\rho = 1 \cdot 10^{15} \Omega \text{ cm}$ ) with semiconducting surface

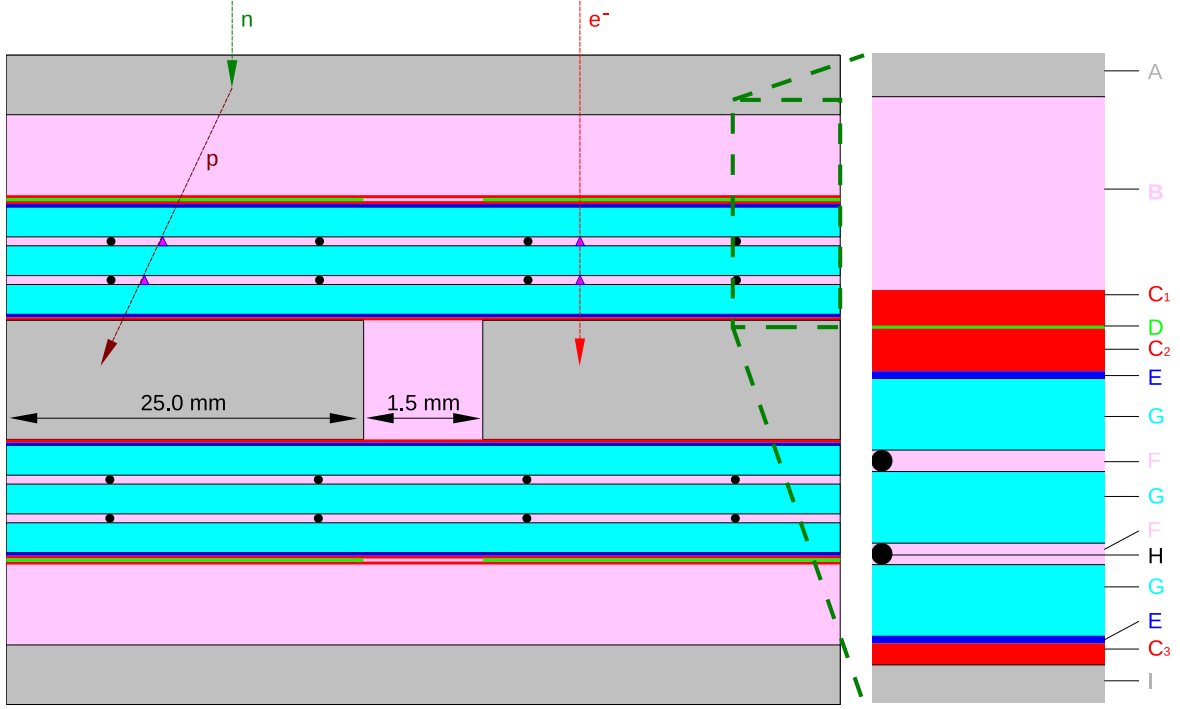


Figure 1: Schematic side view of the  $2\text{ m} \times 0.5\text{ m}$  large prototype. A: stainless steel converter (2 mm), B: gas volume (2.7 mm), C: insulating mylar ( $C_1$ : 0.5 mm,  $C_2$ : 0.6 mm,  $C_3$ : 0.3 mm), D: copper signal electrodes (0.035 mm), E: semiconducting mylar serving as high voltage cathode (0.1 mm), F: gas gap (0.3 mm), G: float glass (1.00 mm), H: polyamid spacer (0.3 mm), I: stainless steel signal anode and converter (4.00 mm). Written in brackets are the dimensions of each layer in beam direction. The triangles along the particle tracks reflect the electron avalanches caused by charged particles. Previously published in [14].

( $\rho = 10$  to  $100\text{ M}\Omega\text{cm}$ ). A differential and single-ended read out is possible.

### 2.2.1 Tests of Small MRPC Prototypes with 175 MeV Neutrons at TSL in Uppsala

In order to study the response of the MRPCs to fast neutrons,  $20 \times 40\text{ cm}^2$  large prototypes were irradiated at “The Svedberg Laboratory” (TSL) in Uppsala, Sweden, with neutrons originating from  ${}^7\text{Li}(p,n){}^7\text{Be}$  reactions with a peak energy of 175 MeV and a low energy tail.

Protons were accelerated in the Gustaf Werner cyclotron to  $179.3 (\pm 0.8)\text{ MeV}$  (0.8 MeV represents the systematic uncertainty in the ToF measurement of the protons) [17]. Afterwards, the protons were extracted within a complex time structure. The macro pulse, a logical signal generated by a pulse generator, started the extraction of the protons. It had a length of 1.04 ms and a repetition rate of 185 Hz (resulting in a duration of 5405 ms). When the macro pulse was active, there was a fine structure, the micro pulse, with a width of 4 to 7 ns and a repetition time of 45 ns, reflecting the cyclotron frequency (compare fig. 3). After the extraction procedure, the protons were lead onto a 23.5 mm thick  ${}^7\text{Li}$  target knocking out neutrons via  ${}^7\text{Li}(p,n){}^7\text{Be}$  reactions with a peak energy of 175 MeV ( $\sigma = 7.4\text{ MeV}$ ) and a low energy tail (compare fig. 3). Behind the target, the protons were deflected into a proton beam dump which served as a beam current monitor.

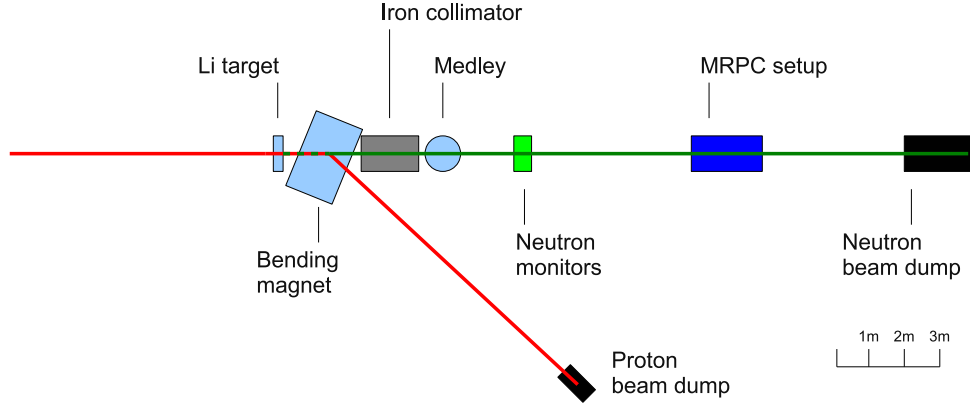


Figure 2: Schematic overview of the beamline in the Blue Hall of the TSL neutron facility. Previously published in [14].

The neutron beam (not effected by the bending magnet) was shaped by iron collimators before impinging onto the Medley setup [18]. There, only a thin  $\text{CH}_2$  target was placed in the neutron beam so that the presence of the Medley setup did not disturb the MRPC measurements. Downstream there were two neutron monitors placed in the beam line: a Thin Film Breakdown Counter (TFBC) [19] and an Ionization Chamber Monitor (ICM) from which we could estimate the number of neutrons impinging onto the MRPC setup that was located at a distance of 11 m from the Li target. A schematic view of the setup can be seen in figure 2.

### Data Acquisition and Analysis

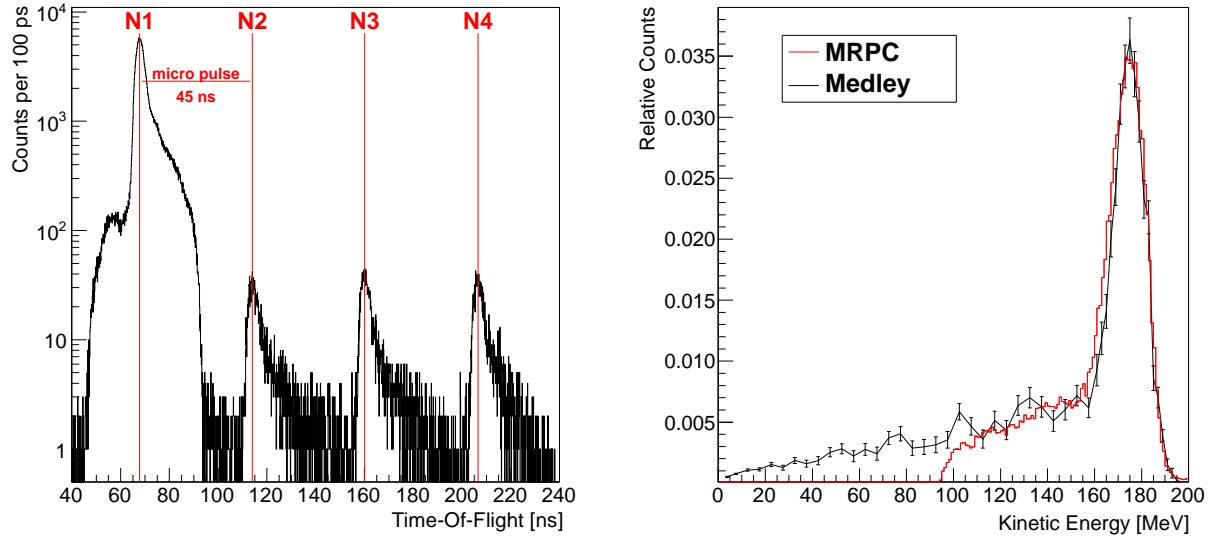
The induced signals at the central anodes were read out by dedicated front end electronics (FEE). FOPI [20] and PADI [21] FEE were used, both providing adjustable thresholds for the individual read out channels. The time signals were sent through a CFD (Constant Fraction Discriminator) and an FPGA (Field Programmable Gate Array). The FPGA combined the MRPC and RF signals to the trigger logic (which was: at least one MRPC channel of each side of the MPRC had to exceed the CFD threshold in coincidence with the RF signal of the accelerator). But it also registered the scaler values, e.g. of the neutron monitors or the dead time. Furthermore, the FPGA provided a coarse time measurement with 25 ns per channel, which was processed for the dead time correction (compare figure 4). Afterwards, the time signals passed a NIM-ECL converter and were fed into a CAEN V1290 multi hit TDC. With a granularity of 25 ps per channel, the TDC registered all events without dead time in a window of 200 ns. This provided optimum conditions for investigating the fine structure of the neutron beam, especially the micro pulses which are illustrated in figure 3a. Thus, four of the micro pulses were covered. The depicted time-of-flight distribution between the hit in the MRPC and the RF signal of the accelerator was gathered with one strip of the MRPC, requesting events when both timing signals exceeded the threshold of the FEE. Afterwards, the average of the timing signals of both ends was calculated. The dominant first bunch indicates neutron events which caused the DAQ to trigger the read out. The latter three bunches are related to consecutive micro pulses of the accelerator separated by 45 ns. The number of events in each of these three bunches divided by the number of events in the triggering bunch, roughly corresponds to the efficiency of the MRPC. The fine structure of one bunch represents the kinetic energy spectrum of the neutron beam which is depicted in figure 3b. The micro pulses



were not properly aligned in time inside the macro pulse. Thus, an artificial broadening of the generated energy spectrum was observed when taking all micro pulses into account. Therefore, the energy spectrum was converted out of the triggering bunch for micro pulses that were generated in the last section of the macro pulse (trigger time  $\geq 680 \mu\text{s}$ ). The distance of the MRPC under study from the Li target was measured on site with 11 m. Due to several delays and different cable lengths no absolute time values which corresponded to the distance from the Li target to the MRPC were provided. Therefore, a time offset which shifts the peak of the energy spectrum to the value of 175 MeV given by Bevilacqua et al. 2011 [18] (black line in figure 3b) was chosen empirically. Afterwards, the Medley spectrum was rescaled to the peak height of the spectrum measured in this experiment.

The charge signal coming from the FEE was fed into a delay and sent to an amplifier before being converted in a CAEN V965 QDC.

Basically, the electronic setup for all detector tests were similar as depicted in figure 11 in section 2.3.



(a) ToF distribution as measured with the MRPC at the TSL facility in Uppsala, representing the micro structure of the TSL cyclotron.

(b) Energy spectrum, converted from the measured ToF spectrum (by fixing the MRPC position at 11 m and applying an empirical time offset to shift the peak energy to 175 MeV). For details see text. Medley spectrum taken from [18] and rescaled.

Figure 3: Results of neutron measurements using MRPCs at TSL in Uppsala. Previously published in [14].

### Dead time Correction and Efficiency Determination

As the MRPC tests were performed in parasitic mode, while the primary experiment took place at the MEDLEY setup, it was not possible to adjust the beam parameters to the specific needs. Especially, a high beam current was used, which caused a high dead time in the Data Acquisition system (DAQ). In general, dead time occurs after one event is registered. It is the duration the DAQ is stunned and cannot record any other event until the dead time has elapsed. Thus, especially in order to calculate the efficiencies of the detectors, a correction of the dead time had to be applied.

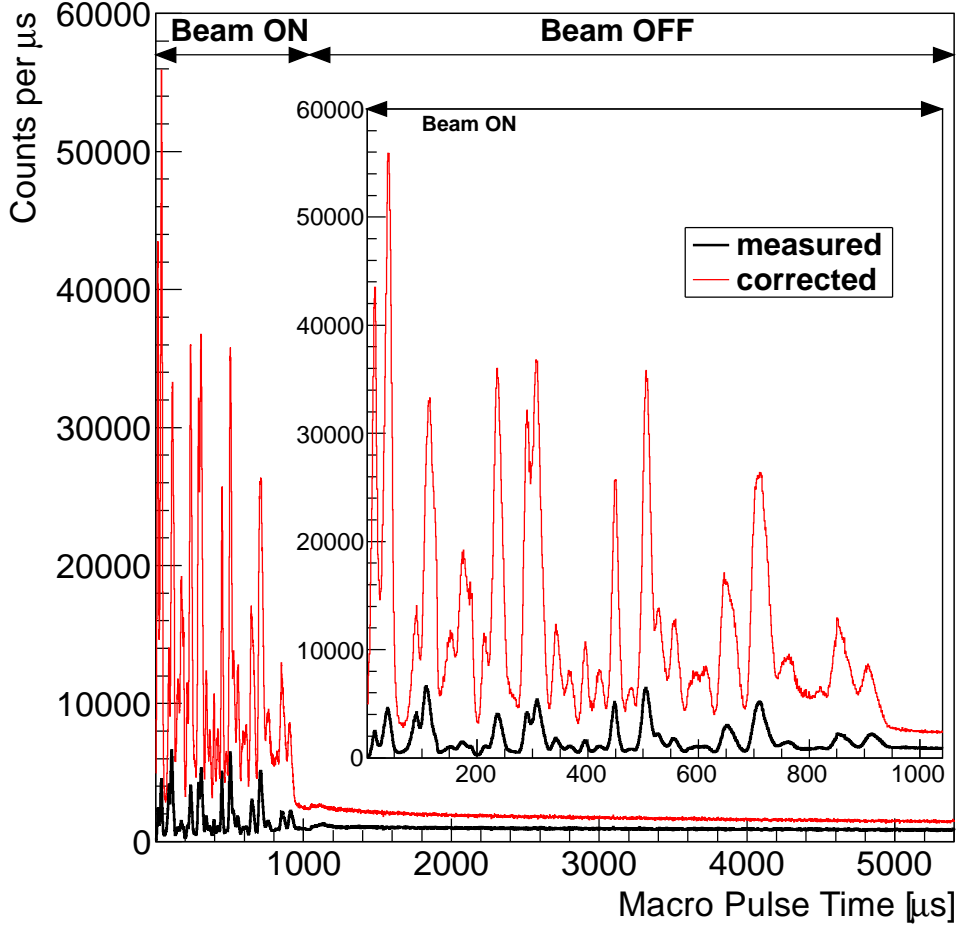


Figure 4: Measured (black) and dead time corrected (red) macro pulse time-of-flight spectra (first bin omitted). See text for details.

In order to perform a dead time correction, the time when one event is recognized in the detector relative to the start of the macro pulse was used (further called MPtime). For each recorded event, this value was filled into a plain MPtime histogram which is shown in figure 4 (thick black line). The high observed background after the beam was switched off can be explained by two effects: First, the high neutron flux during the beam was on caused a high dead time of ca. 90 %, thus, the observed count rate in that region was heavily suppressed. The lower neutron flux during the beam-off period caused a lower dead time of the DAQ, and therefore, more events could be observed. Second, the trigger condition changed: During the beam-off mode, no coincidence with the RF signal of the accelerator was required.

The dead time was estimated from the time difference of two subsequently recorded events inside the macro pulse ( $\text{MPtime}_2 - \text{MPtime}_1$ ), as seen in figure 5 (blue line). There, the dominant peak at  $202 \mu\text{s}$  indicates the mean dead time of the system. But it also includes the probability that a neutron is converted into a charged particle which is, then, detected in the MRPC gas. Thus, the peak is also influenced by the neutron flux: The lower the neutron flux, the smaller is the probability to detect a neutron exactly after the dead time has elapsed and the peak would spread up and more events would be located in the tail after the peak (compare figure 5, black line). But during the experiment, the neutron flux was high enough to minimize this effect. The majority of the events occurred directly after the dead time had elapsed. Therefore, the dead time was estimated with



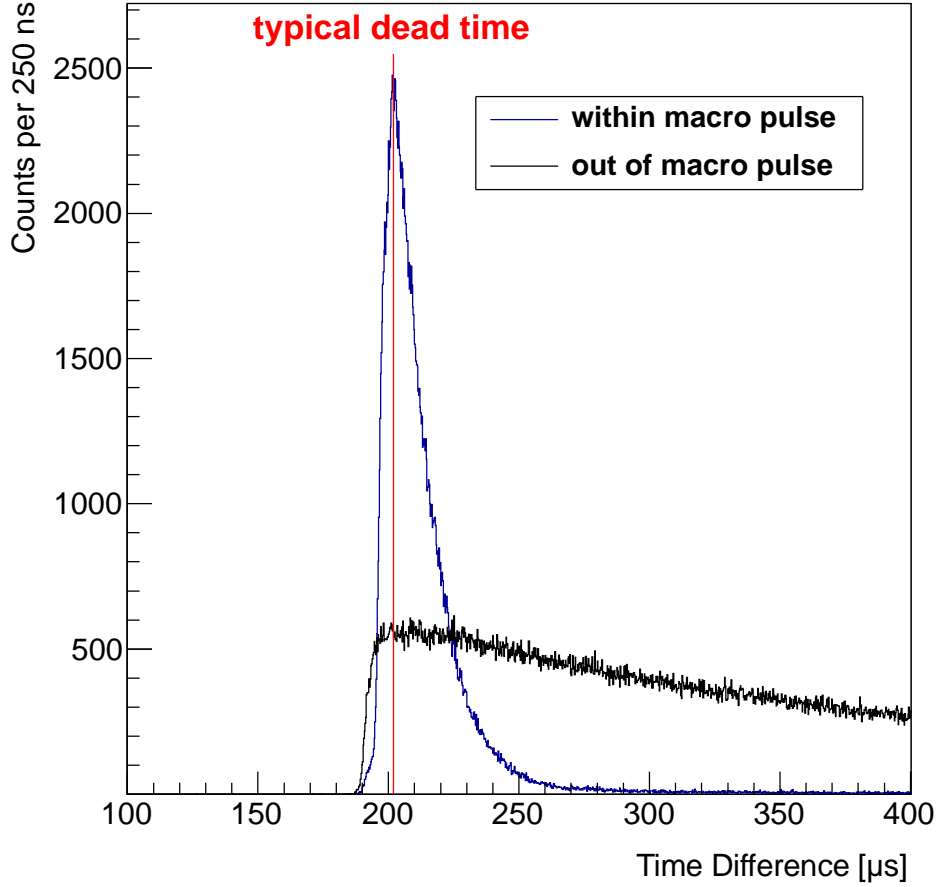


Figure 5: Time difference of subsequently recorded events, during the neutron irradiation of the large MRPCs at TSL for estimation of the mean dead time of the DAQ. The blue line includes only events within the macro pulse showing a clear peak at the typical dead time. The black line includes only events outside of the macro pulse, no clear peak is visible anymore. The vertical red line indicates the typical dead time at  $202\ \mu\text{s}$ . See text for details.

the peak value of this histogram.

Based on this dead time, a histogram with blocked bins was created based on the following considerations: After an event was recognized, for the next  $202\ \mu\text{s}$  the DAQ was blocked, meaning not ready to recognize any new event. Each time, when a bin was blocked, its bin content was increased by one in the blocked bins histogram. One had to be aware of the scenario that the dead time of an event close to the end of a macro pulse could go over into the next macro pulse, meaning its first time bins were still blocked. After repeating this procedure for all recognized events, the blocked bins histogram had to be normalized by the number of macro pulses that elapsed during the period these events were recorded. This value was extracted with the help of the real time of the DAQ, meaning the duration the DAQ was running (provided within the FPGA data with  $25\ \text{ns}$  accuracy). Then, the number of elapsed macro pulses was given by  $N_{\text{MP}} = t_{\text{real}}/T_{\text{macropulse}}$ , while  $t_{\text{real}}$  is the real time the DAQ was measuring and  $T_{\text{macropulse}}$  is the duration of the macro pulse ( $T_{\text{macropulse}} = 1/185\text{Hz} = 5405\ \mu\text{s}$ ).

Afterwards, an unblocked bins histogram was produced, providing information how often a bin (during the macro pulse) was ready for recording events (so, not blocked by the

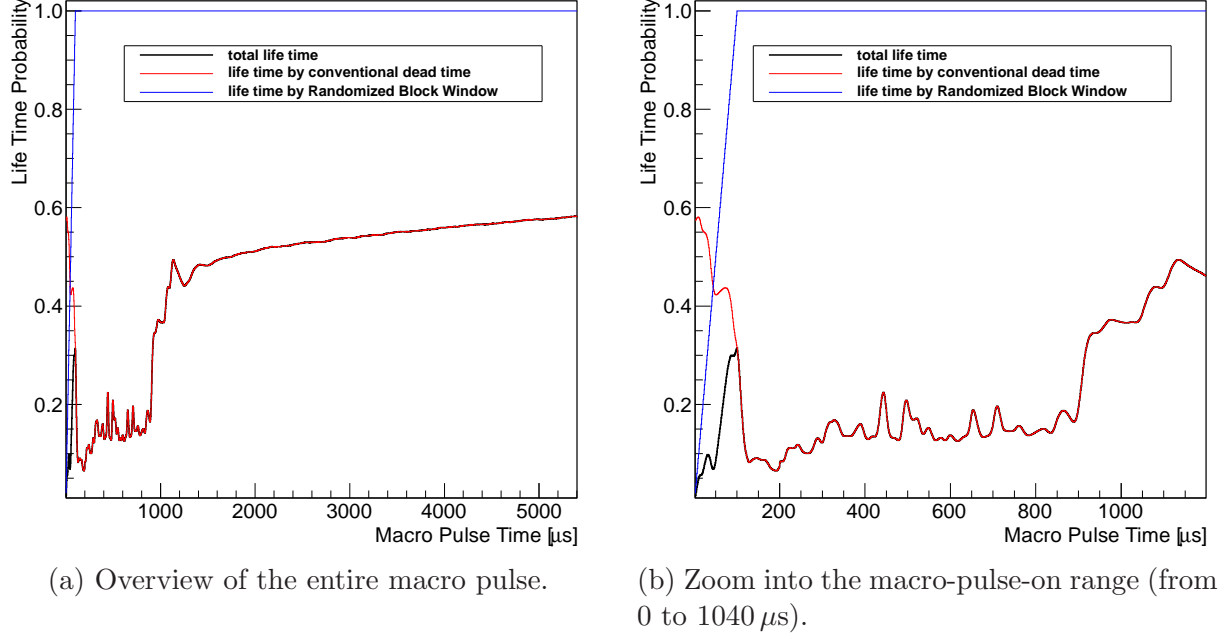


Figure 6: Life time spectra with different contributions over one run, showing bin-wise how often the DAQ was ready for recording events (called UnBlockedBins-histogram in the text). The red line represents the conventional dead time behavior of the DAQ, when blocked while writing the events to tape. The blue line represents the artificial dead time behavior caused by the applied Randomized Block Window. The black line represent the inclusive disjunction of the red and blue line for each event (logical inclusive OR).

dead time) by  $\text{UnBlockedBinsHistogram} = 1 - \text{BlockedBinsHistogram}$  (red line in figure 6).

During that experiment, an additional dead time was artificially created by introducing the so called “Randomized Block Window” (RBW). This was a tentative method to explore the dead time behavior of the DAQ. During the analysis it turned out, that this purpose of the RBW could not be achieved. Anyway, the additional artificial dead time had to be treated in the same manner like the non-artificial dead time caused by the DAQ while recording the event to tape. Therefore, another histogram with blocked bins was filled, normalized by the number of macro pulses and converted into an unblocked bins histogram (called UnBlockedBinsBlockwindow) (blue line in figure 6).

Afterwards, both unblocked bins histograms were added to  $\text{UnBlockedBinsSum} = \text{UnBlockedBins} + \text{UnBlockedBinsBlockwindow}$  (thick black line in figure 6). A corrected MPtime spectrum ( $\text{MPtime}_{\text{corrected}}$ ) was obtained by dividing the plain MPtime spectrum by the sum of the unblocked bins histogram:

$\text{MPtime}_{\text{corrected}} = \text{MPtime}_{\text{plain}} / \text{UnBlockedBinsSum}$ . The corrected spectrum is depicted in figure 4 (red line).

Thereafter, the number of neutrons was calculated by integrating the dead time corrected histogram during the beam-on period (the first 1040 μs). Due to the RBW, the first bins were almost always blocked. This caused a high correction factor during the dead time correction procedure, resulting in an unreasonably huge amount of counts after the dead time correction. With omitting the first bin, this problem was bypassed. Thus, the observed number of neutrons after the dead time correction ( $N_{n,\text{corrected}}$ ) was calculated by integrating the dead time corrected histogram during the beam-on period, omitting

the first bin and its entries.

Beside that, in the corrected trigger spectrum (red line in figure 4) a background in the beam-off range is observed which amounts to 2000 triggers per  $\mu\text{s}$ . This is caused by thermalized neutrons and gamma rays emitted during capture reactions of these neutrons. Despite the different trigger conditions in the beam-on and beam-off range, this background is still present in the first (0-10  $\mu\text{s}$ ) and the last bins (840 - 1040  $\mu\text{s}$ ) of the beam-on range. Therefore, the background is estimated by averaging the values of the last 40  $\mu\text{s}$  in the beam-on range amounting to 20 % of the detected counts.

In order to derive the number of impinging neutrons on the MRPC setup, the neutron monitors (TFBC, ICM) and the proton beam dump (PBD) were utilized. The data on the count rates ( $r_{\text{TFBC}}$ ,  $r_{\text{ICM}}$ ,  $r_{\text{PBD}}$ ) of these monitors were coupled to the employed DAQ system and stored to files during the experiment. The factors for conversion from count rates into neutron fluxes were provided by the Uppsala crew (private communication, A.V. Prokofiev, 2010). Then, the neutron flux was given by

$$j_{\text{TFBC}} = 8.14 \cdot 10^5 \cdot r_{\text{TFBC}} (\pm 10 \%) \text{ cm}^{-2} , \quad (1)$$

$$j_{\text{ICM}} = 5.03 \cdot 10^3 \cdot r_{\text{ICM}} (\pm 10 \%) \text{ cm}^{-2} , \quad (2)$$

$$j_{\text{PBD}} = 32.9 \cdot r_{\text{PBD}} (\pm 30 \%) \text{ cm}^{-2} . \quad (3)$$

These derived fluxes were related to a position 311 cm downstream of the Li target (the exit of the collimator). To convert the neutron flux into the total number of neutrons during the irradiation, one has to multiply with the area of the beam spot at the position where the calibration factors were estimated. The diameter of the beam spot at the exit of the collimator was also given by the Uppsala crew (private communication, A.V. Prokofiev, 2010) with 29.22 mm.

The number of neutrons, then, was given by

$$N_{\text{n,i}} = \frac{\pi(2.922 \text{ cm})^2}{4} j_{\text{i}} , \quad (4)$$

$$N_{\text{n,i}} = \frac{\pi(2.922 \text{ cm})^2}{4} f_{\text{i}} r_{\text{i}} , \quad (5)$$

where index i stands for TFBC, ICM or PBD and  $f_{\text{i}}$  indicates the conversion factors given in equations 1, 2, and 3.

As the neutron monitors were not correlated, the average neutron number of the three monitors was built while their uncertainties ( $u(N_{\text{n,i}})$ ) served as weights.

$$N_{\text{n,total}} = \frac{\frac{N_{\text{n,TFBC}}}{u(N_{\text{n,TFBC}})^2} + \frac{N_{\text{n,ICM}}}{u(N_{\text{n,ICM}})^2} + \frac{N_{\text{n,PBD}}}{u(N_{\text{n,PBD}})^2}}{1/u(N_{\text{n,TFBC}})^2 + 1/u(N_{\text{n,ICM}})^2 + 1/u(N_{\text{n,PBD}})^2} , \quad (6)$$

$$u(N_{\text{n,total}}) = \frac{1}{\sqrt{1/u(N_{\text{n,TFBC}})^2 + 1/u(N_{\text{n,ICM}})^2 + 1/u(N_{\text{n,PBD}})^2}} . \quad (7)$$

Then, the efficiency is given by

$$\epsilon_{\text{RPC}} = \frac{N_{\text{beamON}}^{\text{corr}} - B_{\text{beamON}}^{\text{corr}}}{j_{\text{n}} t A} , \quad (8)$$

where  $N_{\text{beamON}}^{\text{corr}}$  are the counts in the beam-on range of the corrected spectrum,  $B_{\text{beamON}}^{\text{corr}}$  are the background counts in the beam-on range of the corrected spectrum,  $j_{\text{n}}$  is the neutron

flux given by the neutron monitors,  $t$  is the real time of the DAQ (running time),  $A$  is the area of the neutron beam spot size at MRPC position.

Replacing  $j_n t A$  with the number of neutrons  $N_{n,\text{total}}$  derived via equations 5 and 6, the efficiency was calculated by

$$\epsilon_{\text{RPC}} = \frac{N_{\text{beamON}}^{\text{corr}} - B_{\text{beamON}}^{\text{corr}}}{N_{n,\text{total}}} . \quad (9)$$

Systematic uncertainties were estimated based on the following considerations: As the mean dead time in most of the cases amounted to  $200 \mu\text{s}$  (with  $\sigma = 2.5 \mu\text{s}$ ), the dead time correction procedure was performed with values of 198, 200, and  $202 \mu\text{s}$ . The difference, then, gave the systematic uncertainty of the correction procedure amounting to 7%. Furthermore, the uncertainty of the neutron flux measured with the neutron monitors was estimated with equation 7 amounting to 7%. Additionally, statistical uncertainties were considered, dominated by the statistical uncertainty of the background estimation and the run-to-run reproducibility amounting to 10%. With that procedure, the efficiency of the MRPCs are determined to be in the 1% region which are summarized in table 1.

prototype	$\epsilon_{\text{measured}} [\%]$	$\epsilon_{\text{simulation}} [\%]$
HZDR 1b	$0.99 \pm 0.10 \pm 0.14$	$0.90 \pm 0.01$
HZDR 3c	$1.00 \pm 0.10 \pm 0.14$	$0.90 \pm 0.01$

Table 1: Results of the efficiency determination of different prototypes irradiated with 175 MeV neutrons at TSL in Uppsala compared to simulated data as previously published in [15].

Monte Carlo simulations were previously developed and validated using a 30 MeV electron beam at the ELBE facility [16]. The energy spectrum and the beam spot size of the TSL neutron beam at the MRPC under study were coded in this Geant4 simulations in order to perform comparisons of the experimental data to simulations [15]. The experimental data are in fair agreement with the simulations (compare table 1) providing an important confirmation of the simulations. Further discussion on the final detector array will be given in section 2.4.

### 2.2.2 Tests of Large MRPC Prototypes at ELBE

During the research and development phase, many tests and subsequent optimizations had to be performed. A source of fast neutrons was not accessible frequently enough. The detection procedure was based on the conversion of the neutrons into charged particles and consecutive detection of the charged particles in the amplifying gas. Omitting the first step of the detection procedure the ELBE (Electron LINAC with high Brilliance and low Emittance) at HZDR was utilized for the determination of the detector characteristics. It provided electrons with 30 MeV kinetic energy just above the minimum of ionisation [22]. During these tests, the ELBE accelerator was operated in the so called single-electron mode. Reducing the gate voltage much below usual operating parameters together with view screens, thinning out the beam further, the not empty bunches contained only one electron [23]. In addition with the RF signal, that provided a time resolution of  $\sigma_t \approx 5 \text{ ps}$ ) and served as time reference, ELBE offered an excellent capability for detector test, especially the determination of the time resolution and efficiency of the MRPCs.

## General setup at ELBE

During the detector test two small scintillators in front of the MRPC in coincidence with the RF signal of the accelerator served as trigger. The RF signal was delayed, that it always arrives a few ns after the the start of the scintillators. Thus, the RF was time defining and the jitter and resolution of the scintillators did not contribute to the time resolution of the triggering signal. The trigger signal was fed into a read out channel measuring the electronic noise of the DAQ (usually amounting to  $\sigma_{t,\text{noise}} \leq 35$  ps).

## Setup utilizing Conventional Electronics

The signal induced at the strips were treated as described in section 2.2.1. The only major difference was, that a Leading Edge Discriminator instead of a Constant Fraction Discriminator was used for digitizing the time signal, making a time walk correction necessary.

## TacQuila Electronics

In order to keep the tests as close to the final envisaged setup as possible, beside conventional electronics the TacQuila electronics [24], newly developed at GSI, with an RPC-FEE was used. The extended version equipped in the tests provided 16 signal channels and a 17th channel served as common stop signal [25]. The TacQuila provided a coarse time measurement by counting clock cycles relative to the 17th channel. A clock with a frequency of 40 MHz was utilized. A fine time measurement was realized by a Time to Amplitude Converter (TAC) within a range of 25 ns. The time measurement of each channel was started when a signals had arrived. The TAC measured the time to the beginning of the next clock cycle (fine measurement). Afterwards, the clock cycles to the stop signal (17th channel) were counted. Then, the times ( $t_i$ ) measured for each individual TAC channel  $i$  were calculated by

$$t_i = t(\text{tac}_i) - t(\text{tac}_{17}) + (\text{counter}_i / f_{\text{clock}}) , \quad (10)$$

where  $t(\text{tac}_i)$  is the time measured by the TAC channel  $i$ ,  $t(\text{tac}_{17})$  is the time measured by the 17th TAC channel,  $\text{counter}_i$  is the elapsed number of clock cycles until the 17th channel fired for TAC channel  $i$ ,  $f_{\text{clock}}$  is the frequency of the clock (40 MHz). The time calibration (converting channels into ns) was done utilizing a white TAC spectrum (compare figure 7a). The width of the histogram was given by the frequency of the clock. Then, the time ( $t(\text{bin}_j)$ ) of an event at a bin with the number  $j$  was derived by:

$$t(\text{bin}_j) = \frac{1}{f_{\text{clock}}} \cdot \frac{B}{A} , \quad (11)$$

where  $A$  is the integral over the whole histogram,  $B$  is the integral of the histogram up to bin  $j$ . A correlation of time [ns] to the bin number is given in figure 7b.

## Analysis

The analysis was similar for both electronic setups. An event was defined to be valid if a signal at both ends of one the strip was detected, i. e. the signal exceeded the threshold of the TDC. Cross-talk events were excluded using a charge selection: If an electron hit the detector between two strips it induced a charge on both of them. The closer the

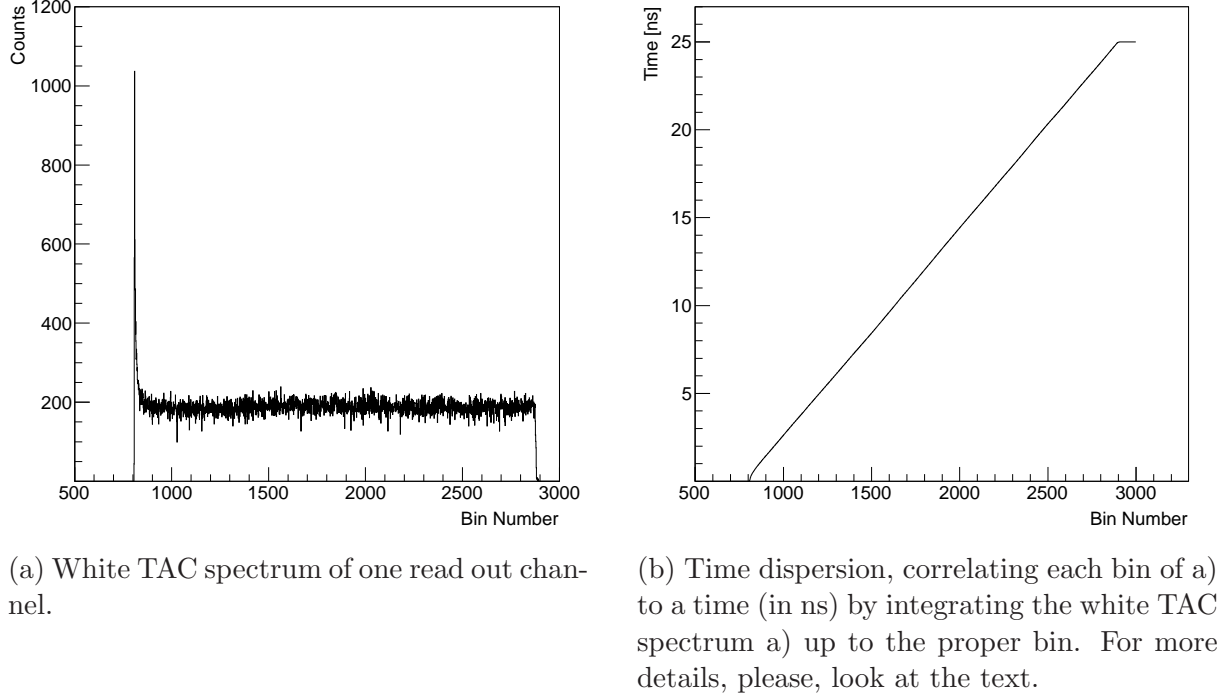


Figure 7: Time calibration of the raw data derived with the TacQuila electronics.

electron was located at one strip the higher was the charge detected by the strip. Thus, if an event caused a higher charge at the neighbouring strip than at the one which the beam fired on it was classified as cross-talk event and not counted for time walk correction and time resolution determination. In order to perform a time-walk correction a TDC vs QDC histogram was utilized and a sum of an exponential and a 2nd order polynomial regression was applied. Afterwards, the average of the measured time was built and a Gauß-fit provided the time resolution  $\sigma_{t,\text{strip}+\text{noise}}$  of the examined strip. As this still includes the electronic noise of the setup, a quadratic subtraction of  $\sigma_{t,\text{noise}}$  revealed the pure time resolution  $\sigma_{t,\text{strip}}$  of the investigated strip.

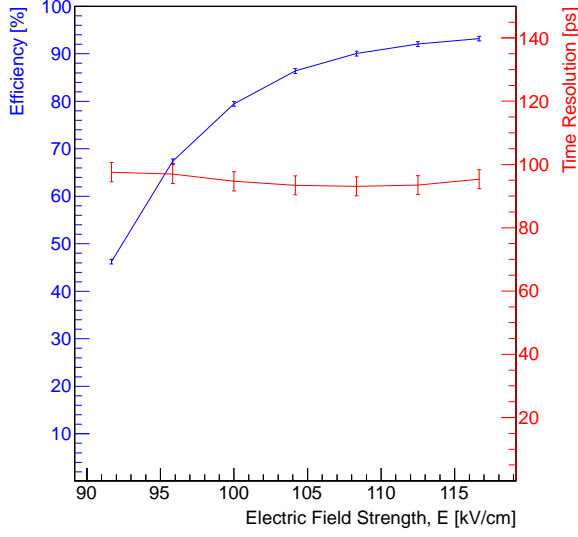
In order to calculate the efficiency of the detector, the condition that both ends of a strip had to fire was applied, too. But here, no special cross-talk treatment was necessary. Due to the beam spot size, which always included three MRPC-strips, one event was once counted either to the one or to the neighbouring strip but not counted more than once. Cross-talk from not irradiated strips was almost negligible with  $\leq 1\%$ ). Then, the efficiency of all three strips was calculated by dividing the number of valid events by the number of triggering events.

The results of both electronic setups are summarized in figure 8.

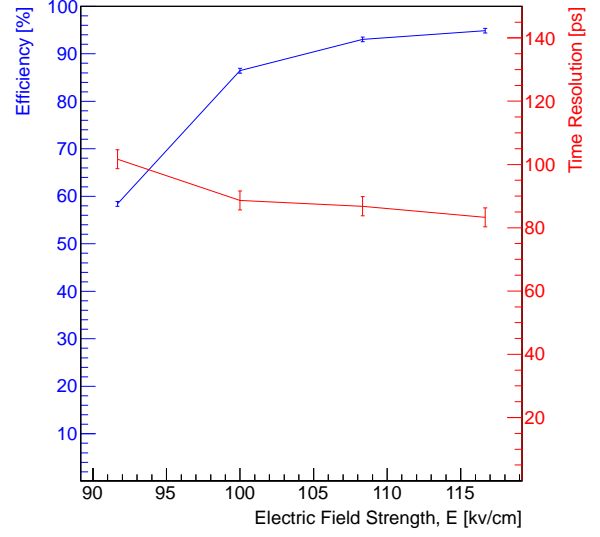
## Summary and Results

Large MRPC prototypes were irradiated with minimum ionizing electrons of 30 MeV kinetic energy along different strips. The detector characteristics were measured in correlation of the position, the high voltage, and the trigger rate with conventional electronics (figure 8, 9). For the TacQuila electronics only a high voltage scan was performed (figure 8a).

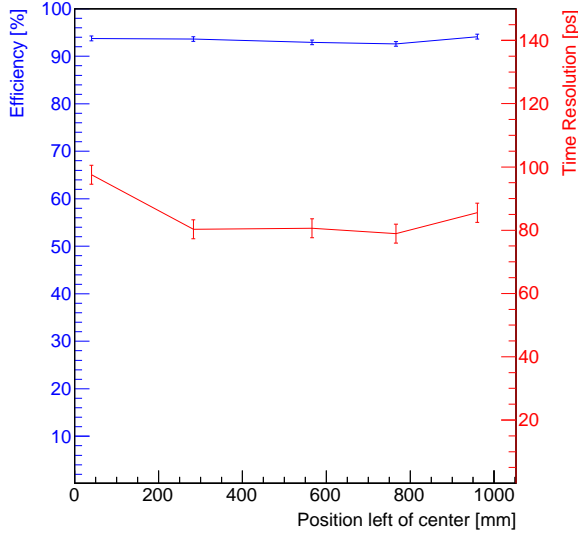
With a trigger rate at 200 Hz, time resolutions of  $\sigma_t \leq 110$  ps were achieved with both different electronic setups for electric field strengths between 92 and 117 kV/cm (figure



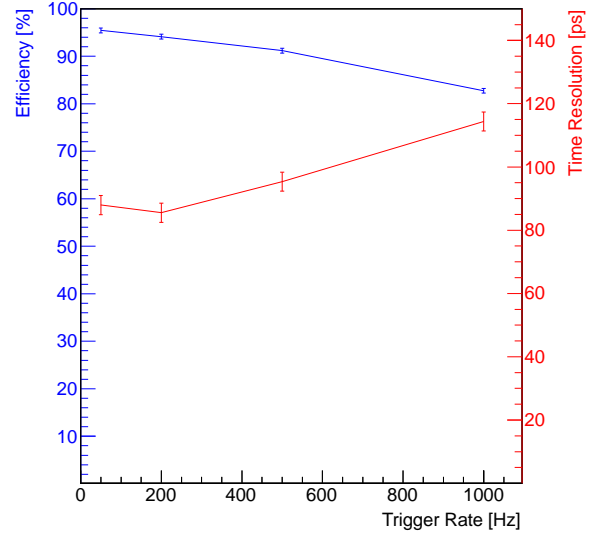
(a) Efficiency (blue line) and time resolution (red line) correlated to the electric field strength measured at prototype HZDR201b at the center of strip four read out with TacQuila electronics.



(b) Efficiency (blue line) and time resolution (red line) correlated to the electric field strength measured at prototype HZDR201b 566 mm left of the center of strip four read out with FOPI-FEE and conventional electronics.



(c) Efficiency (blue line) and time resolution (red line) correlated to the position along strip four of prototype HZDR202 read out with FOPI-FEE and conventional electronics. The applied electric field strength was  $116.7 \text{ kV/cm}^2$  (7 kV).



(d) Efficiency (blue line) and time resolution (red line) correlated to the trigger rate measured at prototype HZDR202 960 mm left of the center of strip four read out with FOPI-FEE and conventional electronics.

Figure 8: Efficiency and time resolution measured with two similar large prototypes read out with either TacQuila or FOPI-FEE plus conventional electronics. Lines are just to guide the eye.



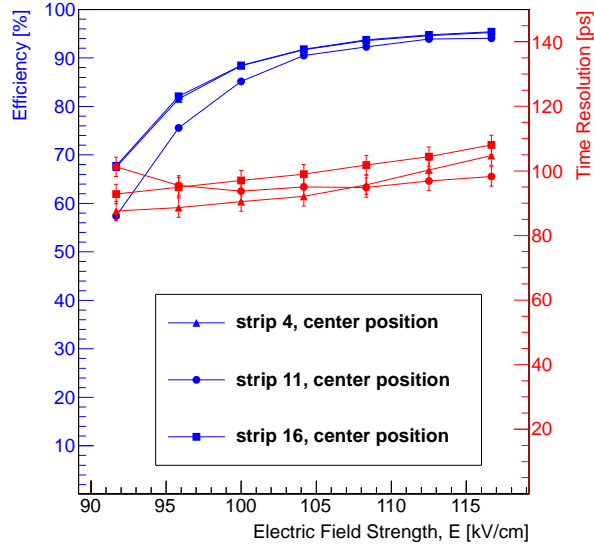


Figure 9: Efficiency (blue line) and time resolution (red line) correlated to the electric field strength measured at prototype HZDR201b at the center of strip four, eleven and sixteen read out with FOPI-FEE and conventional electronics. Lines are just to guide the eye.

8a, 8b, 9) measured at several strips of the large prototypes. The slightly higher values of  $\sigma_t$  at lower electric field strengths can be explained by the low efficiency, resulting in low statistics. Also the walk correction, then, became corrupted. The slight increase at higher electric field strengths (figure 9) might be due to the high amplification which caused a large space the electron avalanches gained. This also broadened the signal induced on the strip and worsened the time resolution. The efficiency of the MRPC increased with the electric field strength, as more avalanches were produced in the amplifying gas which exceeded the number of recombinations in the gas.

The position scan along one strip (figure 8c) revealed small fluctuations of both the time resolution and the efficiency. For an electric field strength of  $E \geq 105$  kV/cm and a trigger rate of 250 Hz values of  $\sigma_t \leq 100$  ps and  $\epsilon \geq 90$  % were achieved. No trend could be identified.

Both the time resolution and the efficiency worsened with increasing trigger rate, measured at 50, 200, 500, and 1000 Hz (figure 8d). This was caused by charge carriers which were accumulated at the surface of the resistive plates (the floating glass) shielding the avalanches in the amplifying gas from being induced onto the read out strips. But for RIB experiments with rather low beam intensities, this effect is of no relevance. Anyway, improvements compensating this effect would be achieved by using a resistive plate with a lower resistance which enables a faster evacuation of the charges at the surface (e.g. Naumann et al. [26] using electrodes made of ceramics composite).

High efficiencies and good time resolutions were achieved when MRPCs were irradiated with minimum ionizing electrons. The design goals were satisfied for the single device (see later for the full array) A comparison of MRPCs to scintillators and a conclusion for the R3B setup at FAIR will be given in section 2.4.



### 2.3 Scintillator Concept

Beside the MRPCs, also a solution based on pure plastic scintillator without any converter material was investigated. The scintillator bars were made of RP-408, manufactured by Rexion, which is based on Polyvinyltoluene [27] similar to EJ-200 and BC-408. It has a wavelength of maximum emission of 425 nm and provides fast timing properties (decay time of 2.1 ns) and a long optical attenuation length (usually 4 m). The active part of the bars had a rectangular cross section of  $5 \times 5 \text{ cm}^3$  and a length of 250 cm. At the ends they were tapered from its rectangular shape to a circular shape of 1 inch (25.4 mm) to provide a light guide structure fitting to the entrance window of the photomultiplier. The active area and the light guide structures were produced in one piece avoiding losses at optical borders. The total length amounted to 270 cm. The bars were equipped at both ends with Hamamatsu R8619 photomultipliers requiring a usual supply voltage of 1000 V [28]. With a diameter of 1 inch and a peak sensitivity of 420 nm they were well compatible with RP-408 scintillator bars (with a wavelength of maximum emission of  $\lambda = 425 \text{ nm}$ ).

In order to study the detector assembly, NeuLAND submodules, consisting of two PMTs and one scintillator bar, were irradiated at ELBE with minimum ionizing electrons of 30 MeV kinetic energy, as already described in section 2.2.2. A sketch of the detector setup is provided in figure 10. In front of the NeuLAND bar and behind three thin scintillators were placed each with a thickness of 5 mm. They were coupled to fast PMTs. Both the one in front of the NeuLAND bar, called S1S2, and the most distant behind the bar, called S3S4, had an active area of  $20 \times 20 \text{ mm}^2$  and were each read out at both

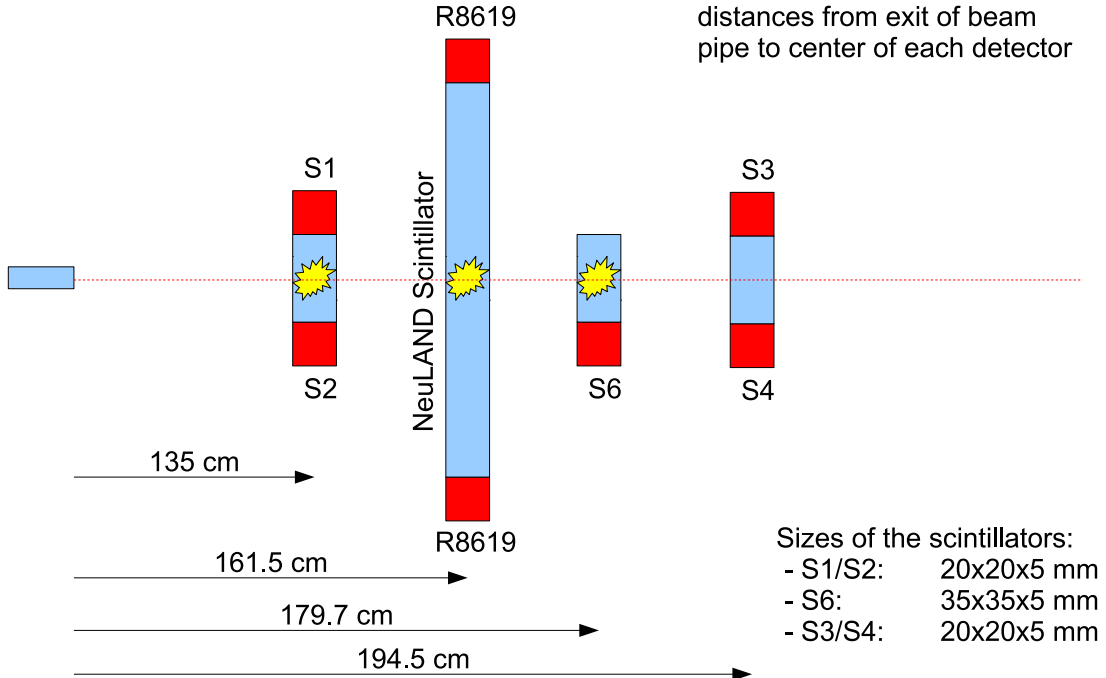


Figure 10: Detector setup at the ELBE cave 112 as seen from above. Given are the distances from the beam pipe exit window to the center of each detector. S1, S2, S3, S4, and S6 are PMTs connected to thin scintillators to define the accepted beam spot on the NeuLAND submodule and to build the trigger logic in coincidence with the RF signal of the accelerator. Exchanging the NeuLAND submodule with an MRPC, this setup was also used for MRPC tests mentioned in section 2.2.2.

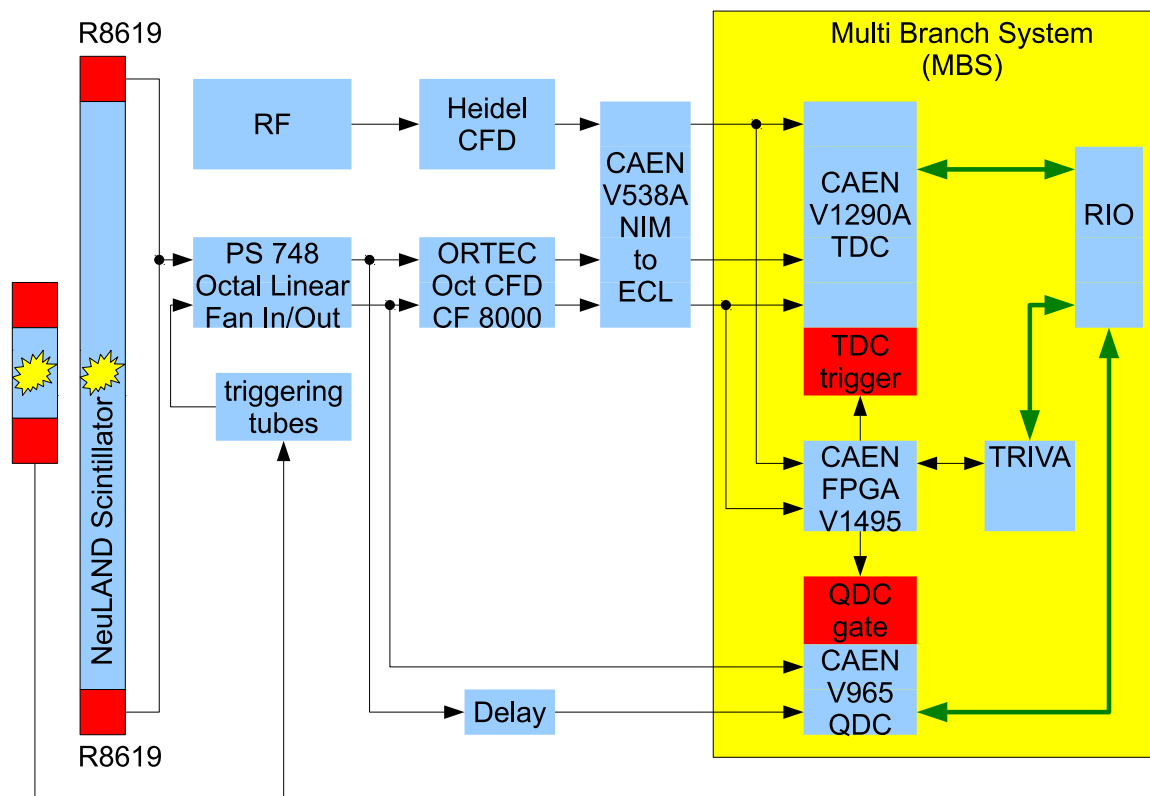


Figure 11: Electronic Setup used for NeuLAND tests at Elbe with 30 MeV electrons.

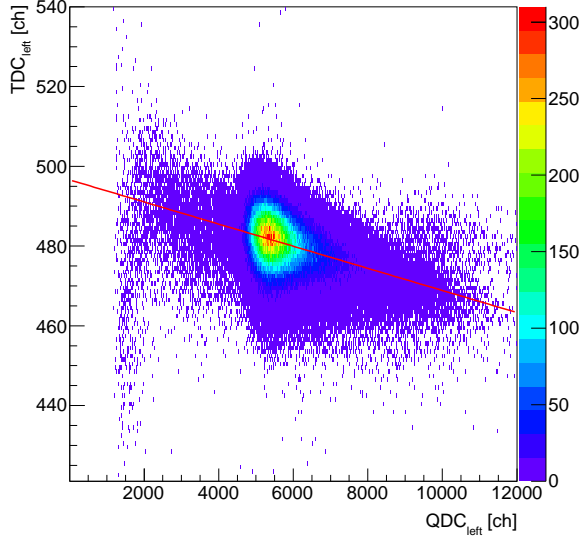
ends. The third in between NeuLAND and S3S4 with an active area of  $35 \times 35 \text{ mm}^2$ , called S6, was coupled to only one PMT. S1, S2 and S6 defined the accepted beam spot size on the NeuLAND bar and in coincidence with the RF signal of the accelerator they built the trigger logic ( $S1 \wedge S2 \wedge S6 \wedge \text{RF}$ ) measuring a trigger rate of roughly 800 Hz.

The electronic setup is depicted in figure 11 and was basically similar to the MRPC tests with fast neutrons at Uppsala in section 2.2.1 or the tests of large MRPCs at ELBE in section 2.2.2. In contrast to section 2.2.2, a CFD was used to convert the timing signal of the NeuLAND PMTs into digital values omitting the need of a complicated walk correction. A constant threshold of -50 mV was applied for each PMT of the NeuLAND bar.

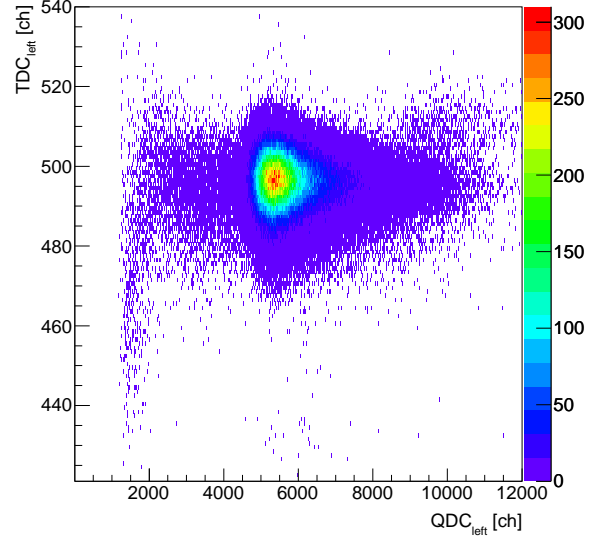
With the above described setup, the time resolution and efficiency were measured as function of the position along the bar and the high voltage applied to the R8619 PMTs.

## Data Analysis

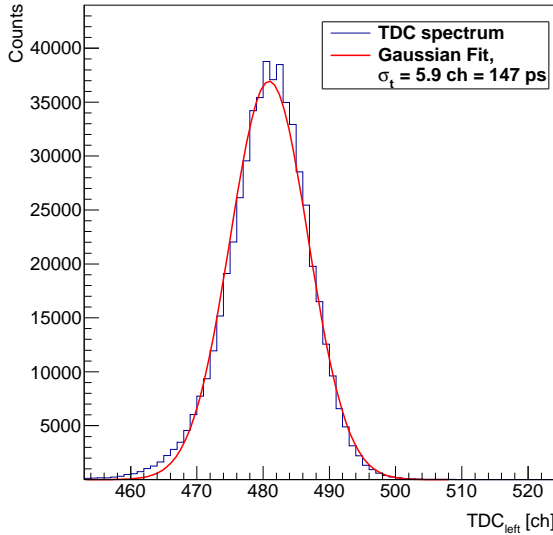
Although a CFD was used for these tests, a small walk effect was observed (compare figure 12a) blurring the measured time resolution of the NeuLAND submodule. In order to correct for that, a linear walk correction was applied (in contrast to the sophisticated walk correction in section 2.2.2). To this end, the measured TDC values were plotted in correlation to the measured QDC values for each PMT separately (figure 12a). Afterwards, a linear regression was applied (red line in figure 12a) and subtracted from the measured TDC data to derive the time walk corrected TDC values. A Gaussian fit was applied to derive the time resolution of a single PMT after walk correction (figure 12d). The walk correction procedure is illustrated in figure 12. On the left side there are the uncorrected (measured) data and on the right side there are the walk corrected data.



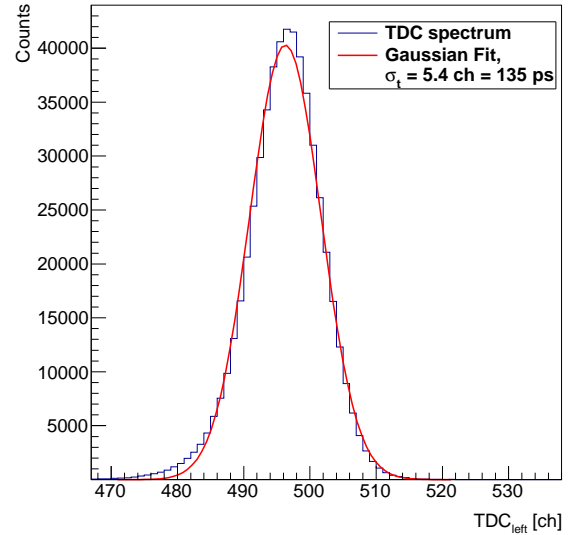
(a) TDC in correlation of the QDC measured at the left PMT of the NeuLAND scintillator bar. The red line represents the linear regression applied to make walk correction.



(b) Walk corrected TDC in correlation of the QDC obtained at the left PMT of the NeuLAND scintillator bar.



(c) TDC spectrum measured at the left PMT of the NeuLAND scintillator bar before walk correction.

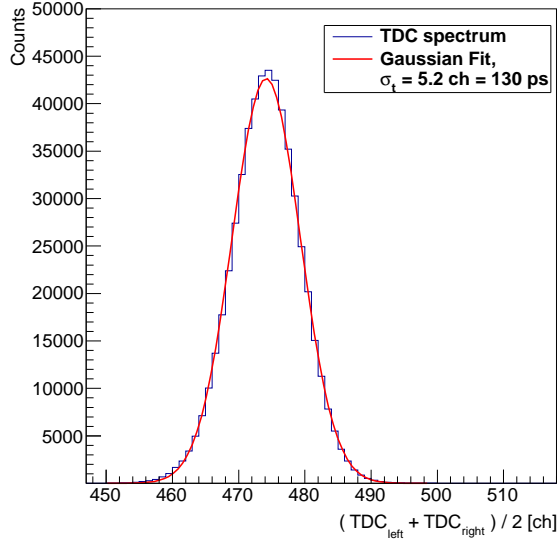


(d) Walk corrected TDC spectrum of obtained at the left end of the NeuLAND scintillator bar.

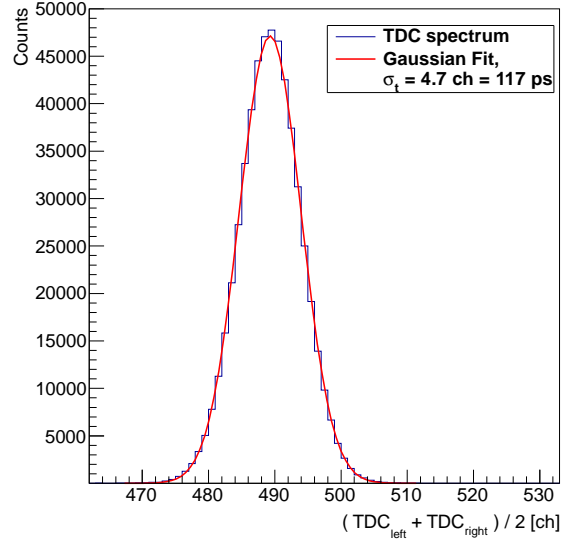
Figure 12: Time walk correction procedure applied for each PMT equipped to the NeuLAND scintillator bar.

Afterwards, the average of the corrected TDC data of both PMTs was built requiring that both PMTs fired to have a valid event. A Gaussian fit was applied where the sigma represents the time resolution of the whole setup  $\sigma_{t,\text{NeuLAND}+\text{noise}}$  including the noise of the electronics  $\sigma_{t,\text{noise}}$  (figure 13b). A comparison of the average TDC data is given in figure 13a and 13b.

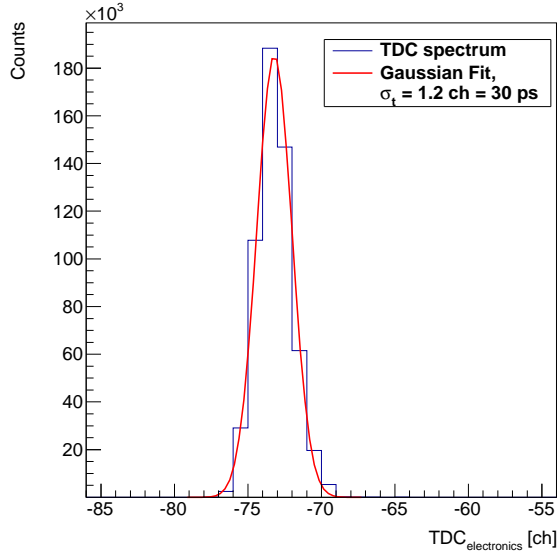
Subsequently, the electronic noise was examined by analyzing the triggering signal which was fed into a read out channel (figure 13c). A Gaussian fit was applied measuring a time resolution of  $\sigma_{t,\text{noise}} = 30$  ps. In order to calculate the final time resolution of the



(a) Average time spectrum built of both PMTs of one NeuLAND bar before walk correction.



(b) Walk corrected average time spectrum built of both PMTs of one NeuLAND bar.



(c) Time spectrum of the time defining triggering signal, measuring the time resolution of the electronic noise.

Figure 13: Average time spectra of both PMTs before and after walk correction and the spectrum of the time defining signal representing the electronic noise.

NeuLAND scintillator assembly without electronic noise of the DAQ, the electronic noise was subtracted quadratically

$$\sigma_{t,\text{NeuLAND}} = \sqrt{\sigma_{t,\text{NeuLAND}+\text{noise}}^2 - \sigma_{t,\text{noise}}^2} . \quad (12)$$

The efficiency was calculated by comparing the events in the corrected average TDC histogram against the number of events that caused a trigger.

## Summary and Results

NeuLAND scintillator bars equipped with Hamamatsu R8619 PMTs were irradiated at ELBE with minimum ionizing electron of 30 MeV kinetic energy and read out with conventional electronics. The time resolution and the efficiency in dependence of the high voltage applied to the PMTs and the position along one bar were derived. The results of the test derived with the above described analysis procedure are summarized in figure 14.

A small increase of the efficiency with increasing high voltage applied to the R8619 PMTs was observed. In the range from 850 V to 1300 V efficiencies of  $\epsilon \geq 98\%$  were achieved (figure 14a, blue line). The time resolution decreased slightly for increasing high voltages in the range of  $U=900$  V to  $U=1300$  V and is always below 115 ps (figure 14a, red line). The worse time resolution at  $U=850$  V can be explained by the non-linearity of the CFD (figure 14d). In this regime the TDC versus QDC spectrum shows a complex non-linear behavior which cannot be corrected with the above described walk correction procedure.

The position scans along one bar (figure 14b) revealed small fluctuations along the NeuLAND scintillator bar for both the time resolution (red line) and the efficiency (blue line) which are almost entirely explained by the uncertainties. The time resolution is  $\sigma_t \leq 118$  ps and the efficiency is  $\epsilon \geq 98.9\%$ .

The electronic noise measured by feeding the triggering signal into a read out channel amounted to  $\sigma_{t,\text{noise}} = 30$  ps.

## 2.4 Summary and Conclusion

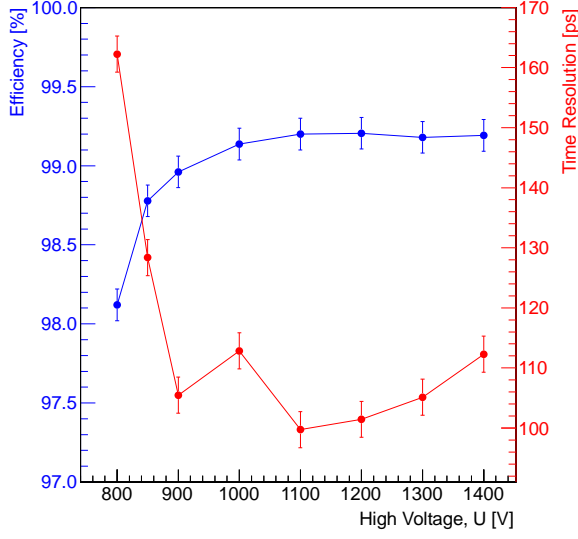
Large size MRPCs were irradiated with minimum ionizing electrons at ELBE (section 2.2.2) showing good time resolutions  $\sigma_t \leq 110$  ps and efficiencies  $\epsilon_{\text{electron}} \geq 95\%$ . The analysis of the irradiation of small MRPC prototypes with 175 MeV neutrons was shown (section 2.2.1) revealing efficiencies  $\epsilon_{\text{neutron}} = 1.00 \pm 0.10 \pm 0.14\%$  (table 1) which are in good agreement with simulations. The derived energy spectrum is consistent with data taken with the MEDLEY spectrometer (figure 3, [18]). The behavior of the MRPCs was well reproduced with GEANT4 simulations [16]. The results reported in this thesis, i. e. the neutron efficiency determined in section 2.2.1, are an important approval of the correctness of the simulation. Simulations with the full detector array, consisting of 50 MRPC layers to achieve an efficiency of  $>90\%$  for 400 MeV neutrons, showed a limited multi-neutron response [7] while a relative energy spectrum was reconstructed for a one-neutron event achieving a resolution of  $\sigma = 17$  keV [7].

NeuLAND scintillator bars, manufactured out of RP-408 by Rexon [27], were irradiated at ELBE with minimum ionizing electrons (section 2.3). High efficiencies of  $\epsilon_{\text{electron}} \geq 97\%$  and time resolutions of  $\sigma_t \leq 120$  ps were achieved (figure 14). These results were also proved by recent measurements with cosmic muons and protons [7]. Simulations showed a good multi-neutron response and relative energy resolutions of  $\sigma = 15$  keV for a one-neutron event.

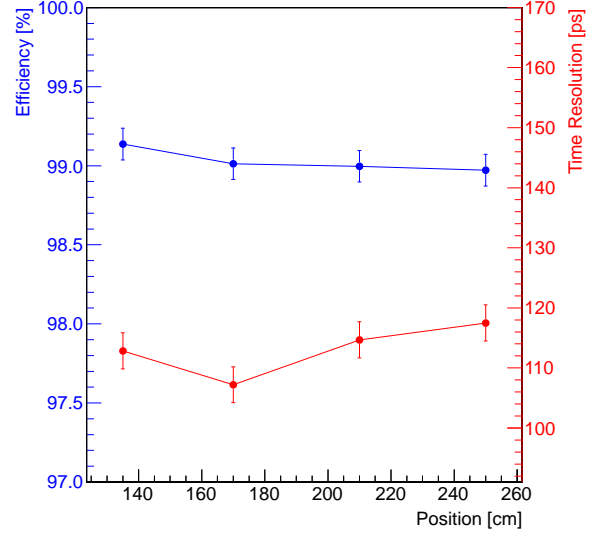
Both MRPCs and the scintillator option showed high efficiencies and good time resolutions. The multi-neutron response of the pure scintillator solution was much better than for MRPCs due to the fact that the deposited energy can be utilized to reconstruct the neutron paths. Furthermore much less efficiency losses due to passive layers inside the detector lead to a higher efficiency of the scintillator. This also improved the resolution of the relative energy spectrum of the scintillator in contrast to the MRPC. Therefore,

the scintillator option was chosen to be employed as NeuLAND detector in the upcoming R3B setup at FAIR.

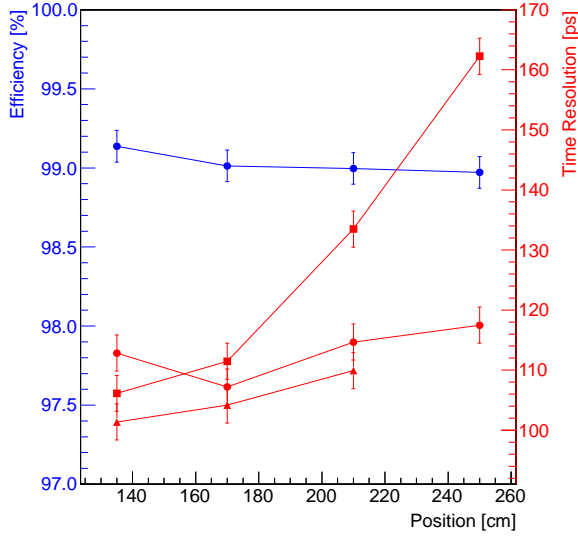
However, the MRPC development was no failure. One of the largest MRPC ever with an area of  $200 \times 50 \text{ cm}^2$  were built during this research and development phase. It was proved that MRPCs can be utilized as neutron detectors with a high single neutron efficiency. Therefore, it is presently under investigation whether MRPCs can be implemented in setups where low multi-neutron capability is needed.



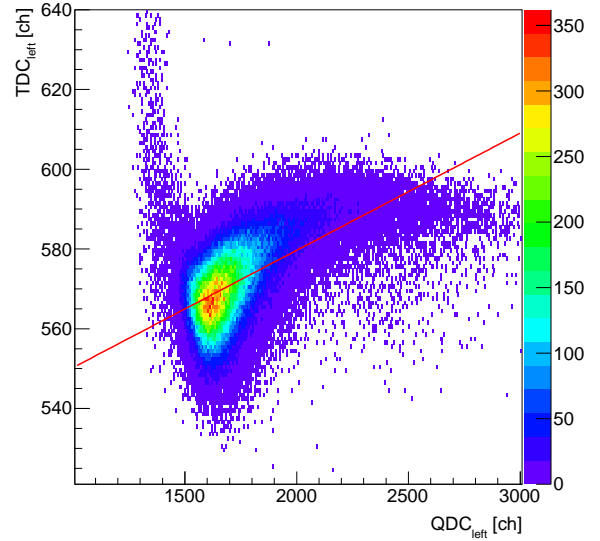
(a) Efficiency and time resolution in correlation of the high voltage applied to the R8619 PMTs.



(b) Efficiency and time resolution in correlation of the position along one NeuLAND bar.



(c) Efficiency and time resolution in correlation of the position along one NeuLAND bar taken with 900 V (squares), 1000 V (circles, same data like in figure 14b) and 1100 V (triangles) applied to the R8619 PMTs.



(d) For supply voltages at the PMTs below 900 V the CFD runs into a non-linear regime corrupting the above described walk correction. Here, a measurement with 800 V at the center of the bar is presented. The red line represents the linear fit applied for the walk correction as described earlier in the text and in figure 12.

Figure 14: Efficiencies and time resolutions derived for the NeuLAND bars tested at ELBE. Lines are just to guide the eye.





## 3 Experimental Methods & Techniques at the LAND/R3B Setup

### 3.1 Radioactive Ion Beam Production at the FRS

As neutron rich nuclei close to the neutron dripline are very short-lived, no target material can be produced of them. In the s393 experiment the radioactive ions were produced out of a primary  $^{40}\text{Ar}$  beam injected into the UNILAC (UNiversal Linear ACcelerator) where they were accelerated to an energy of 11.5 MeV/u ( $\beta = 0.15$ ) on a path of 120 m. Afterwards, the ions were guided into a 130 m long transfer beamline where they were stripped to complete ionization. Subsequently, they were further accelerated in the SIS-18 (SchwerIonen Synchrotron with a maximum bending power of 18 Tm) to 490 MeV/u. This accelerator is a fast cycling synchrotron with a circumference of 217 m. Then, the  $^{40}\text{Ar}$  ions were guided into the Fragment Separator setup (FRS). At the FRS entrance, they impinged onto a 4011 mg/cm<sup>2</sup> thick Be target producing a large number of secondary ions with masses lower than the  $^{40}\text{Ar}$  primary beam. Thereafter, the secondary ions passed a separation stage, consisting of deflecting magnets in a fixed beam trajectory. In general, the interaction of charged particles with electric and magnetic fields and following the forces that lead to the deflection of the charged particle can be described with:

$$\vec{F} = q(\vec{E} + \vec{v} \times \vec{B}) . \quad (13)$$

Here,  $q$  is the charge of the particle,  $\vec{E}$  is the electric field strength,  $\vec{v}$  is the velocity of the charged particle,  $\vec{B}$  is the magnetic flux density.

Inside the magnets of the FRS, only magnetic fields and no electric ones were present, thus, the electric component in equation 13 can be omitted. Furthermore, only the magnetic field component  $B_{\perp}$  perpendicular to the velocity vector of the particle lead to a radial acceleration. Then, the Lorentz-force equals a radial force

$$F_{\text{Lorentz}} = F_{\text{radial}} . \quad (14)$$

Taking relativistic transformations into account, equation 13 evolves to

$$\gamma m \frac{v^2}{\rho} = qvB_{\perp} , \quad (15)$$

where  $m$  is the rest mass of the particle,  $\rho$  is the radius of the circular orbit. Replacing  $m = Au$ ,  $q = Ze$ ,  $v = \beta c$ , where  $A$  is the mass number of the particle and  $u$  is the mass unit,  $Z$  is the charge number and  $e$  is the elementary charge,  $\beta = v/c$  with  $c$  the speed of light and  $\gamma = 1/\sqrt{1 - \beta^2}$ , the equation can be written

$$B\rho = \text{const} \frac{A}{Z} \beta \gamma , \quad (16)$$

with  $\text{const} = \frac{uc}{e} .$

Fixing the beam trajectory by the magnetic rigidity  $B\rho$ , the secondary particles were separated according to their mass-over-charge ratio by accepting only defined velocities ( $\beta$ ) of the specific particle species.

In the FRS setup there were two 3 mm thick scintillators, read out at both ends, used for ToF-measurements to identify the particles in the cocktail beam. The S2 scintillator

was placed at the middle focus 136 m upstream of the reaction target. As it was overloaded with the intense ion beam, it could not be used for the particle identification. The second scintillator, S8, was placed further downstream with 55 m flight path to the reaction target.

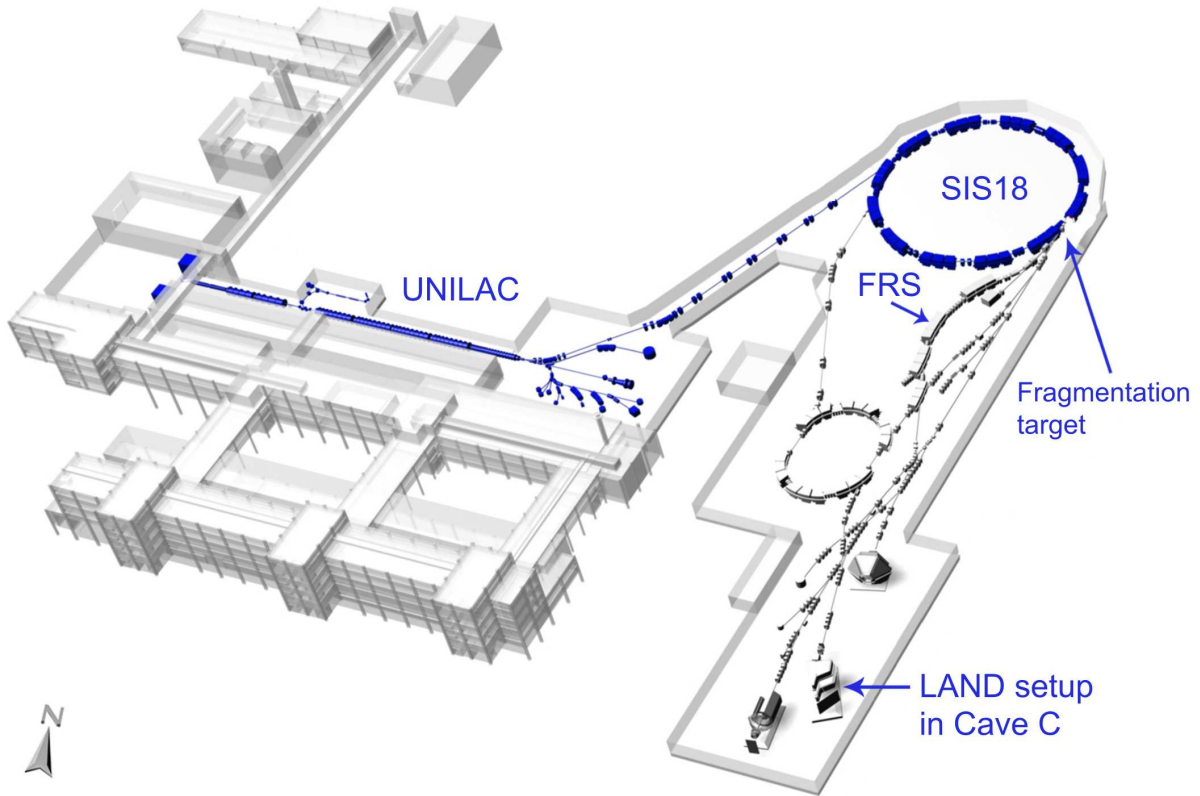
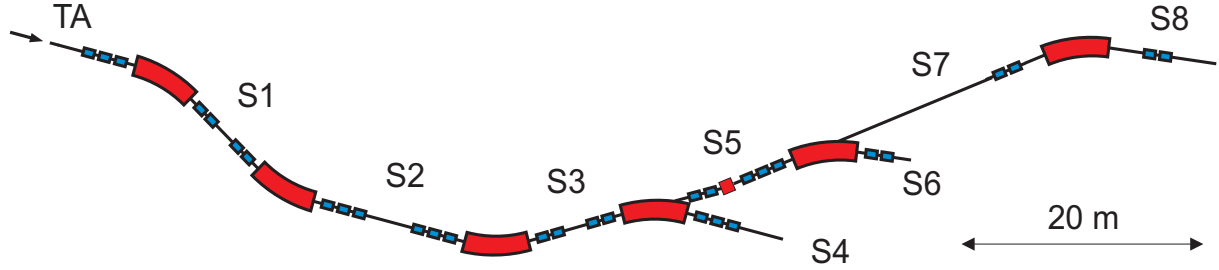


Figure 15: Layout of the GSI accelerator complex. A description of the particle path is given in the text. Taken from [29].



(a) Beamline from the SIS-18 to the Fragments Separator (FRS), to the entrance of Cave C.



(b) Zoom into the Fragment Separator (FRS). Showing the target area (TA), the different focal planes (S1 to S8).

Figure 16: Layout of the GSI accelerator complex with details on the FRS area. TA = target area for fragmentation of the primary  $^{40}\text{Ar}$  beam at the FRS, S2 and S8 = focal planes with scintillators for ToF-measurements for identification of the secondary particles. Both graphs taken from [30].

### 3.2 Overview of the LAND/R3B-Setup

In the following I describe the R3B setup, concentrating on the detectors that were important for the analysis described in this thesis. The data and facts summarized here are strongly based on the theses of [29, 31, 32]. A schematic view of the LAND/R3B Setup can be seen in fig. 17.

The setup was developed for kinematically complete measurements, meaning all of the outgoing reaction products (heavy fragment, neutron and gamma radiation) had to be detected. This allowed the reconstruction of the excitation energy spectrum via the invariant mass method.

The first two detectors, POS and PSP, were used to identify the incoming particles. The POS (section 3.3.2) performed the time-of-flight measurement and the PSP (section 3.3.3) was used to identify the charge of the incoming particle via energy loss measurements. The reaction target (section 3.4) was surrounded by a NaI crystal sphere (section 3.5.2) for the detection of gamma radiation (stemming from the decay of excited states of the reaction product) and protons. Furthermore, upstream and downstream of the target there were each two DSSSDs (Double Sided Silicon Strip Detectors, section 3.3.5) which performed energy loss and position measurements to allow a precise tracking of the incoming and outgoing particles. Afterwards, the reaction products passed through the ALADIN magnet (A LArge DIpole magNet, section 3.5.3). While the charged particles were deflected according to their velocity and mass-over-charge ratio, the neutral particles, i. e., neutrons, were not affected and impinge directly onto the LAND (Large Area Neutron Detector, section 3.5.6) which is placed 12.6 m from the reaction target. Due to the high velocity of the impinging  $^{20}\text{N}$  isotopes, the neutrons were strongly forward boosted. Thus, LAND was operated in a full acceptance mode even with a distance of 12.6 m from the reaction target. The heavy fragments, deflected by ALADIN, were tracked by two GFIs (Großer FIBer Detektor, section 3.5.4) which are mandatory for the mass identification via precise position measurements. Afterwards, the TFW (The Fragment Wall, section 3.5.5) performed a time-of-flight and energy loss measurement to identify velocity and charge of the outgoing heavy fragment.

Furthermore, there was a proton branch with dedicated detectors which is not important for the reaction described in this thesis but mentioned for completeness. The PDCs (Proton Drift Chamber) performed the tracking of the fast outgoing protons and the DTF (Dicke Time-of-Flight Wand) was used to measure the time-of-flight and energy loss.

Distances were determined by photogrammetric techniques and are shown in table 2.

ALADIN was filled with Helium gas. All detectors upstream of ALADIN were placed in a vacuum beam pipe. The detectors downstream were exposed to air.

### 3.3 Detectors for Identifying the Incoming Particles

As the FRS delivered many different nuclei in the cocktail beam separated by their A/Z-ratio resulting in different velocities, the first two detectors in Cave C (together with the S8 detector at the FRS) performed the identification of the incoming particles. The charge was determined by energy loss measurements of the PSP detector. The Bethe-Bloch equation which describes the energy loss of a particle traversing matter was utilized to calculate the charge number Z of the incident ion:

$$-\frac{dE}{dx} = \frac{4\pi}{m_e c^2} \cdot \frac{nZ^2}{\beta^2} \left( \frac{e^2}{4\pi\epsilon_0} \right)^2 \cdot \left[ \ln \left( \frac{2m_e c^2 \beta^2}{I(1 - \beta^2)} \right) - \beta^2 \right], \quad (17)$$

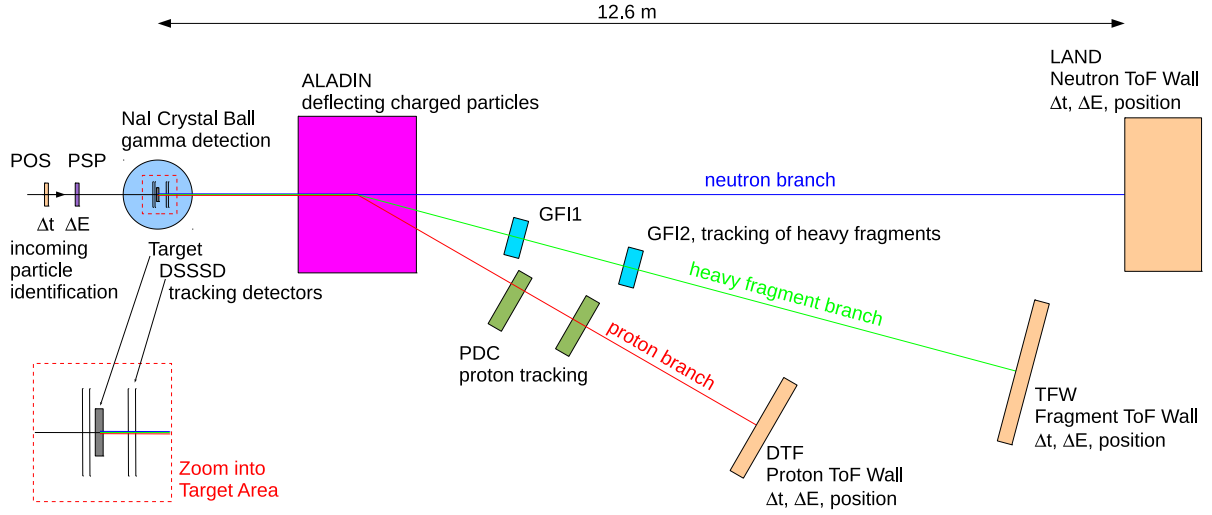


Figure 17: Sketch of the detector setup at the LAND/R3B-Cave. Plastic scintillators are colored orange, neutron beam: blue line, heavy ion branch: green line, proton beam: red line.

where  $\beta = v/c$ ,  $v$  is the velocity of the particle,  $c$  is the speed of light,  $E$  is the energy of the particle,  $x$  is the path length of the particle,  $Z$  is the charge number of the particle ( $Z \cdot e = \text{charge of the particle}$ ),  $\epsilon_0$  is the permittivity of free space,  $e$  is the elementary charge,  $n$  is the electron density of the material,  $m_e$  is the rest mass of the electron,  $I$  is the mean excitation potential of the material.

The mass number  $A$  was determined by time-of-flight measurements between the S8 detector at the end of the FRS and the POS detector at the entrance of Cave C (145 cm upstream of the target). By knowing the path length of 55 m, one can calculate the velocity of the incident particle by

$$\beta = \frac{v}{c} = \frac{d_{\text{S8-POS}}}{\text{ToF} \times c} . \quad (18)$$

Following equation (16) the  $A/Z$  ratio was determined with

$$\frac{A}{Z} = \frac{B\rho}{\beta\gamma} . \quad (19)$$

While the magnetic rigidity  $B\rho = 9.88 \text{ Tm}$  is defined by the FRS setting and its beamline,  $\beta$  and  $\gamma$  are only velocity dependent.

Together with the charge of the incident particle determined with the PSP measurements, the particle is well identified and can be selected for further analysis. A plot of the incoming particle identification is shown in fig. 25.

### 3.3.1 S8 at FRS

The S8 was a 3 mm thick plastic scintillator with a length of 20 cm and a height of 10 cm located at the focal plane S8 directly behind the FRS. It was read out at two ends with photomultipliers providing time and energy information although only the timing information was used as a start signal for the time-of-flight measurements to Cave C. In combination with the timing information of the POS detector, one can identify the mass-over-charge ratio of the secondary particle delivered by the FRS.

### 3.3 Detectors for Identifying the Incoming Particles

Detector	x [cm]	y [cm]	z [cm]	task / measuring
POS	0	0	-145.2	A/Z ratio of incoming particle
PSP	0	0	-105.3	charge of incoming particle
ROLU	0	0		active slit
SST1	0.02	0.03	-6.44	tracking of incoming particle, energy loss
SST2	-0.03	0.01	-3.68	tracking of incoming particle, energy loss
SST3	0.06	-0.09	11.11	tracking of outgoing particle, energy loss
SST4	0.13	-0.06	13.88	tracking of outgoing particle, energy loss
XB	0	0	0	angle and energy of gammas and protons
ALADIN	0	0	260.0	deflection of charged particles for outgoing particle identification
Veto	0	0	$12.5 \cdot 10^2$	supression of charged particles and gammas for LAND
LAND	4.80	0.00	$13.1 \cdot 10^2$	ToF, position and angle of neutrons
GFI1	-56.50	2.30	467.10	tracking of heavy fragments, mass identification
GFI2	-95.10	3.30	616.60	tracking of heavy fragments, mass identification
TFW	-231.60	7.30	1120.80	charge, ToF, y-coordinate of heavy fragments

Table 2: Summary of the detectors in the LAND/R3B setup providing the x-, y- and z-coordinates of the centre of each detector (provided by Marcel Heine via photogrammetry), and their purpose. The origin of the coordinate system is in the centre of the reaction target. Only detectors important for the presented reaction are listed.

#### 3.3.2 POS

The POS was a square shaped scintillator with dimensions of  $2.5 \text{ cm} \times 2.5 \text{ cm}$  and a thickness of  $0.1 \text{ cm}$ . It was providing a time resolution of  $\sigma_{t,\text{POS}} = 25 \text{ ps}$ , thus, well capable for defining the stop signal of the incoming ToF-measurements and the start signal of the ToF-measurements of the reaction products behind the target. The POS was read out at four sides with photomultipliers using light guides providing time and energy information. In this experiment, only the time informations were used for investigation of the velocities ( $\beta_i$ ) of the incoming particles by building the average of the four timing signals. A schematic view of the POS is presented in figure 18.

#### 3.3.3 PSP

Downstream, the PSP (Position Sensitive Pin diode) realized an energy loss measurement ( $\Delta E$ ) to examine the charge (Ze) of the incoming particle. It is an n-type silicon detector with a square shape of  $4.5 \text{ cm} \times 4.5 \text{ cm}$  and a thickness of  $300 \mu\text{m}$ . The front side of the detector is implanted with boron to form a pn-junction which was used as anode (resistive electrode) with four read out pins at each corner. Reading out each of these pins separately one can determine the position of the interaction providing a position resolution of  $\sigma_{\text{pos,PSP}} = 200 \mu\text{m}$ . But as there was no good calibration run available, the position information was not used during this experiment. The back side was used as cathode (conductive electrode) and read out with one pin. As the charge induced at the read out pins is proportional to the number of electron-hole pairs produced by the traversing ion, the total energy loss can be measured with a resolution of 1%, providing



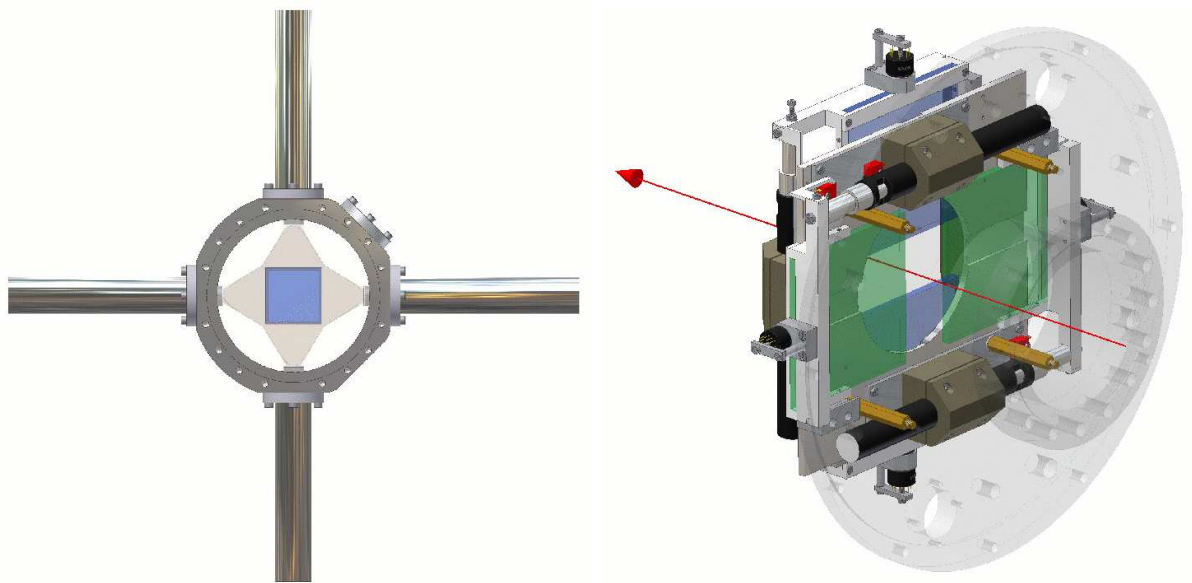


Figure 18: Layout of the POS [33] (left panel). Technical sketch of the ROLU active slit detector [34] (right panel).

the basis of the charge determination via the Bethe-Bloch equation (equation 17).

### 3.3.4 ROLU

The ROLU (Rechts Oben Links Unten = German for "Right Up Left Down") was used as a veto detector to adjust the accepted beam spot size on the target. It consisted of four 5 mm thick plastic scintillator sheets (two horizontally and two vertically) that were arranged in that way that they formed a slit/window in the center. Each of them was read out by a photomultiplier and could be moved with a step motor to adjust the size of the central window (usually ca.  $2 \times 2 \text{ cm}^2$ ). If an ion hit one of the scintillator sheets, producing a signal in the ROLU, the event was excluded from recording to tape. If the ion passed the central window without producing a signal in the ROLU, the event was accepted to be recorded to tape. A Layout of the ROLU is given in figure 18.

### 3.3.5 DSSSD

The Double Sided Silicon Strip Detectors (DSSSDs or SSTs) were used for energy loss measurements (for charge determination) and position measurements for precise tracking of the particles providing a position resolution of  $\sigma_{\text{pos}} \approx 100 \mu\text{m}$  [31]. Together with a precise knowledge of the distance between the in beam DSSSDs, one can derive the angle of the incoming and outgoing particles.

The DSSSDs were semiconductor based detectors with an area of  $72 \times 40 \text{ mm}^2$  and a thickness of 0.3 mm [31]. They consisted in total of 1024 silicon strips.

640 strips were located perpendicular to the long edge (s-side or p-side) of the detector measuring the x-direction of the traversing charged particle. Its implantation pitch had a size of  $27.5 \mu\text{m}$ . But as only every fourth strip was read out, while the other strips were left floating, the resulting read out pitch was  $110 \mu\text{m}$ .

The remaining 384 strips were placed in parallel to the long edge (k-side or n-side) of the DSSSD measuring the y-direction of the traversing charged particle. The implantation

pitch size of the k-side amounted to  $104\ \mu\text{m}$  while reading out every channel.

In total eight DSSSD were placed in the setup, two directly in front of the target to measure the incoming particles, two after the target to investigate the outgoing reaction products and four around the target (building a box) to examine protons from quasi-free breakup reactions at large polar angles [30].

### 3.4 Reaction Targets

The reaction targets were mounted in a remotely controllable target wheel which was moved with a step motor. They had an area of  $3 \times 3\text{ cm}^2$  with a specific thickness. A lead target was used to provide the Coulomb field which acts as virtual photon field. A carbon target was providing the nuclear contribution to the reaction which had to be subtracted. Beside that, also data with no target were recorded to estimate the contribution of the beamline, in especially, the different detectors, the Helium gas in ALADIN, and the air behind the ALADIN exit window. The target material, their thicknesses, and their type of contributions are summarized in the following table 3.

Target	Thickness [mm]	Density [g/cm <sup>3</sup> ]	Areal Density [g/cm <sup>2</sup> ]	Contribution to the Reaction
Pb	0.176	11,342	<b>1.99</b> ( $\pm 0.04$ )	Beamline, Nuclear, Coulomb
C	<b>5,08</b> ( $\pm 0.1$ )	1,84	0.93	Beamline, Nuclear
empty	-	-	-	Beamline

Table 3: Reaction targets employed during the experiment described here. Bold values are results of measurements (private communication within the collaboration). The density of graphite was given by the manufacturer.

## 3.5 Detectors for Identifying the Reaction Products

### 3.5.1 DSSSD

In addition to the DSSSDs for the incoming particle tracking, two DSSSDs were used at distances of 11.1 cm and 13.8 cm behind the target for tracking of the reaction products. For further details see section 3.3.5.

### 3.5.2 NaI Crystal Ball

The Crystal Ball was a  $4\pi$  gamma detector consisting of 162 sodium iodide crystals with a length of 20 cm, each read out by a photomultiplier tube. The crystals were arranged in a sphere with an inner diameter of 50 cm and an outer diameter of 90 cm requiring different shapes of the crystals. 12 of them were pentagonally and 150 hexagonally shaped. Independent of its shape, the accuracy with which the angle could be defined was  $14^\circ$ . The high granularity of the Crystal Ball enabled the possibility of a Doppler correction, but it also made an addback routine necessary (described in section 4.8). A summary of the detector characteristics is presented in table 4.

In the forward hemisphere, there were 64 crystals used for proton detection. This was done, reading out the PMTs at the last dynode (omitting the final amplification stage) resulting in a low-gain energy readout. In this thesis, the proton readout was not used, further details on the Crystal Ball proton detection can be extracted from ref. [30].



Total efficiency	$E_\gamma = 1.3 \text{ MeV}$	0.96
	$E_\gamma = 3.0 \text{ MeV}$	0.90
Full energy efficiency	$E_\gamma = 1.3 \text{ MeV}$	0.71
	$E_\gamma = 3.0 \text{ MeV}$	0.56
Total energy resolution	$M_\gamma = 20$	18 - 22%
Multiplicity (M) resolution	$M_\gamma = 20$	25 - 30%
Intrinsic energy resolution (single crystal)	$E_\gamma = 662 \text{ keV}$	7.8%
	$E_\gamma = 1.3 \text{ MeV}$	5.5%
Time resolution (single crystal)		2.8 ns

Table 4: Characteristic values of the NaI Crystal Ball [35].

### 3.5.3 ALADIN

ALADIN (A LARge DIpole magNet) was an electrically operated dipole magnet with massive iron yokes. Its magnetic field deflected the charged heavy reaction products ca.  $15^\circ$  from the nominal beam axis according to their mass-over-charge ratio while neutrons were left unaffected. In order to keep parasitic nuclear reaction of the reaction products to a minimum, its gap was filled with He gas under normal pressure. It has an acceptance of  $\pm 60 \text{ mrad}$ , a gap height of 0.5 m and a depth of 1.54 m. ALADIN was operated at a current of  $I \approx 2500 \text{ A}$ , resulting in a magnetic field strength of  $B = 1.66 \text{ T}$ .

### 3.5.4 GFIs

Two GFIs (Großer Fiber Detektor) were placed in the fragment branch to identify the masses of the heavy fragments via their deflection in the magnetic field by precise x-position measurements. Beside that, they also were used to track the heavy charged reaction fragments, thus, they were important for the reconstruction of the excitation energy.

The GFIs had an area of  $50 \text{ cm} \times 50 \text{ cm}$  and consisted of 475 thin scintillating fibres with a square-shaped cross section of  $1 \text{ mm} \times 1 \text{ mm}$ . The fibres were placed vertically in parallel directly next to each other. They were coated with reflecting material and white paint to guide the light through the fibres and to avoid crosstalk between neighbouring elements. The ends of the wires were glued to a two dimensional mask which was coupled to a position sensitive photomultiplier (PSPM). If a heavy fragments hits a fibre, light is produced and travelling through the wires onto the photocathode. The anode of the PSPM consists of a rectangular grid of  $18 \times 16$  wires which provided a sufficiently high position resolution (for ions with  $Z \geq 3$ ) to relate the position on the PSPM to the fibre element that was hit. Thus, the position resolution equals the dimension of the fibre wires of 1 mm.

### 3.5.5 TFW

The TFW (Time of Flight Wall) was used for time and energy loss measurements to identify the velocity and the charge of the heavy reaction products and provided low resolved position information. It was consisting of 32 plastic scintillator paddles, each read out with PMTs on both ends. The first plane was built up of 14 vertical paddles with a length of 147 cm and the second one of 18 horizontal paddles with a length of 189 cm. Each paddle had a height of 10 cm and a depth of 0.5 cm. The crossing paddles provide

the advantage of having four time and energy measurements and an easier synchronization between the particular paddles in both planes. The calibration and synchronization procedures of long plastic scintillator based detectors will be described in section 3.5.6.

The expected time resolution is  $\sigma_t = 100$  ps [29]. A schematic layout of the TFW is provided in figure 19.

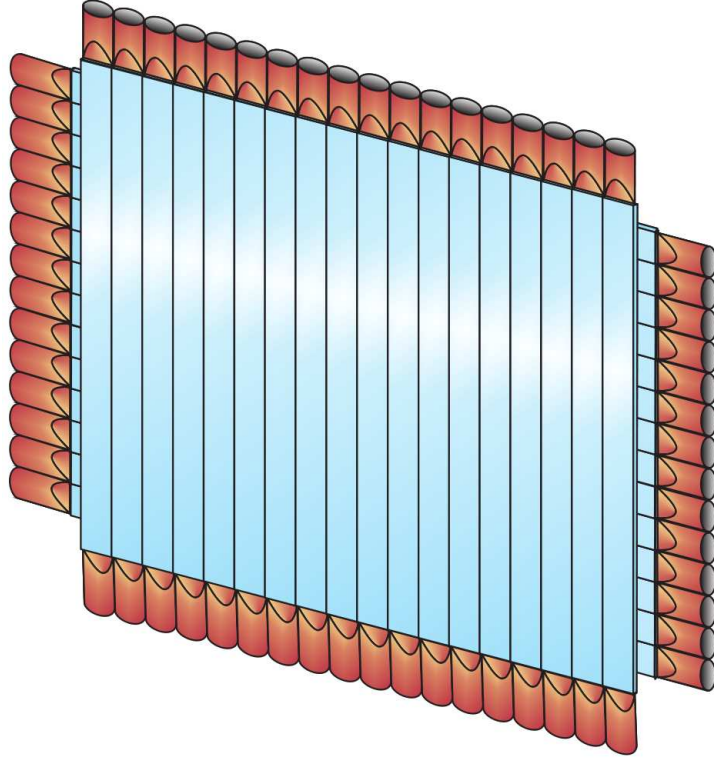


Figure 19: Schematic Drawing of the TFW scintillator array [29].

#### 3.5.6 LAND

The purpose of LAND (Large Area Neutron Detector) was to measure the time-of-flight and the position of fast neutrons with kinetic energies between 100 and 1000 MeV. It provided an efficiency for a single neutron with 400 MeV kinetic energy of 90 % [32,36], a time resolution  $\sigma_t = 250$  ps [32] and a position resolution of 7-10 cm due to the granularity of the array and the time-difference method [36]. Thus, it was possible to reconstruct the momenta of the neutrons originating from nuclear reactions in the target and to reconstruct the relative energy spectrum of the reaction.

LAND was a 2 m long and 2 m wide scintillator array with a depth of 1 m. Due to its large area it covered an angular acceptance of 80 mrad at a distance of 12.6 m from the reaction target. It consisted of 10 planes with 20 scintillator paddles each. The planes were arranged subsequently with horizontally and vertically orientated paddles. Each paddle had a square shaped cross section of 10 cm  $\times$  10 cm and was read out at both ends by a PMT. In order to convert the not detectable neutrons into detectable charged particles, the paddles were built up of a sandwich structure of subsequently 5 mm iron converter and 5 mm scintillator sheets. Further details can be found elsewhere [36,37].

Directly in front of LAND there was the Veto detector. It was used to identify and suppress charged particles and gammas impinging onto LAND. It was built of two

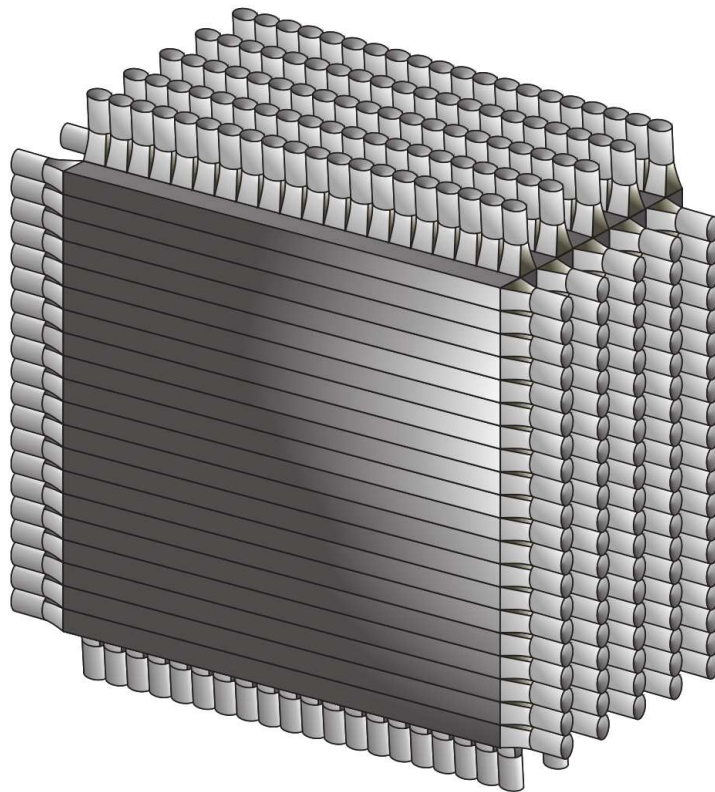


Figure 20: Schematic Drawing of the LAND scintillator array. Taken from [29].

crossed layers each consisting of 20 scintillator strips, The strips with dimensions of  $200\text{ cm} \times 10\text{ cm} \times 0.5\text{ cm}$  were read out at both ends with PMTs to gather position and ToF information [37].

### 3.5.7 land02 Framework

The data analysis and calibration of the detectors were done utilizing the land02 framework, which originally was written by Håkan Johanson [38]. It provided software for unpacking lmd-files to root-files, for the extraction of calibration parameters for the different detectors in the setup and to convert the raw data of the TDCs and QDCs with its arbitrary units into proper physics values (like times in ns, energy loss in MeV, charge numbers, x-,y-,z-coordinates in cm).

The calibration procedures done within the land02 software package will be described in the following section 3.5.8.

### 3.5.8 Calibration Procedures of Long Scintillators

1. **TDC dispersion:** The timing detectors were read out by TDCs. The TDC values needed to be (re)converted into physical time values (preferably ns). For that purpose, a so called TCAL counter gave a precise timing signal every 10 ns during the experiment. These timing signals and the referring TDC values of each channel (i.e. PMT) of a detector were recorded in the non-physics data part of the experiment files. Plotting the TCAL versus the TDC value of one PMT (compare figure 21a) one can observe a linear relation between these values. By extracting the slope and the offset by a linear fit, one can convert the TDC values into ns for each channel of

all timing detectors. The program `tcal`, a part of the `land02` framework, extracted these conversion coefficients within the `TIME_CALIB` calibration parameters based on the above described procedure.

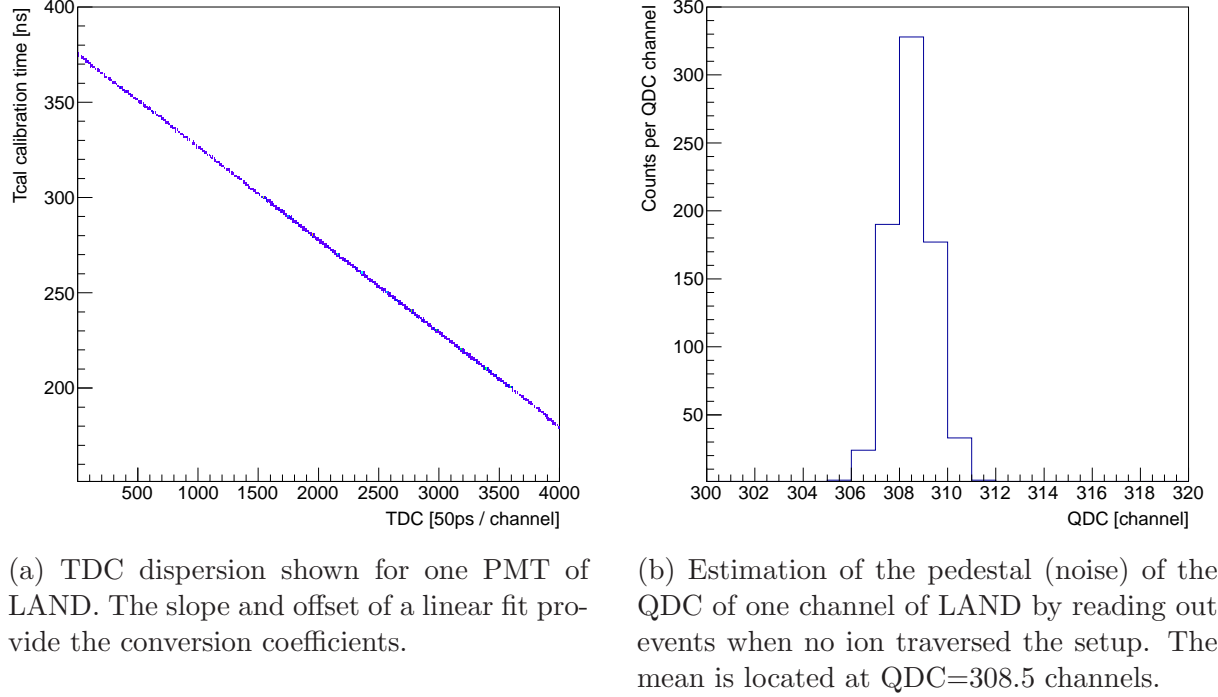


Figure 21: Time calibration and pedestal estimation.

**2. PEDESTAL subtraction:** The particles traversing a detector undergo energy loss which, in the end, leads to an electrical signal. These signals were digitized by Charge-To-Digital converters (QDC) which measured a voltage on an internal capacitor. This capacitor was charged by the signal of the detector and a small current ( $I_{\text{ped}}$ ) provided by the QDC itself. During the length of the readout gate of the QDC this current summed up to a charge called pedestal ( $I_{\text{ped}} \cdot t_{\text{gate}}$  while  $t_{\text{gate}}$  is the time when the gate is open for reading out the QDC). For further analysis, this pedestal had to be subtracted from physics data for each QDC channel in order to estimate the energy loss properly. To determine the pedestal, a clock counter triggered the readout of the detectors within regular time intervals. A program called `clock` collected data of non-physics events (meaning no ion passed the setup) which are depicted in figure 21b. In the majority of these non-physics events only the pedestal was recorded (beside a tiny fraction of muons passing a detector). Then, a Gauß-fit provided the mean and the width of the pedestal. These values were provided by the `ZERO_NOISE` calibration parameter of the `land02` framework, which then subtracted the pedestal for further analysis.

**3. Synchronization of PMTs within one paddle:** The synchronization of the PMTs within one paddle of a scintillator based detector was done using cosmic muons (for LAND and TFW). For the TFW, also ions irradiated over the whole detector area (by changing the current of the ALADIN magnet) could be used for that purpose. The crossing paddles of the LAND (and also of TFW) provide a lattice/grid which was used for a rough position calibration depending on the paddles that fired during a muon traversed the detector. Then, time and energy calibration parameters could

be calculated, which was done by the program `cosmic1` of the `land02` framework:

**Time:** Based on the roughly estimated hit position and the known length of the paddle, the time which the light needed to travel from the hit position to each end of the paddle was estimated. From that, the offset between both timing signals is derived. Beside that, also the speed of light in the paddle could be extracted, which is important for the reconstruction of the hit position by the time-difference method. These values were provided in the `TIME_DIFF_OFFSET` calibration parameters of the `land02` framework.

**Energy:** Similarly, the QDC offset between both ends of a scintillator was extracted and the attenuation coefficient was calculated, which is mandatory for the estimation of the hit position based on energy measurements (i.e. when no timing signals were present). These values were given in the `ENERGY_DIFF_GAIN` calibration parameters in the `land02` framework.

4. **Synchronization of neighbouring paddles:** This was also done using cosmic muons with the `cosmic1` program. In that stage, the time and energy values of both PMTs in one paddle are already synchronized (previous step).

**Time:** Here, the cosmes were assumed to hit subsequent paddles simultaneously. Comparing the average timing signals of both PMTs of the first paddle to those of the second paddle, the difference, and thus, the offset could be calculated in order to synchronize each paddle of the detector to the other. For the LAND detector, the muon track could be calculated through the whole array. This could be used to correct for the time offset between the signal of the same muon at the beginning of the detector and the end of the detector. This value is provided by the `TIME_SYNC_OFFSET` calibration parameter.

**Energy:** As the cosmic muons had very high kinetic energy, and thus, were minimum ionizing (meaning the energy loss is very small in contrast to the kinetic energy), they were assumed to loose energy rather constantly while traversing the entire detector (TFW and even LAND). Thus, the energy detected by two subsequently hit paddles should be constant. In that way, an energy synchronization of all paddles along one scintillator detector (LAND or TFW) could be realized. The energy offsets between the paddles were given within the `ENERGY_SYNC_GAIN` calibration parameter.

5. **Time synchronization of all detectors in the setup:** In order to synchronize all the timing detectors in the setup, two methods were possible. Either, high energetic photons (gammas) stemming from reaction at the reaction targets could be utilized. Knowing their velocity (speed of light) and the precise distance to the target (12.6 m), the expected time offset could be calculated. Or, switching of the bending magnet and having no target in the beam, ions could be used in the same manner with their velocity derived from the incoming particle detectors (the latter method was mainly used for the TFW).

### 3.6 Energy Measurement in Long Scintillators – The Smiley-Effect

In the following section, I describe the attenuation of light in long scintillators. This work was done in order to investigate the so called Smiley-Effect, meaning that the total detected light (meaning energy) is not independent from the hit position of an impinging particle and to examine the origin of this effect.

#### 3.6.1 Light Attenuation in Scintillators

The basic way for describing light attenuation in long scintillators is using a simple exponential decay law for the intensity of the light traveling through the scintillator bar like,

$$\text{energy detected left: } e_1 = E \cdot e^{-\lambda \cdot x} , \quad (20)$$

$$\text{energy detected right: } e_2 = E \cdot e^{-\lambda \cdot (L-x)} , \quad (21)$$

where  $E$  is the total deposited energy in the scintillator,  $\lambda$  is the attenuation length,  $L$  is the length of the scintillator,  $x$  is the position where the particle hit the scintillator. Here, reflections are omitted as they are thought to cause no loss of light inside the scintillator. These can be combined to a total detected energy in the scintillator

$$\begin{aligned} \sqrt{e_1 e_2} &= E \sqrt{e^{-\lambda x - \lambda(L-x)}} , \\ \sqrt{e_1 e_2} &= E \sqrt{e^{-\lambda L}} , \\ \sqrt{e_1 e_2} &= E \cdot \text{const}_1 , \\ &\text{with } \text{const}_1 = e^{-\lambda L} , \end{aligned} \quad (22)$$

suggesting that the total measured energy is independent from the position where the particle hit the detector and gives directly the total deposited energy of the particle (within a constant linear conversion factor).

Reorganizing equations 20 and 21 enables conclusions on the hit position based on the energy measurements.

$$\begin{aligned} \frac{e_1}{e_2} &= \frac{E \cdot e^{-\lambda \cdot x}}{E \cdot e^{-\lambda \cdot (L-x)}} , \\ \frac{e_1}{e_2} &= e^{-\lambda \cdot x + \lambda \cdot (L-x)} , \\ \frac{e_1}{e_2} &= e^{-2\lambda x} \cdot \text{const}_2 , \\ &\text{with } \text{const}_2 = e^{\lambda L} , \end{aligned} \quad (23)$$

During the experiment, this method was used to reconstruct the hit position when no time information was present (e.g., when the signal did not exceed the threshold of the TDC). A sketch of the light propagation in long scintillators can be found in figure 22.



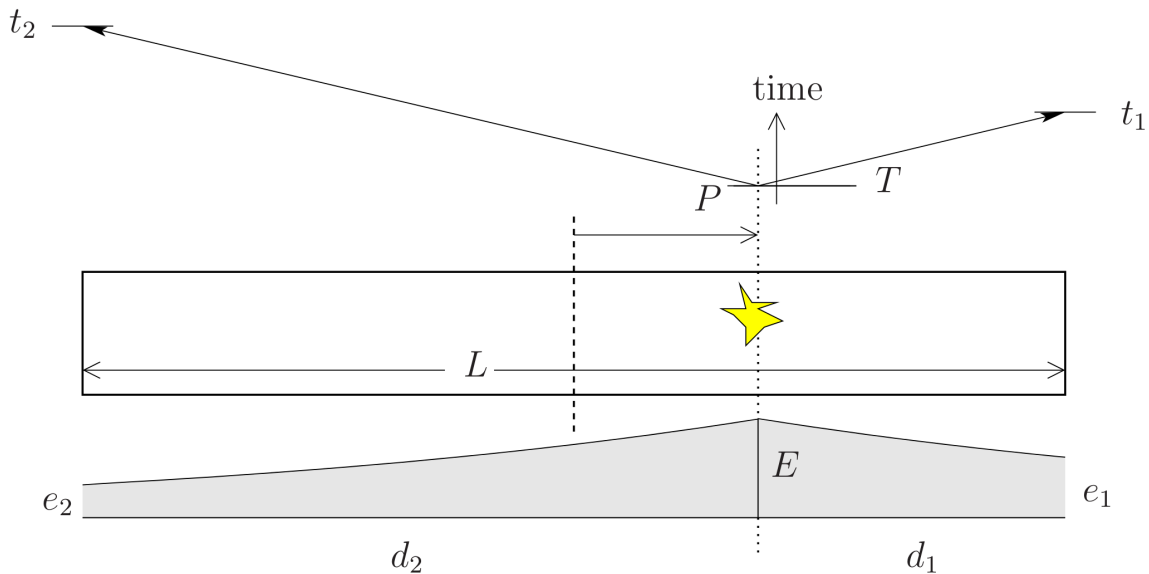


Figure 22: Light propagation in a scintillator paddle. Shown is the scintillator bar (of length  $L$ ) with the emission of scintillation light (yellow symbol). The energy loss is depicted in the lower part,  $E$  is the deposited energy,  $e_1$  and  $e_2$  are the detected energies at the right and left PMT, respectively (note the opposite notation in the text, e.g., eq. 20). In the upper part, the time measurement is illustrated, where  $T$  is the time when the event occurred,  $t_1$  and  $t_2$  are the detected times at the right and left PMT, respectively. Taken from [38].

### 3.6.2 Extracting Energy and Position of Impinging Cosmic Muons

In order to check eq. 22, one needs to irradiate LAND with particles with a rather constant energy loss all over the detector. Therefore, cosmic muons with a  $\beta \geq 0.7$  provide a good tool. A code, called `muon1`, was written by Håkan Johansson as part of the `land02` software package to extract the energy and position informations of these impinging cosmic muons which works as follows. The LAND detector consists of scintillator bars (called paddles) while 20 of these paddles form one plane. These planes are arranged subsequently in horizontal and vertical direction. Thus, the crossing paddles within the subsequent planes provide a kind of lattice which can be used to extract a hit position of impinging muons independent of the measured time or energy information. When a muon passes through the detector, based on these lattice points a path length can be calculated. This is important to derive an energy normalisation. If the particle passes the detector (respectively a paddle) perpendicular to the surface, the path length is one. If it passes in an angle of  $45^\circ$  to the x-z-plane but  $0^\circ$  to the y-z-plane, the path through the detector extends to  $\sqrt{1+1} = 1.414$  of the detector thickness, so the deposited energy of the particle is also 1.414 times larger than in the perpendicular case. Thus, the detected energy needs to be divided by the path length to get a detected energy per unit length (i.e. the paddle/detector width). The result of the detected energy as a function of the hit position can be seen in figure 23, showing that the total detected energy, beside the theoretical reflections in eq. 22, is not independent of the hit position. The profile plot (red plus signs) ranges from 660 to 740 a.u. for the total detected energy resulting in a 12 % deviation from the mean value at 691 a.u.

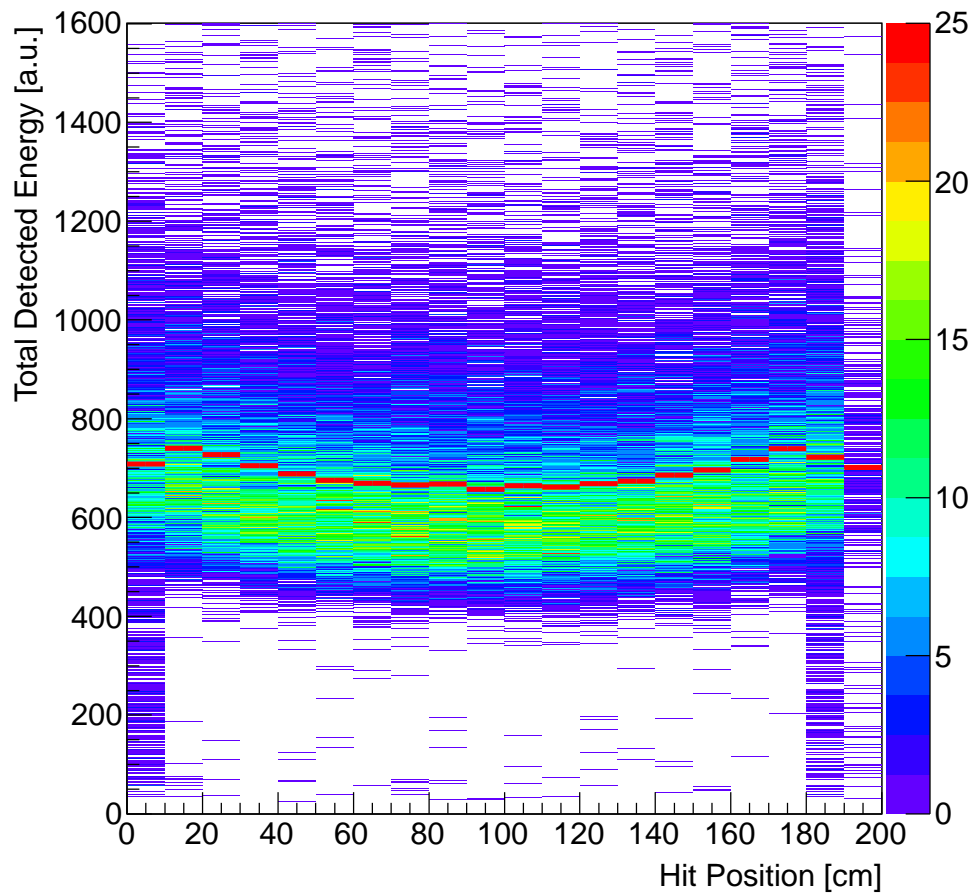


Figure 23: Energy loss as function of the hit position as determined by crossing paddles. The thick red line represents a profile plot of the underlying 2D histogram with a mean value of the total detected energy at 691 a.u. and a range of 660 to 740 a.u., resulting in a 12 % deviation.

### 3.6.3 Simple Smiley Calculations in 2D

As seen in the previous paragraph, a simple exponential decay law is not sufficient to describe the attenuation of light in scintillators. Figure 23 is suggesting additional losses due to a process that is not yet understood.

When a particle undergoes energy loss inside the scintillator, light is emitted isotropically. The larger the angle of the emitted photon within the x-y-plane of a paddle, the larger is the path that the light has to travel until it reaches the end of the scintillator bar where it is detected by a photomultiplier tube (PMT). Thus, the attenuation is not only depending on the hit position but also on the longer path length the light has to travel when emitted not parallel to the x-direction. Due to the longer path length also an additional light attenuation is expected.

Furthermore, when the light is reflected at the upper or lower edges of the scintillator bar while traveling towards the PMTs, depending on the angle it can undergo non-total reflection resulting in additional losses each time the light is reflected at the edges when its incident angle is larger than the critical angle. Therefore, a code was written in the framework of this thesis, which takes the additional path length and the additional losses due to non-total reflections at the edges of the scintillator into account in order to simulate



this “Smiley“ in two dimensions (x-y-plane of the scintillator bar).

The code calculates the energy loss based on the following equations:

$$\text{energy detected left:} \quad e_1 = E \cdot e^{-\lambda p_1} (R)^{n_1} , \quad (24)$$

$$\text{energy detected right:} \quad e_2 = E \cdot e^{-\lambda p_2} (R)^{n_2} , \quad (25)$$

with:

$$\text{path to the left PMT:} \quad p_1 = \frac{x}{\cos(\phi)} ,$$

$$\text{path to the right PMT:} \quad p_2 = \frac{L - x}{\cos(\phi)} ,$$

$$\text{number of reflections left:} \quad n_1 = \frac{x}{h \cdot \tan(\theta)} , \quad \text{with } n \in \mathbb{N} ,$$

$$\text{number of reflections right:} \quad n_2 = \frac{L - x}{h \cdot \tan(\theta)} ,$$

where  $R$  is the reflectivity of the surface (the fraction of light that is reflected back into the scintillator bar after hitting the edge). Furthermore,  $\lambda = 1/117$  is the attenuation length in 1/cm [37].

Beside that, following assumptions were made in order to provide the calculations with reasonable parameters: If the light hits the surface of the scintillator bar with an angle  $\theta$  (measured from the long edge of the scintillator) below the critical angle

$$\theta_{\text{critical}} = \arcsin \left( \frac{n_{\text{air}}}{n_{\text{Scint}}} \right) = 39.3^\circ , \quad (26)$$

where the refractive index of the scintillator material is  $n_{\text{Scint}} = 1.58$  [37], the refractive index of air is  $n_{\text{air}} = 1.00$ , it undergoes total reflection ( $R=1$ ).

If  $\theta$  is greater than  $\theta_{\text{critical}}$ , the light undergoes non-total reflection meaning it transits out of the scintillator onto the wrapping and is reflected backwards into the scintillator. The reflectivity of the wrapping is assumed to be  $R_{\text{wrapping}} = 1.00$  while the reflectivity from the wrapping back inside the scintillator is assumed to be

$$R_{\text{out} \rightarrow \text{in}} = \left( \frac{n_{\text{Scint}} - n_{\text{air}}}{n_{\text{Scint}} + n_{\text{air}}} \right)^2 \quad (27)$$

based on Fresnel’s law, where the refractive index of the scintillator material is  $n_{\text{Scint}} = 1.58$  (based on data by [37]), the refractive index of air is  $n_{\text{air}} = 1.00$  (needed for a gap between the scintillator and the wrapping). Then, the entire reflectivity due to non-total reflection is

$$R_{\text{untotal}} = R_{\text{wrapping}} - R_{\text{out} \rightarrow \text{in}} = 0.9495 . \quad (28)$$

Then, for each 1 cm of the scintillator bar, a light source was applied, emitting light isotropically in the x-y plane (within  $0.1^\circ$  steps). The light attenuation was calculated as described in equations 24 and 25. The result of the calculation can be seen in figure 24.

### 3.6.4 Conclusion and Discussion

Figure 24 shows good agreement of the 2D simulation with experimentally extracted data. Although only a 2D model applied here this proves qualitatively that a simple exponential

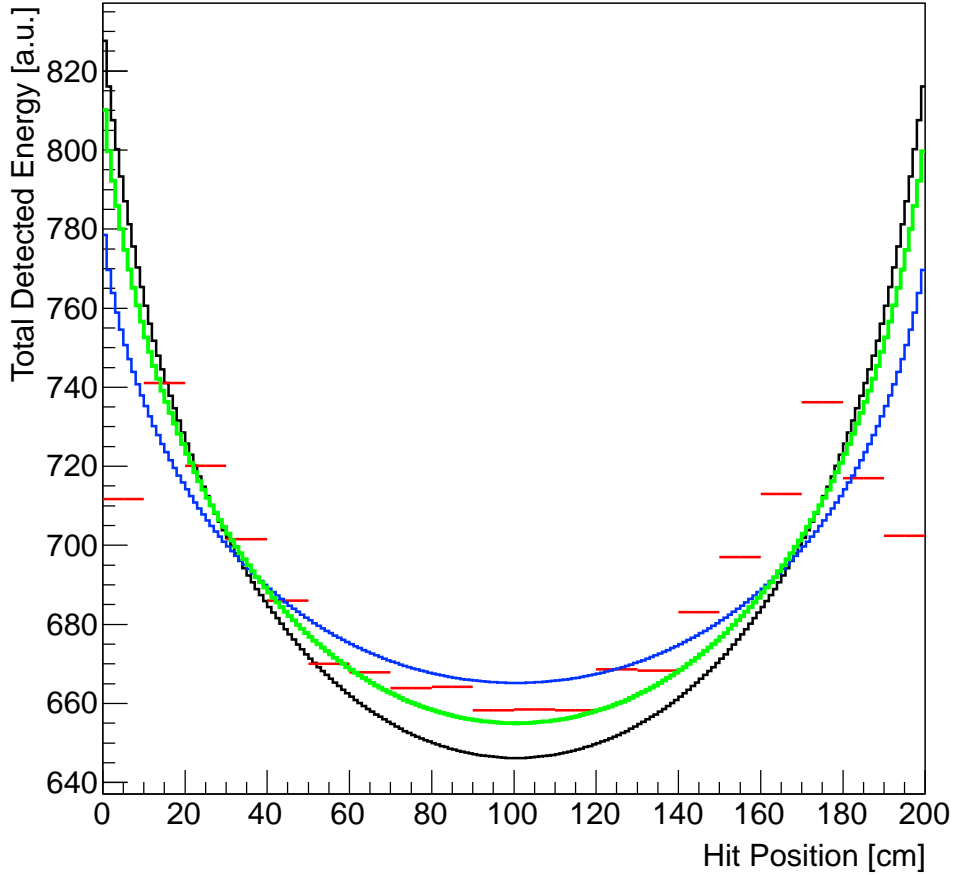


Figure 24: Comparison of calculation and experimental data. Red = measurement; Blue = total reflection (additional losses only due to path length); Black  $R = 0.95$  (worst case); Green  $R = 0.97$  (chosen to agree with the exp. data).

attenuation of light while traveling through a scintillator is not sufficient to describe these complex processes. The additional losses observed in figure 23 are caused by the additional attenuation due to the longer path length of the light, when not emitted directly towards the PMTs (blue line). Furthermore, additional losses are caused by non-total reflection at the edges of the scintillator while traveling towards the PMTs (green and black line). These additional losses cause that the total deposited energy in a long scintillator is not independent of the hit position where the scintillation light is emitted.

In order to solve this problem quantitatively one would have to expand the simulation to three dimensions. Here, only a qualitative check was envisaged trying to find the origin of the Smiley effect. Therefore, the reflectivity of 0.97 from the 2D model found to fit best to the experimental data would not hold true for the 3D model. An expansion to three dimensions would cause additional losses of the light while traveling through the scintillator. Therefore, the reflectivity of 0.97 found in the 2D model would induce a more dominant curvature in the position dependent energy measurement. Thus, the reflectivity of a 3D model would be found to be higher than 0.97.

On the other hand, the z-dimension of one scintillator paddle is only 0.5 cm, resulting in a large loss of light due to reflections in z-direction for rather low emission angles. This challenges that the light emitted in z-direction would undergo too many reflections that it can not be detected anymore at the PMT.

The observed flattening at the edges in figure 23 is not yet understood.

Although the total deposited energy is not crucial for the neutron detection, the energies detected at each end ( $e_1$  and  $e_2$ ) sometimes are needed to reconstruct an event (e.g. if one of the timing values is missing, the hit position and the missing time value are reconstructed from the single energies). Beside that, the total detected energy is crucial in other long scintillators, like the TFW for charge determination. Therefore, the consideration of the Smiley effect would improve the experimental results.



## 4 Data Analysis for $^{20}\text{N}(\gamma, n)^{19}\text{N}$ Reaction

In this section, I describe the analysis of the Coulomb dissociation reaction of  $^{20}\text{N}$  measured in the s393 experiment at the LAND/R3B cave at GSI.

### 4.1 Incoming Particle Identification

The apparatus for the identification of the incoming particles and the dedicated detectors were already described in section 3.3. The charge of the incoming particle was derived by energy loss measurements in the PSP. This was converted via the Bethe-Bloch equation into the referring charge number. The mass-over-charge ratio was determined by time-of-flight measurement between the S8 and POS detector. As the FRS separated the secondary particles according to their mass-over-charge ratio by fixing the radius of the trajectory, the accepted particles had different velocities which characterized their mass-over-charge ratio. A detailed description on the basic methods of the incoming particle identification is given in section 3.3. In that way, the particles delivered to the LAND/R3B cave could be well identified (figure 25).

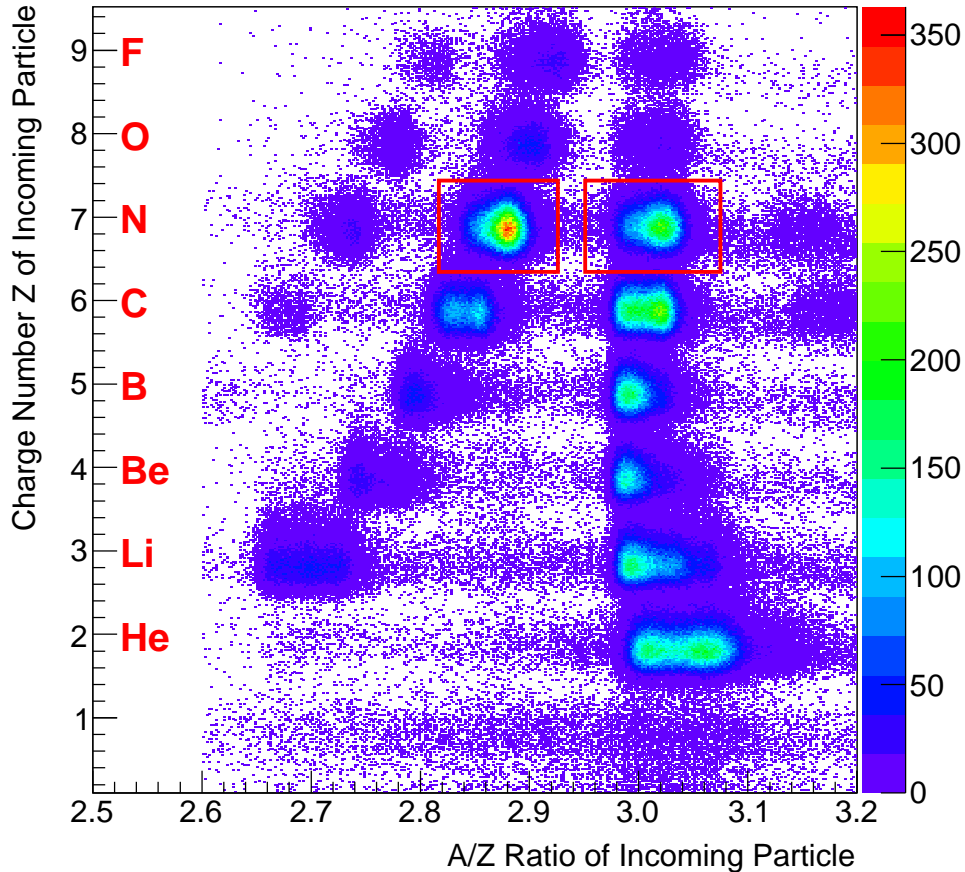


Figure 25: Incoming particle identification. The charge number  $Z$  is derived by energy loss measurements in the PSP and the  $A/Z$  ratio by time-of-flight measurements between S8 and POS (55 m distance). The red rectangles indicate the  $^{20}\text{N}$  (left) and  $^{21}\text{N}$  (right). Other nuclei included in this experiment were analyzed by several different collaborators (e.g. [32, 39]).

## 4.2 Identifying the Charge of the Outgoing Particle

The charge of the outgoing fragment was determined by energy loss measurements of the TFW (described in detail in paragraph 3.5.5). A cut was applied for further analysis between 6.5 and 8.1 MeV in order to select particles with an outgoing charge number  $Z=7$ .

Furthermore, it was investigated how this cut on the energy loss measurements would reduce the statistics and thus influence the cross section. Therefore, all runs with  $^{20}\text{N}$  impinging onto the lead target were taken into account. The deposited energy at the entire TFW while requiring a single hit in both the TFW and LAND (as in the analysis of the  $^{20}\text{N}(\gamma, n)^{19}\text{N}$  reaction) was plotted (figure 26). Diagonal impinging particles should not cause any ambiguous results as the particles are strongly forward boosted and the deflection angle due to the ALADIN magnet and the angular distribution due to the reaction are very small (with angles of max.  $\pm 0.05\text{ rad}$ ) in comparison to the long drift path from ALADIN to the TFW. A Gaussian fit was applied in the range of 6.5 and 8.1 MeV (red curve in figure 26). The integral of the Gaussian fit provides the number of events without applying the cut ( $N_{\text{Gauss}}$ ).

The number of events with the charge cut applied in the range of 6.5 and 8.1 MeV ( $N_{\text{Cut}}$ ), then, was compared to the  $N_{\text{Gauss}}$  revealing a loss of only 2.0% of the statistics.  $N_{\text{Cut}}/N_{\text{Gauss}} = 0.979$ .

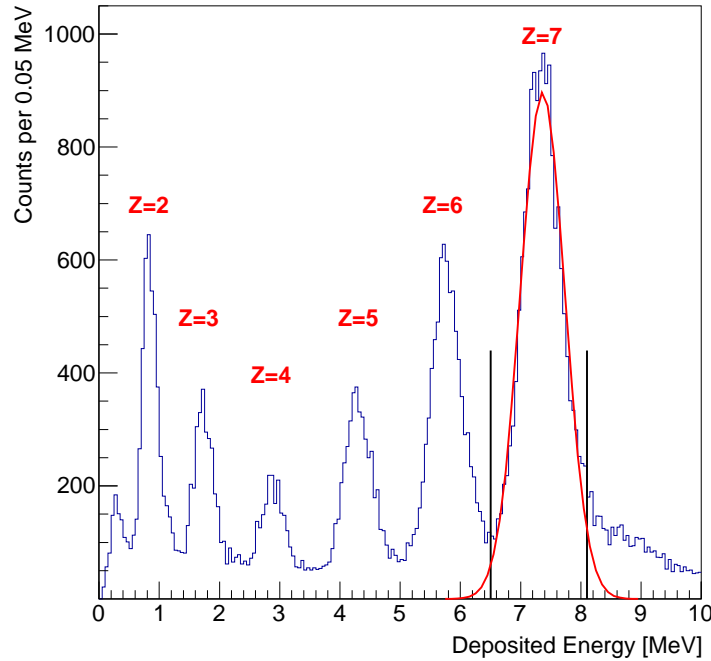
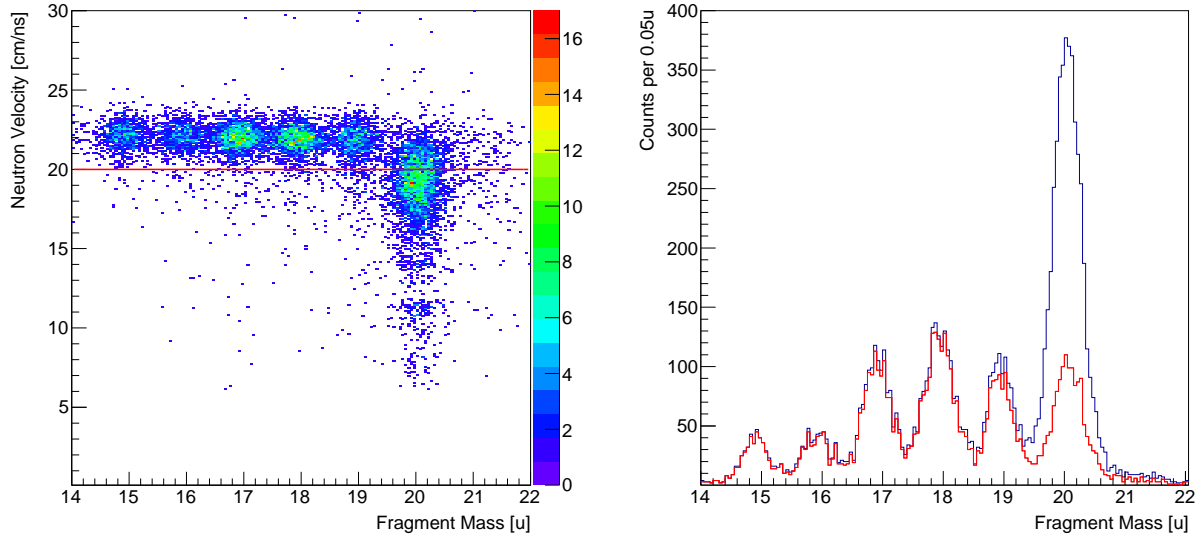


Figure 26: Energy loss measurements of the fragment ToF Wall (TFW) for identifying the charge of outgoing reaction fragments. Here,  $^{20}\text{N}$  nuclides impinge onto a Pb target. A single hit in both the TFW and LAND were required. The outgoing  $Z=7$  particles are located in the peak at 7.3 MeV. The black vertical lines at 6.5 and 8.1 MeV indicate the applied cut to select outgoing nitrogen isotopes only.

### 4.3 Exclude Scattered Neutron Hits in LAND

During the analysis it turned out that, when requiring incoming  $^{20}\text{N}$ , many  $^{20}\text{N}$  isotopes detected at the TFW were in coincidence with a hit in the LAND detector which cannot be caused by real neutron events. Therefore, several tests were applied to check the origin of these neutrons. The assumption was that these  $^{20}\text{N}$  isotopes did not undergo a reaction in the reaction target, but impinged onto the TFW inducing a reaction while the products scattered into the LAND.

As the scattered particles make a detour, they should occur later in time at LAND apparently with a lower velocity. In order to check this, the fragment mass was plotted against the neutron velocity (figure 27a). This clearly showed that the events at LAND in coincidence with  $^{20}\text{N}$  isotopes detected at the TFW have a lower velocity which is consistent with the above assumption. Furthermore, one could see that this effect is almost negligible for the “true” reaction products (with masses lower than 20 u). In order to exclude most of the neutron-events stemming from reactions in the TFW, a cut on the neutron velocity  $v_n$  was applied accepting only events with  $v_n \geq 20$  cm/ns.



(a) Fragment mass number in relation to the neutron velocity to identify scattered neutrons. All events with a neutron velocity lower than 20 cm/ns were excluded (indicated by red line).

(b) Comparison of the fragment mass spectra with excluding scattered neutron hits by the cut on the neutron velocity (red line) and without (dark blue line).

Figure 27: Exclusion of scattered neutron hits. Here,  $^{20}\text{N}$  impinge onto a Pb target, requiring a hit in LAND, accepting only outgoing heavy fragments of charge number  $Z=7$ .

## 4.4 Empirical Identification of the Outgoing Fragment Masses

In order to understand the mass identification of the outgoing heavy fragment and to have a cross check to the tracker results (described below in section 4.5) an empirical identification was performed.

As the mass identification is done by measuring the magnetic rigidity of the charged particles in the magnetic field of ALADIN and measuring the resulting dispersion at the two GFIs, it can be described by the following equation (compare eq. 16):

$$B\rho = \text{const} \frac{A}{Z} \beta \gamma , \quad (29)$$

$$\text{with const} = \frac{uc}{e} ,$$

with  $B$ , the magnetic field strength,  $\rho$ , the radius of the deflected particle track,  $A$ , the mass number of the outgoing fragment, and  $Z$ , the charge number of the outgoing fragment. As  $B$  is rather constant in time over the entire experiment and  $Z$  is fixed by energy loss measurements at the TFW (see section 4.2) the deflection radius only depends on the mass number  $A$  and the velocity of the fragment. Beside that, also the initial starting point of the particle, i.e. the hit position on the target ( $x_{\text{target}}$ ), has to be taken into account. Furthermore, the outgoing particles can be deflected in the target causing an angular distribution which also influences the hit position on the GFIs and thus the mass identification.

Therefore, the difference in the hit position of the two GFIs in x-direction ( $x_{\text{GFI2}} - x_{\text{GFI1}}$ ) was investigated in correlation of the hit position at the second GFI ( $x_{\text{GFI2}}$ ), the hit position on the target in x-direction ( $x_{\text{target}}$ ), and the time-of-flight of the fragment ( $\Delta t_{\text{fragment}}$ ) (figures 28, 29, 30).

The minimization procedure will be described exemplarily for the angular distribution of the outgoing fragments, but is in principle the same for the hit position on the target and the velocity of the fragments. In the following, only incoming  $^{20}\text{N}$  impinging onto a Pb target and outgoing particles with  $Z=7$  were considered (via the energy loss in the TFW, section 4.2). A reaction trigger pattern was applied, requesting only fragments when a hit in LAND was registered.

Due to the different deflection in the magnetic field of ALADIN, the masses of the outgoing fragments can be identified by the x-position measurements in the two GFI detectors. Then, the angular distribution is given by

$$\tan \rho = \frac{x_{\text{GFI2}} - x_{\text{GFI1}}}{\Delta z} . \quad (30)$$

As the distance (in z-dimension) of the two GFIs is large in comparison to  $x_{\text{GFI2}} - x_{\text{GFI1}}$ , the argument of the tangent becomes very small. Thus, the Taylor series expansion can be truncated after first order and the difference in the x-position measurements of the two GFIs is a good measure of the deflection angle:

$$\rho = x_{\text{GFI2}} - x_{\text{GFI1}} . \quad (31)$$

This can be used to identify the masses of the outgoing fragments.

Figure 28b shows the angular distribution of the outgoing fragments versus the measured x-position on the second GFI ( $x_{\text{GFI2}}$ ). The diagonal lines represent the distributions of the outgoing fragments. The lowest diagonal line represents the non-reacted  $^{20}\text{N}$  beam



and the above lying lines represent outgoing fragments with decreasing mass number. There is a strong dependence of the angular distribution on the measured x-position at the second GFI. In order to improve the mass resolution derived by this method, a linear fit was applied for correction:

$$(x_{\text{GFI2}} - x_{\text{GFI1}})_{\text{corrected}} = (x_{\text{GFI2}} - x_{\text{GFI1}})_{\text{raw}} - x_{\text{GFI2}} \cdot a_1 . \quad (32)$$

With replacing  $(x_{\text{GFI2}} - x_{\text{GFI1}}) = \Delta x_{\text{GFI}}$ , the equation reads

$$\Delta x_{\text{GFI,corrected}} = \Delta x_{\text{GFI,raw}} - x_{\text{GFI2}} \cdot a_1 . \quad (33)$$

Only the slope ( $a_1$ ) is necessary and the offset can be omitted (will be included later on during the transformation from GFI-position to mass numbers). The slope was varied systematically while the resolution of the corrected peak was analyzed with a Gaussian fit. The minimization of the standard deviation of the Gaussian fit provided the optimum parameter of the slope to be applied for the identification of the masses of the outgoing fragments.

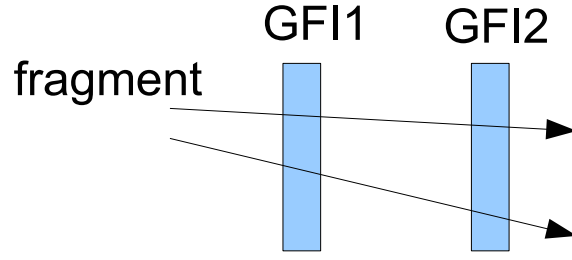
This procedure was also applied for the hit position on the target ( $x_{\text{target}}$ ) (visualized in figure 29) and the time-of-flight of the fragment ( $\Delta t_{\text{fragment}}$ ) (visualized in figure 30) representing the velocity of the fragment. The latter correction does not work as well as the others. There is still a significant slope for the  $^{20}\text{N}$ . The reason is not clearly identified. As the resulting mass peaks were well separated, this effect was not further investigated.

Afterwards, the corrected values ( $\Delta x_{\text{GFI,corrected}}$ ) were transformed via a second order polynomial into the referring mass numbers.

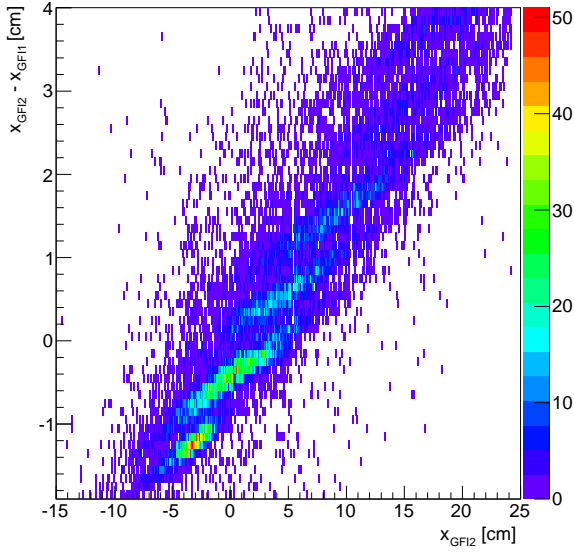
A summary of the results especially the resolution derived by this method is presented in table 5. A comparison to the results derived by the generic tracker will be given in section 4.6 (compare table 8).

Nucleus	Mass [u]	Mass Variance [u]	Mass Resolution [%]	Literature [40]
$^{20}\text{N}$	19.99	0.270	1.35	20.023
$^{19}\text{N}$	18.93	0.206	1.09	19.017
$^{18}\text{N}$	17.93	0.186	1.04	18.014

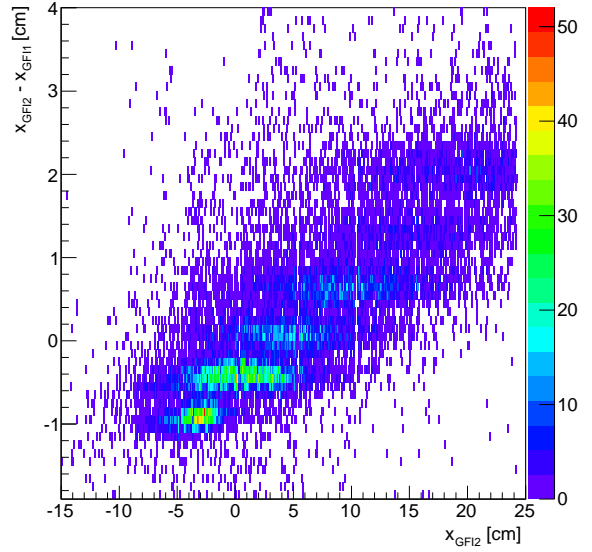
Table 5: Masses and mass resolution derived by the empirical calibration. A Gaussian fit was applied to extract the mean and the sigma. Here, incoming  $^{20}\text{N}$  impinge onto a Pb target, the charge of the heavy fragment is  $Z=7$ , requiring a hit in LAND and accepting only events with a neutron velocity  $v_n > 20 \text{ cm/ns}$ .



(a) Illustration of the influence of the fragment angle on the hit position at the GFIs for mass identification.

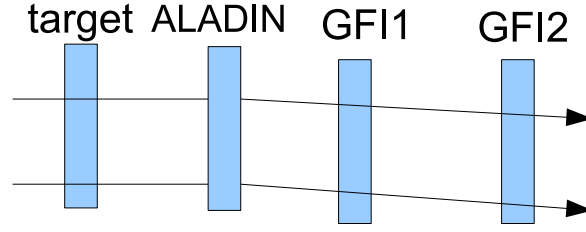


(b)  $\Delta x_{\text{GFI}}$  versus  $x_{\text{GFI2}}$  before correction.

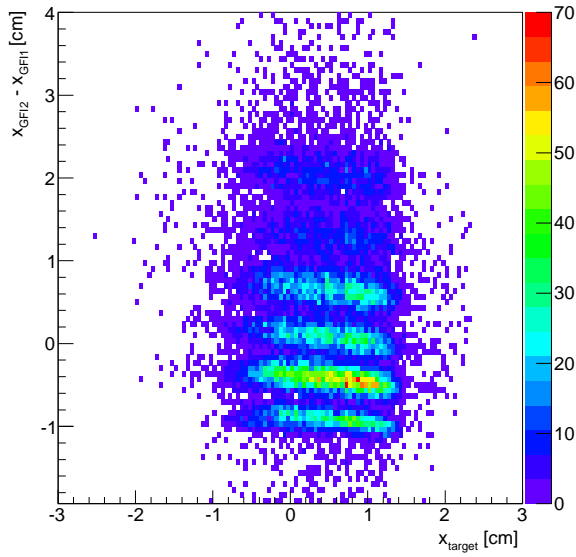


(c)  $\Delta x_{\text{GFI}}$  versus  $x_{\text{GFI2}}$  after correction.

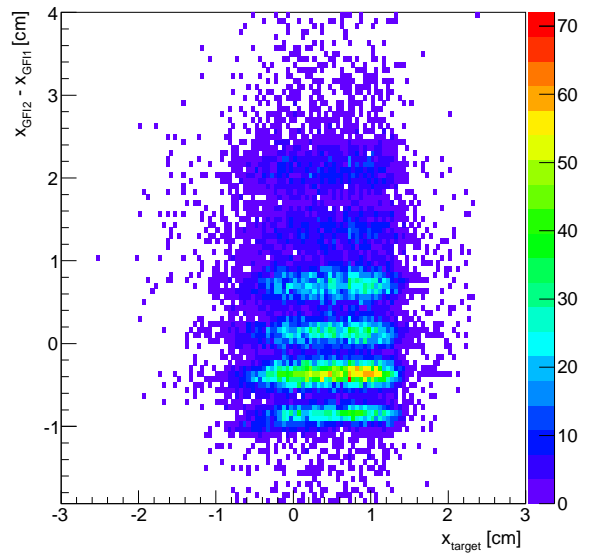
Figure 28: Procedure to correct for influences of the the fragment angle on the hit position at the GFIs for mass identification.



(a) Illustration of the influence of the hit position on the target ( $x_{\text{target}}$ ) on the hit position at the GFIs for mass identification.

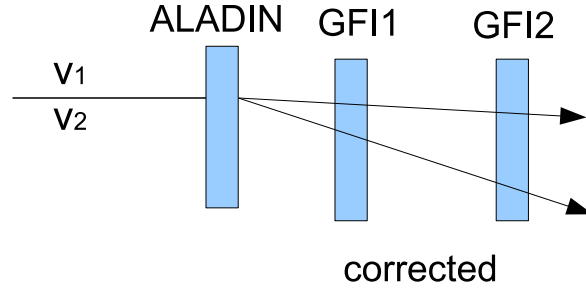


(b)  $\Delta x_{\text{GFI}}$  versus the hit position on the target ( $x_{\text{target}}$ ), before correction.

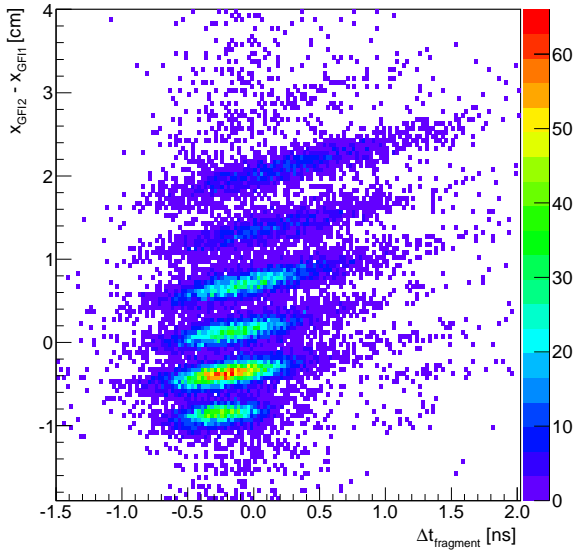


(c)  $\Delta x_{\text{GFI}}$  versus the hit position on the target ( $x_{\text{target}}$ ), after correction.

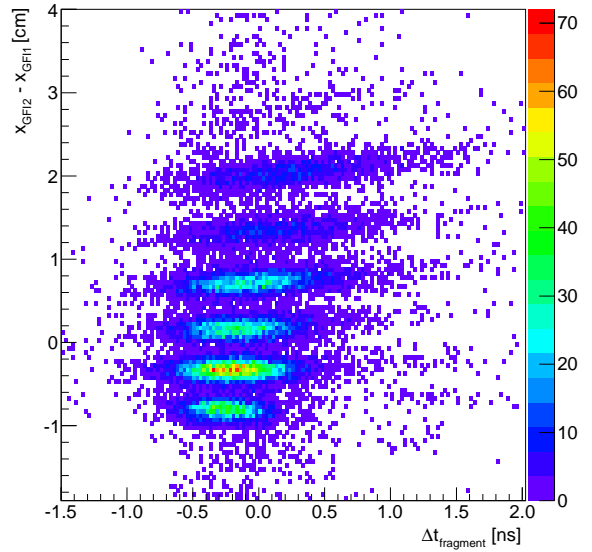
Figure 29: Procedure to correct for influences of the hit position of the impinging  $^{20}\text{N}$  at the target ( $x_{\text{target}}$ ) on the hit position at the GFIs for mass identification.



(a) Illustration of the influence of the time-of-flight of the heavy outgoing reaction fragment ( $\Delta t_{\text{fragment}}$ ) on the hit position at the GFIs for mass identification.



(b)  $\Delta x_{\text{GFI}}$  versus the time-of-flight of the heavy outgoing reaction fragment ( $\Delta t_{\text{fragment}}$ ), before correction.



(c)  $\Delta x_{\text{GFI}}$  versus the time-of-flight of the heavy outgoing reaction fragment ( $\Delta t_{\text{fragment}}$ ), after correction.

Figure 30: Procedure to correct for influences of the time-of-flight of the outgoing  $^{19}\text{N}$  nucleus ( $\Delta t_{\text{fragment}}$ ) on the hit position at the GFIs for mass identification.

## 4.5 Outgoing Particle Identification by the Generic Tracker

The generic tracker, developed by Ralf Plag<sup>1</sup>, is a standalone program (outside the land02 framework) which simulates the track of a charged particle through the entire LAND/R3B setup. Thereby, it takes energy loss in matter (in the different detectors, in the helium atmosphere of ALADIN, air of the fragment branch) into account and calculates the track of the particle, consisting of its position and directions along the x-, y- and z-axis, and time information at each detector. By that, the masses, velocities and angles of the particle track are derived. From the calculated path, the tracker can determine the residuals, meaning the deviation of the measured hit position in each detector to the calculated position where the particle should have hit the detector. In order to make the tracker work properly, it needed to be configured, especially the positions of each tracking detector had to be calibrated precisely, which will be described in section 4.5.1. The tracker can work in two different modes:

**forward tracking:** the particle track is fixed by the incoming beam detectors meaning the first two DSSSDs in front of the target. The hit position of the particle in these detectors fix the track and the tracker routine calculates the path through the whole setup.

**backward tracking:** the particle track is fixed by the outgoing beam detectors behind ALADIN, meaning the GFIs in the heavy fragment branch. The hit position of the outgoing reaction fragments in the two GFIs fix the track and the tracker routine calculates the particle track backwards through the setup. Here, as the GFIs only provide x-positions, the TFW is included for rough y-position measurement of the fragment.

**mixed tracking** is a combination of the forward and backward tracking mode.

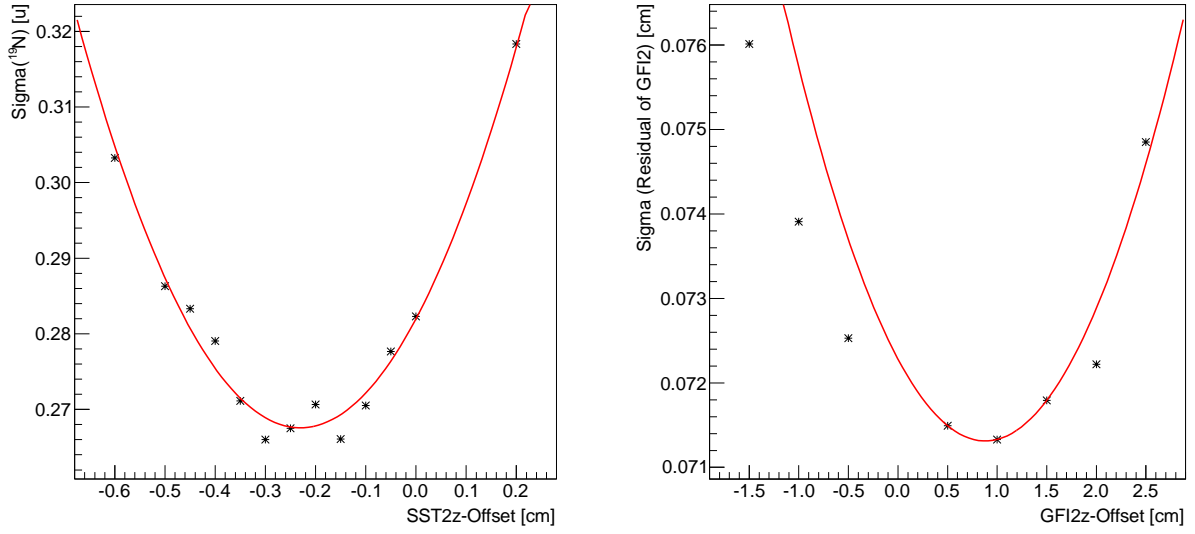
### 4.5.1 Calibration of the Detector Positions

In order to adjust the tracker deriving the correct masses with a good mass resolution and the proper momenta of the ejectiles, the position of the tracking detectors needed to be determined rather precisely. Also the time offsets of the detectors had to be determined, which had an influence on the velocity and, thus, on the momentum and mass distribution.

The tracker had to be supplied with precise positions for two groups of detectors: the DSSSDs for the incoming particle tracking and the GFIs for the outgoing reaction fragment. Rough values were provided at the homepage<sup>1</sup> of the tracker (provided by Paloma Diaz-Fernandez) and served as initial parameters for the following calibration procedure. The x-position of each detector was rather simple to estimate: as the tracker gave the residuals (meaning the deviation of the measured hit position of a particle in one detector relative to the theoretical hit position derived by the tracker), this offset simply had to be added in the configuration file. A more complicated task was, to find the correct z-positions of the detectors. This was not given by the tracker directly but had to be estimated with the shape and width of the x-residuals of the detectors and the positions and widths of the peaks of the mass distribution. Therefore, the first step was a systematic search for the best DSSSD position in z-direction. Afterwards, finding the best z-position of the GFIs and search of the z-position and proper time offset of the fragment ToF wall were additional tasks.

During these configurations, beside the cuts mentioned in the previous sections, the

<sup>1</sup> a documentation of the tracker can be found at <http://ralfplag.de/tracker/>



(a) Width of the outgoing  $^{19}\text{N}$  mass distribution derived by the tracker as a function of the z-position of the second DSSSD (called SST2z offset). The red line represents a 2<sup>nd</sup> order polynomial regression. The minimal mass resolution is found at a DSSSD offset of -0.23 cm.

(b) Width of the residual of the second GFI detector versus its offset for determination of the optimum GFI position. In the 2<sup>nd</sup> order polynomial regression (red line), only the GFI2zOffset=[0.5,1,1.5] were included, as only these provided rather symmetric residuals. The minimum is located at an offset of -0.88 cm.

Figure 31: Determining the best offsets of the DSSSDs and the GFIs for deriving best mass resolutions with the tracker.

following cuts were applied within the experiment specific configuration file: trigger pattern  $\text{TPat} \leq 255$ , taking only in-spill data and no cosmic events; both GFIs shall only have one event within the active area of  $x \in [-25\text{cm}, 25\text{cm}]$ ; both DSSSDs shall only have one hit.

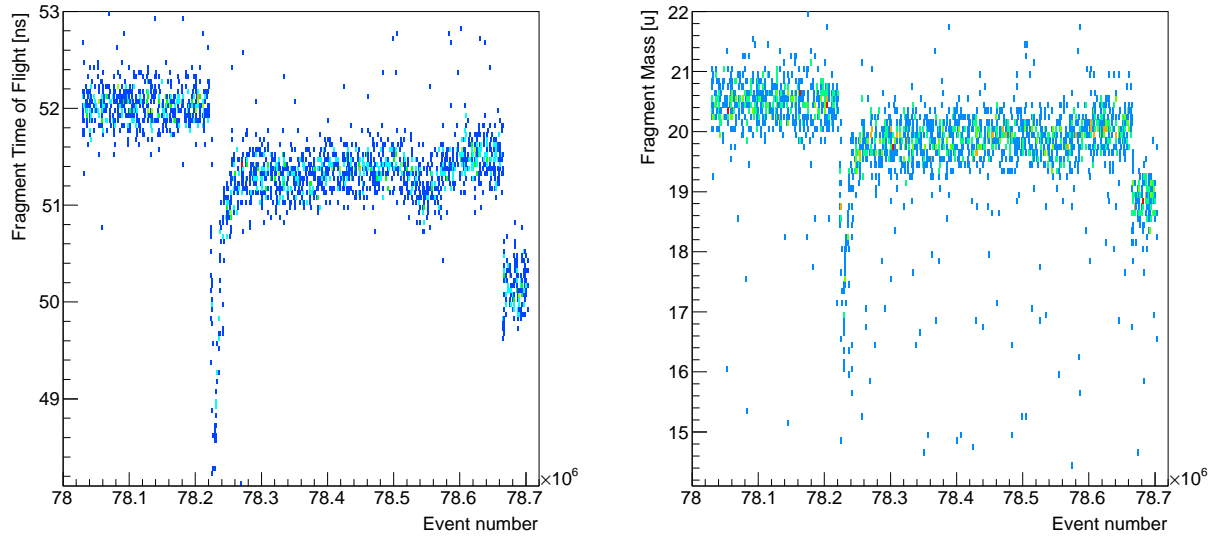
### Search for z-position of DSSSDs

In order to find the optimal DSSSD positions, the z-position of the second DSSSD was varied systematically, while keeping the positions of other detectors untouched. This was done, using the tracker in the forward tracking mode. Here, the particle track was fixed by the DSSSDs and thus their position translate into the mass resolution derived by the tracker. As the time-of-flight of the fragment had to be calibrated later, it was ignored during the first steps of the calibration procedure, applying the velocity of the incoming particle to the outgoing heavy fragment<sup>2</sup>. The residuals and mass resolution of the  $^{19}\text{N}$  were analyzed and plotted against the z-position (compare fig. 31a). A 2<sup>nd</sup> order polynomial regression was applied to find the z-position with the minimum mass resolution. The resulting value was committed to the referring tracker calibration parameter.

### Search for z-position of GFIs

In order to find the best position of the GFI detectors, the similar procedure as described for the DSSSDs was applied. The second GFI detector was moved in z-direction while

<sup>2</sup> with the tracker option `--ignore-tof`



(a) ToF between the POS and the fragment wall (TFW) versus the event number (running number increasing by one for each registered event) depicting jumps in the ToF at the TFW.

(b) Mass Number derived by the tracker versus the event number for the same file, showing how the jumps in the ToF transfer to the mass identification.

Figure 32: Illustration of the jumps in the ToF between POS and TFW and the influence on the derived mass distribution. This file was omitted from further analysis.

the other detectors (first GFI and both DSSSDs) were kept untouched. Here, the tracker was operated in the backward tracking mode as this fixed the particle track to the hits in the GFIs. Again, the ToF of the fragment was ignored and replaced by the velocity of the incoming particle. But, with moving the second GFI further apart from the first one, the mass peaks derived by the tracker also move further apart from each other, meaning the mass difference from  $^{15}\text{N}$  to  $^{20}\text{N}$  is greater than  $5u$ . By observing the mass difference, the residuals of the GFIs became asymmetric which was a hint that the position calibration was ambiguous. Therefore, the residuals of the GFIs were required to be symmetric while interpolating with a  $2^{nd}$  order polynomial regression for determining the optimum GFI position (compare figure 31b). The values with symmetric GFI-residuals also provided small residuals at the DSSSDs and good mass resolutions for  $^{19}\text{N}$  which was an additional proof to take only these GFI offsets into account.

### Search for z-position and time offset of TFW

Changing the z-offset of the fragment ToF wall, the tracker calculated the proper time offset. If these parameters together were passed to the configuration parameters, there were no significant changes in the mass resolution derived by the tracker routine. Thus, the z-offset was chosen to fit to a time offset of 0 ns.

After doing this for one file, it turned out, that the time offset is not constant over all subsets of files, making a time offset correction for each file (even within one run) necessary. But in a small fraction of the data, even inside one file, jumps appeared in the ToF as function of the event number (compare figure 32a). This, of course, also had an influence, e.g. on the mass resolution derived by the tracker (depicted in figure 32b) and, thus, had to be treated properly. The origin of these jumps is thought to be caused by

wrong calibration parameters in the land02 calibration files (compare section 3.5.8). Thus, a rigorous solution for that problem would be to repeat the calibration procedures with the land02 subroutines and provide new calibration parameters. As the tracker already provides the proper time offsets, the following solution was chosen: Jumps between two files could be corrected easily via the time offset parameter in the tracker configuration. Data with jumps occurring within one file were omitted sacrificing 3% of the entire data (17% of the empty target data).

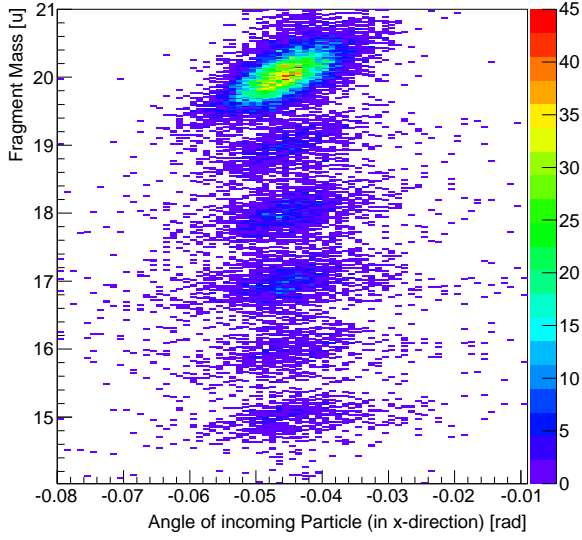
### 4.5.2 Checking the Calibration of the Tracker

In order to validate the calibration of the tracker, following verifications were performed.

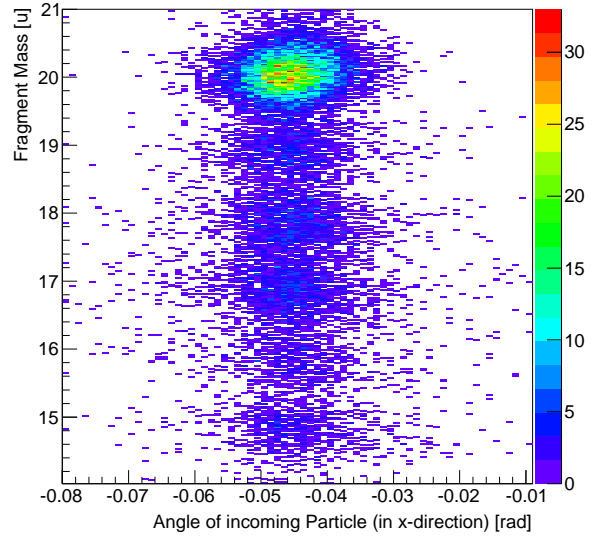
#### Mass Distribution in Correlation of the Angle of Incoming Particle

It might be possible that the DSSSDs and the GFIs cannot be moved independently from each other. Thus, the position calibration parameters of the tracking detectors found in the previous paragraph 4.5.1 might only characterize a local minimum but not a global one. Therefore, the outgoing mass distribution as a function of the incoming particle angle should give a flat relation for each tracking mode separately. In figure 33 the mass distribution is shown for each tracking mode (forward and backward) and for each direction (x- and y-direction) of the angle of the incoming particle (further called Indx and Indy). While the mass distribution seemed to be independent from Indx and Indy for backward tracking (compare figure 33b, 33d), this was not true for the forward tracking mode (figure 33a, 33c). This correlation turned out to be quite strong for Indx while it is almost negligible for Indy. Further attempts to move the GFIs further apart from the DSSSDs in the tracker calibration in order to minimize this effect did not succeed. A manual correction would be possible in order to improve the results of the mass distribution. But, as the mass peaks were already rather well separated, this task was not necessary.

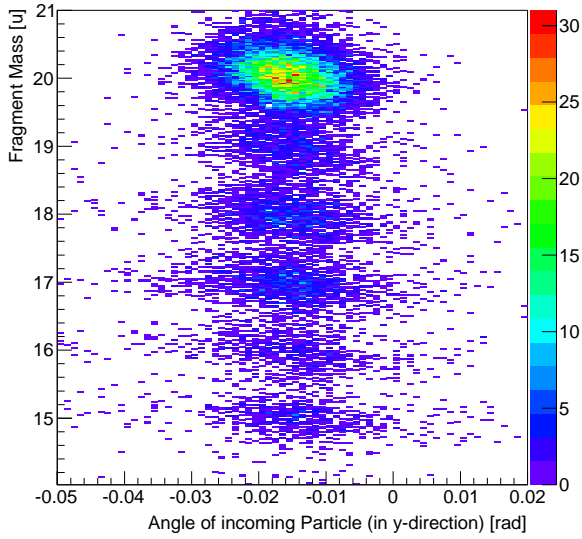




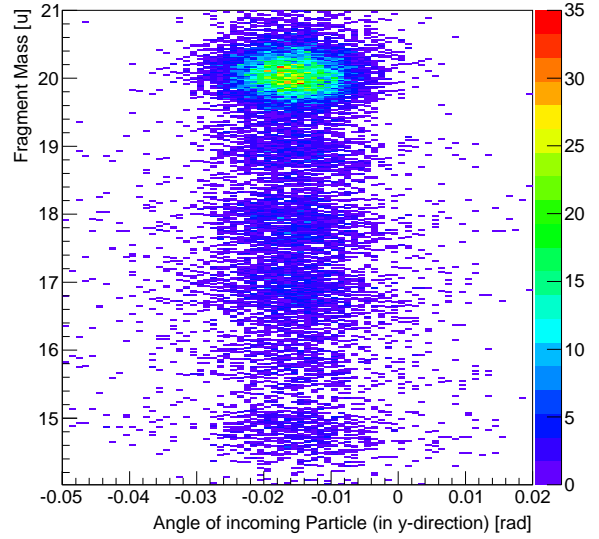
(a) Mass distribution in forward tracking mode as function of Indx.



(b) Mass distribution in backward tracking mode as function of Indx.



(c) Mass distribution in forward tracking mode as function of Indy.



(d) Mass distribution in backward tracking mode as function of Indy.

Figure 33: Correlation of the mass distribution (derived with the tracker) with the angle of the incoming particles in x- and y-direction (Indx and Indy) for the two main tracking modes. Here,  $^{20}\text{N}$  nuclides impinged onto a Pb target, requiring a hit in LAND, including the time-of-flight of the fragment, and applying a mixed-tracking.

### 4.5.3 Mass Distribution derived by the Tracker

A summary of the detector positions derived during the calibration procedure of the tracker is given in table 6. It has to be clarified that these positions do not necessarily reflect the physical positions of the detectors in the LAND/R3B cave. As mentioned in the previous paragraphs, these detector positions reflect a local minimum for the mass resolutions derived by the generic tracker. Furthermore, e.g. the TFW can be placed at any position as long as the time offset is adjusted accordingly.

Detector	x [cm]	y[cm]	z[cm]
PSP1	0.000	0.000	-88.900
Target	0.000	0.000	0.000
SST1	-0.011	-0.004	11.100
SST2	0.082	0.052	13.830
GFI1	-52.727	2.300	463.227
GFI2	-68.312	0.000	522.393
TFW	-224.328	1.301	1121.440

Table 6: Detector positions derived during the calibration of the tracker to find best mass resolutions. For further explanation, please, look at the text.

After applying the calibration parameters to the tracker, the mass resolution was surveyed again. The masses of the outgoing heavy reaction fragments were derived with the mixed tracking mode, including the ToF of the fragments, requiring a hit in LAND for  $^{20}\text{N}$  nuclei impinging onto a lead target. A Gaussian fit was applied in the interval  $A \in (18.6, 19.4)$  while the mean and the sigma are summarized in table 7. A plot of the mass distribution can be seen in figure 39. A comparison to the results derived by the empirical mass identification will be given in the next section (section 4.6, esp. table 8).

Nucleus	Mass [u]	Mass Variance [u]	Mass Resolution [%]	Literature [40]
$^{20}\text{N}$	20.06	0.246	1.23	20.023
$^{19}\text{N}$	18.95	0.236	1.24	19.017
$^{18}\text{N}$	17.93	0.258	1.44	18.014

Table 7: Masses and mass resolution derived by the tracker. A Gaussian fit was applied to extract the mean and the sigma. These data were obtained including the fragment ToF after including the corrections discussed in the previous paragraphs. Here, incoming  $^{20}\text{N}$  impinge onto a Pb target, the charge of the heavy fragment is  $Z=7$ , requiring a hit in LAND and accepting only events with a neutron velocity  $v_n > 20 \text{ cm/ns}$ .

## 4.6 Comparison of the two Methods for Mass Identification

Both methods (sections 4.4 and 4.5) for the identification of the outgoing fragment mass result in well separated mass peaks while the empirically derived mass spectra have a slightly higher resolution. The results are summarized in table 8. The slightly worse resolution of the results of the generic tracker might be manually corrected by a regression of the fragment mass as a function of the angle of the incoming particle in x-direction. However, as the generic tracker already provides well separated mass peaks, a further correction was not necessary.

Another cross check is possible by plotting the masses derived by the two methods in a two dimensional histogram (figure 34). Here, misalignments may give a hint on major problems between the two methods. The figure shows that most of the events are in the blobs along the diagonal line ranging from 15 u to 21 u indicating that no major misidentifications occurred. The small fractions of events that are explicitly apart from the well identified events are acceptable within statistical uncertainties. It is worth to mention that this plot cannot give a hint on which of the both methods is better or worse as misidentifications may originate from any of the methods. It is just to observe whether both methods lead to same results.

In conclusion, beside well separated mass peaks, the generic tracker provided the velocities, directions and angles of both incoming and outgoing reaction fragments without any additional conversion. Thus, the data of the generic tracker (section 4.5) were used for further analysis.

Nucleus	Empirical Identification Mass [u]	Generic Tracker Mass [u]	Literature [40] Mass [u]
$^{20}\text{N}$	$19.99 \pm 0.270$	$20.06 \pm 0.246$	20.023
$^{19}\text{N}$	$18.93 \pm 0.206$	$18.95 \pm 0.236$	19.017
$^{18}\text{N}$	$17.93 \pm 0.186$	$17.93 \pm 0.258$	18.014

Table 8: Comparison of the masses and mass resolution derived by both empirical mass identification and the generic tracker for incoming  $^{20}\text{N}$  impinging onto a Pb target, requiring one hit in LAND and a neutron velocity of  $v_n > 20$ .

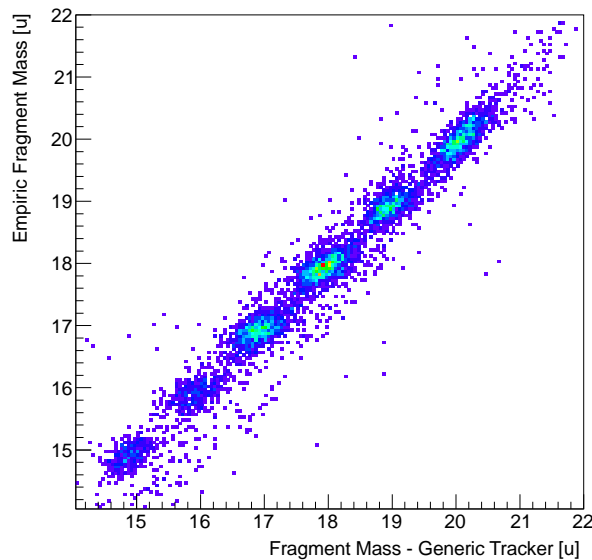


Figure 34: Comparison of the masses derived with the two different methods for incoming  $^{20}\text{N}$  impinging onto a Pb target, requiring one hit in LAND and a neutron velocity of  $v_n > 20$

## 4.7 LAND Efficiency Correction

With values between 70 and 90 %, the LAND efficiency is the most important efficiency to be corrected for. As the LAND efficiency varies with the kinetic energy of the neutrons, an energy dependent neutron efficiency correction was necessary. The total efficiency of LAND also depends on the acceptance of LAND and, thus, on the relative energy between the fragment and the neutron.

Therefore, the total efficiency of LAND in relation to the kinetic energy of the neutron in the system of the impinging nucleus was calculated (figure 35a). These calculations were based on simulations with the LAND Event Generator (LEG) where neutrons were emitted isotropically in the center of mass system. These data were provided by Dominic Rossi, for a detailed discussion, please, see [41]. The nominal neutron detection efficiency of LAND was determined in an earlier experiment [36] and build the basis of the LEG simulation. Furthermore, broken or deactivated paddles decreased the total efficiency of LAND and, therefore, were taken into account.

Beside that, the total efficiency depends on the acceptance of LAND. The acceptance defines how many neutrons hit the active area of LAND. It strongly depends on the angle under which the neutron is emitted. This depends on the kinetic energy of the neutron gained during the break up reaction and on the initial kinetic energy of the neutron delivered by the impinging particle.

The total one neutron detection efficiency of LAND (figure 35a) consists of the following parts. The first part up to an energy of roughly 4 MeV represents the one neutron detection efficiency of the active area of LAND with respect to deactivated paddles. It slightly increases with the kinetic energy of the neutrons as higher energetic neutrons are more efficiently converted into charged particles which subsequently are detected. After the cut-off at approximately 4 MeV, the total efficiency is governed by the acceptance of LAND. With increasing energy (stemming from the break-up reaction), more energy can be directed into transverse direction. In the worst case the neutron is emitted into 90

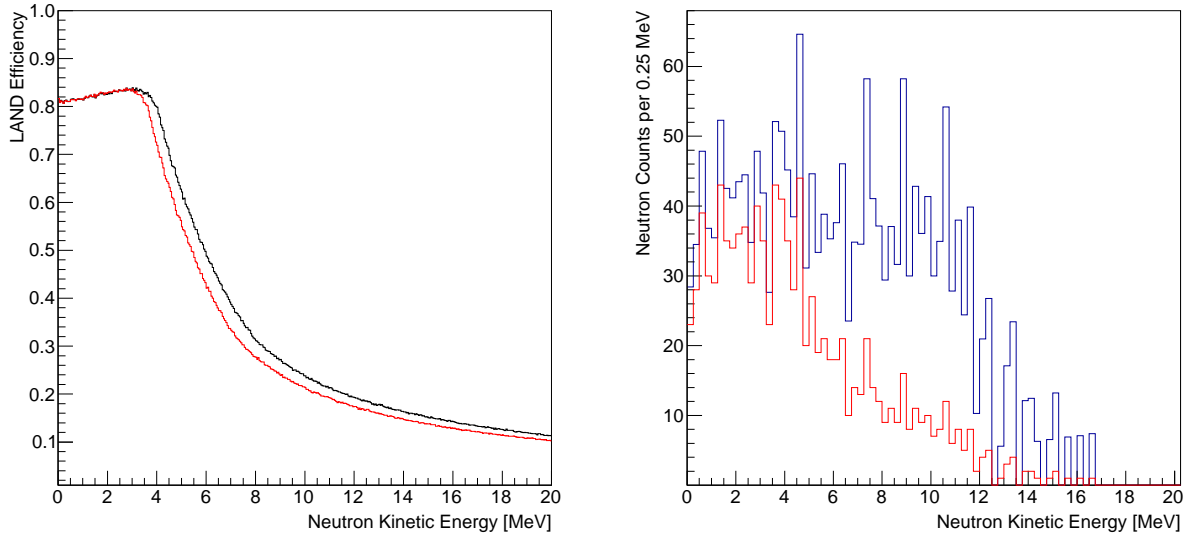
degree out of the beam axis in the rest frame (system of the impinging particle). Gaining more kinetic energy, the neutrons are more likely guided out of the active area of LAND. This leads to an exponential-like decay of the total efficiency.

The cut-off point is influenced by the initial kinetic energy of the neutron delivered by the impinging particle. The higher the energy of the impinging particle the stronger the neutrons are forward boosted making the cut-off occurring at higher energies. As the velocity of the  $^{20}\text{N}$  with  $v_{20\text{N}} = 0.742c$  was greater than  $v_{21\text{N}} = 0.726c$ , this effect can be seen comparing the cut-off points of the red and black line in figure 35a.

The kinetic energy of the neutron in the center of mass system was extracted from the measured data for each event based on the following equation

$$E_{\text{kin},n} = \gamma_{\text{Proj}}\gamma_n M_n - \gamma_{\text{Proj}}\beta_{\text{Proj}}\gamma_n\beta_n \cos(\angle[\text{Proj},n])M_n - M_n, \quad (34)$$

where the indices n and Proj stand for neutron and Projectile, respectively,  $\angle[\text{Proj},n]$  symbolizes the angle between the projectile and the neutron and  $M_n$  represents the rest mass (in MeV) of the neutron. Afterwards, this event was weighted with the proper efficiency value extracted from figure 35a during the calculation of the cross sections and the excitation energy spectra mentioned in section 4.9 and 4.10. The kinetic energy distributions measured (red line) and efficiency-corrected (blue line) are visualized in figure 35



(a) One-neutron detection efficiency of the LAND detector based on LEG-simulations by Dominic Rossi for impinging  $^{20}\text{N}$  (black line) and impinging  $^{21}\text{N}$  (red line).

(b) One-neutron emission spectrum of impinging  $^{20}\text{N}$  measured with LAND (red line) and corrected for the LAND efficiency (black line).

Figure 35: One-neutron detection efficiency and neutron emission spectrum of  $^{20}\text{N}$  impinging onto a Pb target as function of the kinetic energy of the neutrons in the center of mass system. The kinetic energy is given in the center of mass as indicated with equation 34.

## 4.8 Gamma Spectra

When a  $^{20}\text{N}$  nucleus interacts with the reaction target it dissociates into a neutron and a  $^{19}\text{N}$  nucleus for the specific reaction described here. The  $^{19}\text{N}$  can be left in an excited state, which deexcites by the emission of at least one gamma quant which should be detected in the NaI crystal ball (compare section 3.5.2). The energy of the gamma quant(s) gave an important contribution to the energy balance of the reaction and, thus, would be missing in the kinematics of the neutron-fragment-system, blurring the relative energy spectrum.

As the NaI crystal ball was highly segmented, it made a Doppler correction of the forward boosted gammas possible, but also an addback algorithm necessary. The gammas emitted from a moving source undergo a Doppler shift, dependent on the velocity of the emitting source, especially the incoming  $^{20}\text{N}$  nucleus, and the angle under which the gamma was emitted relative to the beam direction. The angle could be derived on the basis which crystal detected the gamma and the velocity of the  $^{20}\text{N}$  was determined by ToF measurements between the S8 and POS detectors (compare section 3.3) making a Doppler correction possible.

Beside that, a gamma quant hitting a single crystal could Compton scatter into a neighbouring crystal and release a part of its energy in the neighbouring crystal. Thus, a reconstruction of all the detector events belonging to one gamma interaction was necessary to derive the entire energy deposition of the gamma quant.

The addback algorithm applied here was provided by Valerii Panin [42]. The algorithm finds all crystals which had a detected energy above a certain threshold (chosen to be at  $E_{\gamma,\text{crystal}} > 0.3 \text{ MeV}$ ). Afterwards, these were sorted with decreasing energy. The crystal with the highest detected energy was set to be the center of a cluster, thus, center of the interaction of the primary photon (gamma quant). All neighbouring crystals (with an energy above the threshold) were added to give the cluster energy  $E_{\gamma}$ . Afterwards, a Doppler correction on the basis of the procedure described in the previous passage, was applied.

Basically, each crystal should have been provided with separate thresholds as the crystals in forward hemisphere would observe more Bremsstrahlung radiation than the one in backward hemisphere (ranging from 0.1 to 0.3 MeV). Here, a compromise was chosen with applying a constant threshold for all crystals of 0.3 MeV.

As the total emitted gamma energy is important for the calculation of the excitation energy (compare section 4.10), the energy of each gamma cluster identified during the reaction of one impinging  $^{20}\text{N}$  had to be summed up. But only if a single gamma cluster  $i$  had an energy of  $E_{\gamma,i} > 0.4$  it was defined to contribute to  $E_{\gamma,\text{sum}}$ :

$$E_{\gamma,\text{sum}} = \sum_{i=1}^n E_{\gamma,i} \quad \forall E_{\gamma,i} > 0.4 \text{ MeV}. \quad (35)$$

The gamma spectrum derived during the present analysis (figure 36) and a comparison to previous works by D. Sohler et al. [43] can be found in figure 37. The peak at 1.2 MeV is clearly visible in both spectra.

In order to estimate the background radiation,  $E_{\gamma,\text{sum}}$  of non-reacted  $^{20}\text{N}$  was utilized applying identical cuts as for  $^{19}\text{N}$  (red line figure 36). Only the mass cut was adopted accordingly. Figure 36 clearly indicates that the peak at 1.2 MeV originates from excited states of the  $^{19}\text{N}$  nucleus and not from background radiation and, thus, can be used to separate between transitions of the impinging  $^{20}\text{N}$  into the ground state of  $^{19}\text{N}$ , on the one hand, or into excited states, on the other hand.

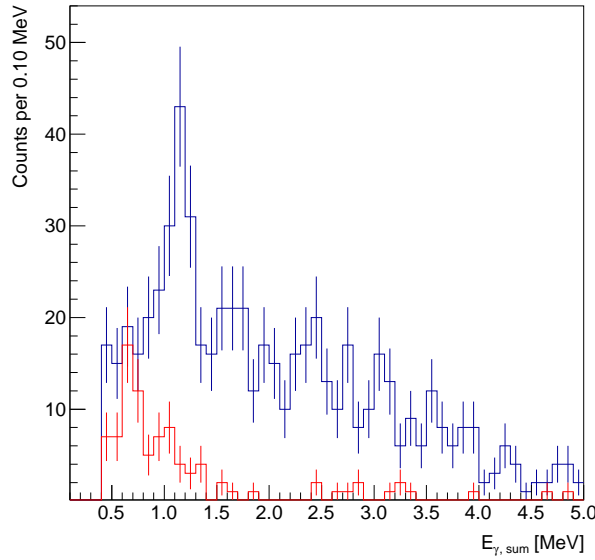


Figure 36: Gamma Sum Spectrum of outgoing  $^{19}\text{N}$  produced during reactions of  $^{20}\text{N}$  with the Pb target (blue line) and gamma background measured with unreacted  $^{20}\text{N}$  impinging on the Pb target (red line).

Due to the fact that the detection efficiency of the NaI Crystal Ball is between 70 and 85 % for energies of 1 to 5 MeV (see figure 38), the non-detection of a gamma quant is not equivalent to the case that there was no gamma quant emitted. This is important when separating transitions into the ground state of  $^{19}\text{N}$  from those to an excited state.

Using the straight condition: Ground state transitions are registered when no gamma was detected, would overestimate the contributions of the ground state and underestimate these of the excited states if no efficiency corrections would be applied. Therefore, contributions from excited states have been efficiency corrected. Afterwards, ground state contributions were obtained by subtracting the excited states from the total Coulomb dissociation cross section, which also includes events when no gamma was detected (further details are given in section 4.10).

The detection efficiency is shown in figure 38 (data provided by Paloma Díaz Fernández). These data were derived using the addback algorithm as described previously in the text and an addback threshold of 400 keV. Furthermore, a Doppler-correction of the gammas originating from particles with a velocity of  $\beta = 0.72$  was applied. Thus, a detection efficiency of 80 % ( $\pm 5$  %) was extracted for the first excited state of  $^{19}\text{N}$  at 1.15 MeV. A mean gamma energy of 2.0 MeV was estimated from figure 36 for the energy range between 0.4 to 5 MeV resulting in a mean detection efficiency of 85 % ( $\pm 8$  %).

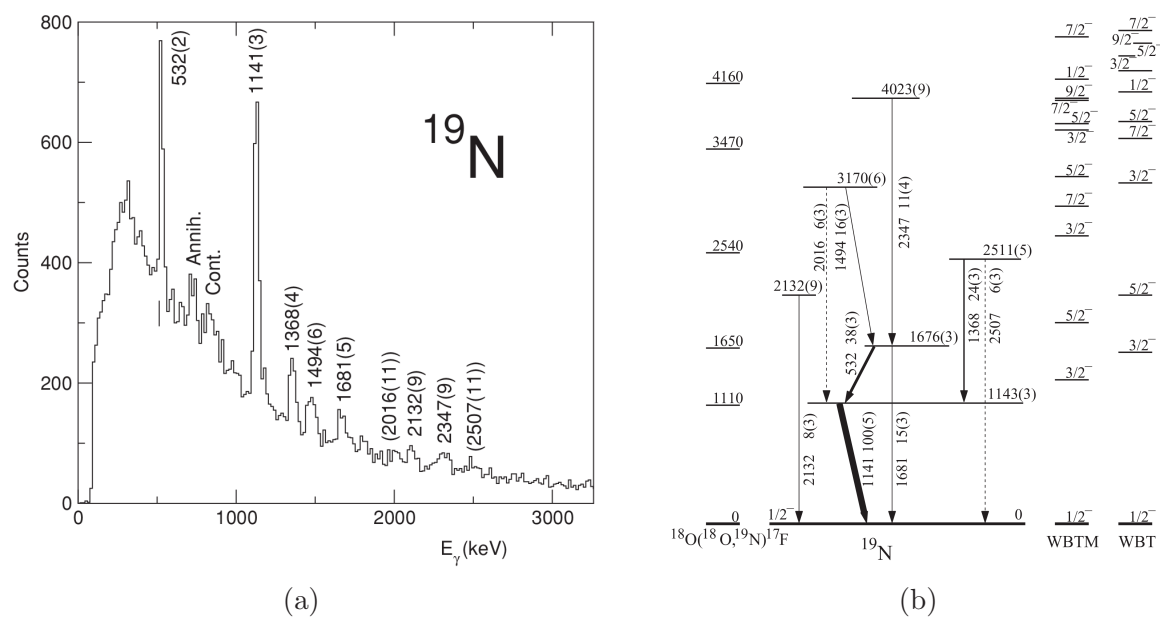


Figure 37: Gamma Spectra of  $^{19}\text{N}$  derived by D. Sohler et al. [43].

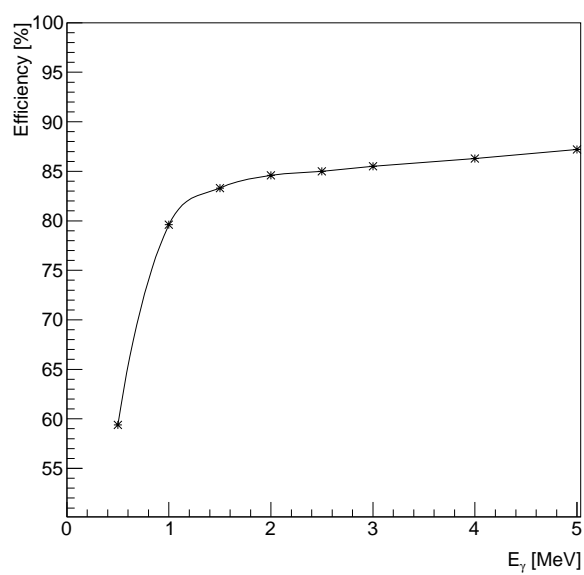


Figure 38: Detection efficiency of the Crystal Ball as a function of the energy of the high energetic photons.



## 4.9 Coulomb Dissociation Cross Section

The Coulomb dissociation cross section is given by the following formula [41]:

$$\sigma_{\text{CoulEx}} = p_{\text{Pb}} \cdot \frac{M_{\text{Pb}}}{d_{\text{Pb}} \cdot N_{\text{A}}} - p_{\text{C}} \cdot \alpha \cdot \frac{M_{\text{C}}}{d_{\text{C}} \cdot N_{\text{A}}} - p_{\text{empty}} \cdot \left( \frac{M_{\text{Pb}}}{d_{\text{Pb}} \cdot N_{\text{A}}} - \alpha \cdot \frac{M_{\text{C}}}{d_{\text{C}} \cdot N_{\text{A}}} \right) \quad (36)$$

Here,

- $p_{\text{Pb}}$  is the probability of the  $^{20}\text{N}$  to react with the lead (Pb) target,
- $M_{\text{Pb}}$  is the molar mass of lead,
- $d_{\text{Pb}}$  is the area density of the lead target,
- $N_{\text{A}}$  is the Avogadro's constant,
- $p_{\text{C}}$  is the probability of the  $^{20}\text{N}$  to react with the carbon (C) target,
- $M_{\text{C}}$  is the molar mass of carbon,
- $d_{\text{C}}$  is the area density of the carbon target,
- $\alpha$  is a scaling factor (detailed later),
- $p_{\text{empty}}$  is the probability of the  $^{20}\text{N}$  to react with no target but matter in the beam line.

It describes the breakup of a nucleus by only the Coulomb potential of the lead target while the beamline contributions (no target) and the nuclear contribution (carbon target) are subtracted. The background reactions of the matter in the beamline have to be subtracted on the probability level. Therefore, from probabilities to cross sections the background contributions need to be scaled with the number of atoms in the reaction targets [41]. A summary of the target properties and their type of contribution is given in table 3.

### 4.9.1 Data Normalization and Reaction Probabilities

In order to derive reaction probabilities, the outgoing fragment mass distribution needed to be normalized to the number of impinging particles. Basically, this can be done by counting the particles hitting the incoming beam detectors (see sections 3.3.2, 3.3.3) in figure 25. But this method would overestimate the number of impinging particles, as lots of losses occurred due to detector efficiencies, acceptances and applied cuts. Therefore, not the data of the incoming detector but the tracked data were used, as there are already a few cuts applied in the tracker configuration (compare section 4.5.1). Then, the integral over the whole outgoing fragment mass distribution (meaning all detected outgoing N-isotopes), requiring a hit in the TFW (via a Tpat&2), gave the number of impinging particles, that really traversed the entire setup without being scattered out of the beamline or being not detected due to detector inefficiencies. Not only the  $A=20$  nuclei but all outgoing N-isotopes had to be taken into account as all of them originate from an impinging  $^{20}\text{N}$  nucleus. Disregarding the  $A<20$  nuclei from the estimation of the number of incoming particles would underestimate the normalization factor by roughly 10 % and, therefore, overestimate the final Coulomb dissociation cross section by 10 %. Basically, this also holds true for the  $Z<7$  nuclei resulting from any reactions of the impinging  $^{20}\text{N}$ . But this number turned out to cause significantly smaller changes in the normalization factor and, thus, in the resulting cross section. The derived number had to be corrected with the proper downscale factor, which is used to prioritize certain physics events. Events when POS but not ROLU, the fragment wall and the neutron wall fired had a high priority and, thus, were always recorded if occurring (resulting in a downscale factor of 1). If

only the POS but not ROLU registered a hit, only every 64th event was recorded (thus, the downscale factor was 64). The downscaling was necessary to minimize the storage memory as the intense impinging (and unreacted) beam caused a large amount of rather useless data. Beside that, the small number of interesting reactions (caused by low cross sections involved) would be blocked by the large dead time caused by the intense impinging beam. The most important trigger patterns, the related detectors involved and the proper downscale factors are summarized in table 9.

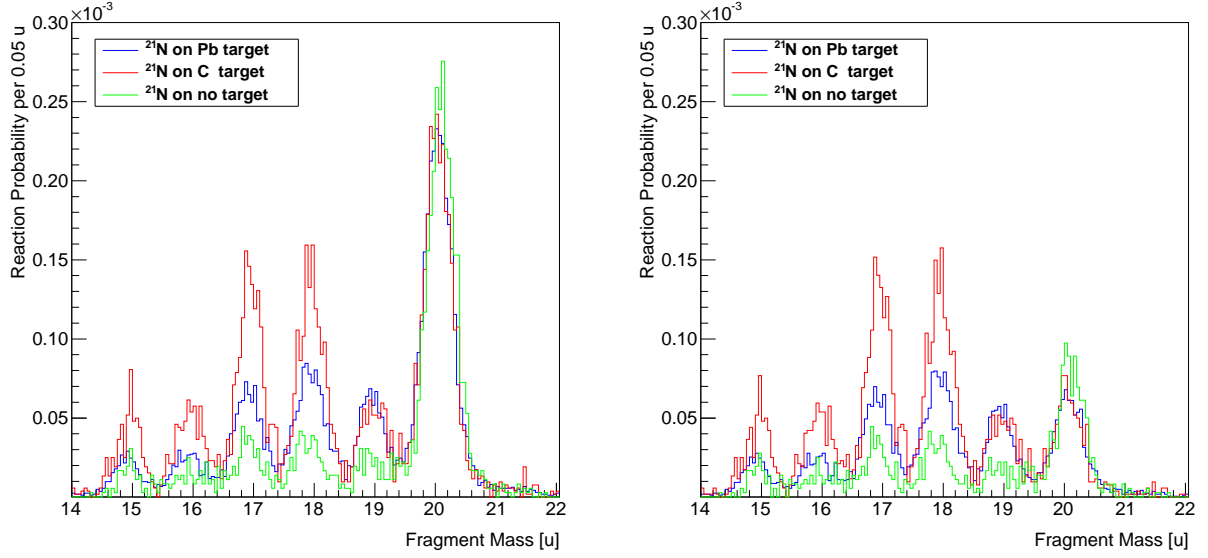
Trigger Pattern	Coincidence required	downscale factor
TPAT01=1	Good Beam = Spill on, POS!ROLU	64.0
TPAT02=2	GB+TFW = Spill on, POS!ROLU, TFW	16.0
TPAT03=4	FRS-S8 = Spill on, S8@FRS	32767.2
TPAT04=8	GB+CB-Sum = Spill on, POS!ROLU, TFW, CB-sum	1.0
TPAT05=16	GB+DTF = Spill on, POS!ROLU, TFW, DTF	1.0
TPAT08=128	GB+LAND = Spill on, POS!ROLU, TFW, LAND	1.0

Table 9: Most important Trigger Patterns used during the analysis described in this thesis with detectors fired and downscale factors.

The probabilities of the impinging  $^{20}\text{N}$  to react with each target ( $p_{\text{Pb}}$ ,  $p_{\text{C}}$ ,  $p_{\text{empty}}$ ) were extracted by plotting the outgoing fragment masses normalized with the number of incoming particles for each target separately (visualized in figure 39). Here, the generic tracker was run in the mixed tracking mode, including the fragment ToF. Also a single hit in LAND was required and the cut on the neutron velocity to exclude scattered neutrons was applied (39b). Beside that, in figure 39a, the reaction probabilities without a cut on the neutron velocity is shown to indicate the following scenario: As described earlier (compare section 4.3), the peak at  $A=20$  in the outgoing fragment mass spectrum is caused by  $^{20}\text{N}$  nuclei that did not react in the reaction target but elsewhere (most probably in the TFW, due to the higher areal density in comparison to air) causing neutrons scattered into LAND. Therefore, the reaction probabilities of each target (Pb, C, empty) should be equal at  $A=20$ . This is not the case for the reaction probability with the cut on the neutron velocity included as the cut goes directly through the velocity distribution (compare figure 27a). A small variation in the cut on the neutron velocity would already change the amount of resulting events significantly. Therefore, this plot indicates that this is no systematic problem of the analysis procedure of the  $^{20}\text{N}(\gamma, n)^{19}\text{N}$  reaction, especially in the data normalization, but only due to the cut on the neutron velocity which gives significant changes in the resulting events at  $A=20$ .

#### 4.9.2 Scaling Factor

As the Pb target holds the Coulomb and the nuclear contribution of the  $^{20}\text{N}(\gamma, n)^{19}\text{N}$  reaction (compare section 3.4) one has to subtract the nuclear contribution to get the pure Coulomb part of the reaction. As the nuclear part was measured with a carbon target and the carbon nuclei are much smaller than the Pb nuclei, the measured nuclear contribution of the carbon nuclei has to be scaled to the lead nuclei. Therefore, a scaling factor  $\alpha$  needs to be introduced which is mainly based on geometric reflections [41]. As the radius of a nucleus is proportional to the mass number  $A$  of a nucleus, the scaling factor can be derived by



(a) Reaction probability without cut on the neutron velocity

(b) reaction probability with cut on neutron velocity at 20 cm/ns.

Figure 39: Reaction probability distribution of incoming  $^{20}\text{N}$  impinging on different targets.

$$\alpha = \frac{A_{^{20}\text{N}}^{1/3} + A_{\text{Pb}}^{1/3}}{A_{^{20}\text{N}}^{1/3} + A_{\text{C}}^{1/3}} = 1.725 . \quad (37)$$

Beside that, also an experimental approach is possible. Therefore, one needs to observe a reaction channel of the  $^{20}\text{N}$  that has an excitation energy that can not be reached by Coulomb excitation anymore. During the analysis, it turned out that the  $^{20}\text{N}(\gamma, 3n)^{17}\text{N}$  reaction has a separation energy (3 neutron separation energy of  $^{20}\text{N}$ :  $S_{3n} = 10.32 \text{ MeV}$ ) too low for investigating the scaling factor. The 4 neutron removal could not be analyzed as the  $^{16}\text{N}$  were bent too much out of the beam axis, that the fragment tracking detectors (GFIs, compare 3.5.4) did not cover the entire beam spot anymore. Thus, the one-proton-removal reaction (with a one proton removal energy:  $S_{1p} = 17.94 \text{ MeV}$ ) needed to be utilized for that purpose. But the tracker needs different sets of calibration parameters to identify  $Z=6$  (meaning carbon) isotopes making the analysis of the one proton removal reaction a work-intensive task. As the  $^{20}\text{N}$  nucleus is not located too close to the neutron dripline, no deformation of the nucleus should occur and, thus, the geometric scaling factor should be similar to the experimentally derived one. For further analysis, the geometric scaling factor was used.

### 4.9.3 Error Estimation

The statistical errors were estimated via the following equation:

$$\begin{aligned}
 u^2(\sigma_{\text{CoulEx}})_{\text{stat}} &= \left( \frac{F_{\text{Pb}}}{N_{20\text{N,Pb}}} \right)^2 \cdot N_{19\text{N,Pb}} + \left( \alpha \cdot \frac{F_{\text{C}}}{N_{20\text{N,C}}} \right)^2 \cdot N_{19\text{N,C}} + \\
 &\quad \left( \frac{F_{\text{Pb}} - \alpha \cdot F_{\text{C}}}{N_{20\text{N,MT}}} \right)^2 \cdot N_{19\text{N,MT}} , \\
 \text{with: } F_{\text{Pb}} &= \frac{M_{\text{Pb}}}{d_{\text{Pb}} \cdot N_A} , \\
 F_{\text{C}} &= \frac{M_{\text{C}}}{d_{\text{C}} \cdot N_A} , \\
 u(\sigma_{\text{CoulEx}})_{\text{stat}} &= 7.8 \text{ mb} .
 \end{aligned} \tag{38}$$

The number of incoming and outgoing events to be included in this equation and the resulting contributions to the statistical uncertainties are summarized in table 10.

Systematic uncertainties were obtained by varying the cut on the incoming particle identification (namely Z and A/Z) within 3 sigma. The results are summarized in table 11. Additionally, the simulated LAND efficiency estimation has an uncertainty of 6 % and transfers directly into the Coulomb dissociation cross sections. Furthermore, the uncertainty of the Crystal Ball efficiency had to be taken into account. It amounted to 5 % for the photo peak efficiency and 8 % for the mean detection efficiency.

Target	acceptance window	in Z	in A/Z	#incoming	#outgoing	$u_{\text{stat}}$
Pb	$3\sigma$	[6.34 ; 7.44]	[2.82 ; 2.93]	1618992	1053	3.4 mb
C				520704	338	2.3 mb
empty				359344	101	6.6 mb
Pb	$1\sigma$	[6.71 ; 7.07]	[2.85 ; 2.89]	770608	522	5.1 mb
C				249568	149	3.1 mb
empty				176320	48	9.3 mb

Table 10: Number of incoming and outgoing events for the lead, carbon and empty target with respect to a 1 sigma and 3 sigma cut on the incoming particle properties (Z and A/Z). Furthermore, the contribution to the statistical uncertainty is given (last column). The total statistical uncertainty amounts to  $u_{\text{stat}}(3\sigma)=7.8 \text{ mb}$  and  $u_{\text{stat}}(1\sigma)=11.0 \text{ mb}$ .

### 4.9.4 Results of the Coulomb Dissociation Cross Section

In order to derive the final Coulomb excitation cross section, the probability distributions of the incoming  $^{20}\text{N}$  for each target were scaled with the proper scaling factor (compare paragraph 4.9.2). Furthermore, the target properties, especially the number of atoms in the target (e.g.  $\frac{M_{\text{Pb}}}{d_{\text{Pb}} \cdot N_A}$ ) had to be taken into account to take the step from reaction probabilities to cross section. The partial contributions of the different targets is depicted in figure 40a, while the histogram of the final Coulomb excitation cross section is illustrated in 40b (note the different scale and binning).

In order to estimate the Coulomb dissociation cross section of the  $^{20}\text{N}(\gamma, n)^{19}\text{N}$  reaction, the integral of the peak without any fit was extracted in the range of  $A \in [18.5; 19.5]$ .

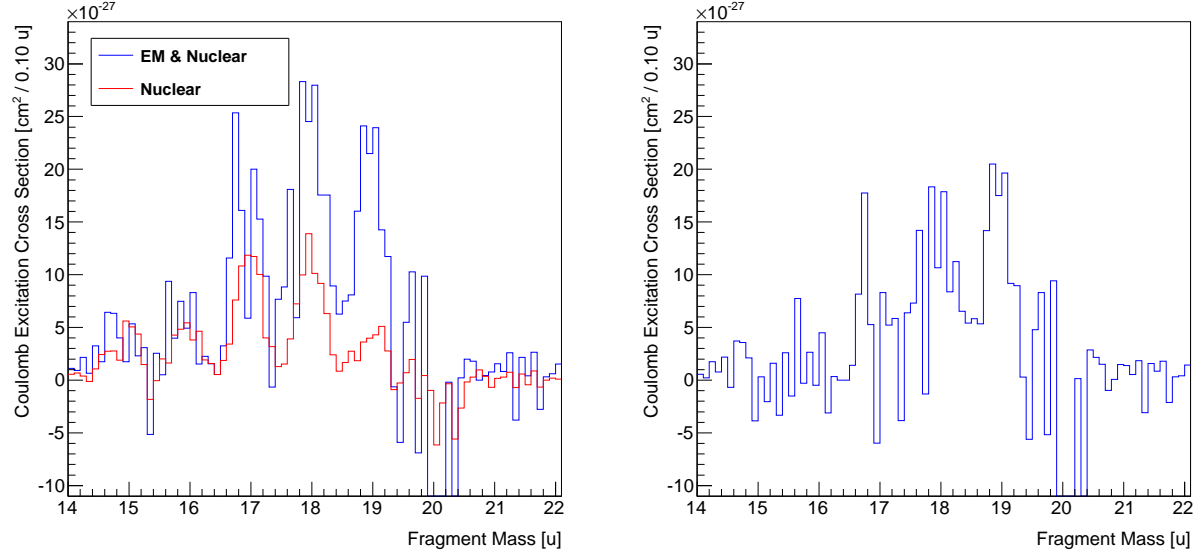
The statistical and systematic errors were estimated as described in the previous paragraph 4.9.3.

The results of the Coulomb excitation cross section and systematic uncertainties derived by sigma variations of the parameters of the incoming particle identification are summarized in table 11. Beside the here described method (first row), results from a different method, described in section 4.10, for transitions of  $^{20}\text{N}$  into the ground state and excited states of  $^{19}\text{N}$  are provided therein (last three rows). A discussion on the results will be given in section 4.11.

The Coulomb excitation cross section of the  $^{20}\text{N}(\gamma, n)^{19}\text{N}$  reaction amounts to  $\sigma_{\text{CoulEx}, ^{20}\text{N}} = (94.9 \pm 7.8^{\text{stat}} \pm 2.4_{\text{inPID}}^{\text{sys}} \pm 5.7_{\text{LANDefficiency}}^{\text{sys}}) \text{ mb}$ . As the total dissociation cross section was not corrected with the Crystal Ball efficiency, no uncertainties for the Crystal Ball efficiency contribute here.

acceptance window		3.0 $\sigma$	2.5 $\sigma$	2.0 $\sigma$	1.5 $\sigma$	1.0 $\sigma$	mean	standard deviation
Coul. Ex. (total)	[mb]	95.8	92.9	92.0	96.0	97.8	94.9	2.4
Coul. Ex. (all excited states)	[mb]	88.5	86.7	85.2	95.9	91.9	89.6	4.3
Coul. Ex. (ground state)	[mb]	7.3	6.2	6.9	0.1	5.8	5.3	2.9
Coul. Ex. ( $E_{\gamma, \text{sum}}=1141 \text{ keV}$ )	[mb]	33.5	31.5	30.3	31.2	31.0	31.5	1.2

Table 11: Coulomb excitation cross section in correlation with sigma variations on the incoming Z and A/Z-ratio for estimation of systematic uncertainties. The first row represents the results derived in section 4.9 which represents the total Coulomb dissociation cross section while the last three rows represent the results described in section 4.10: transitions into only excited states, the ground state, the first excited state (with  $E_{\gamma, \text{sum}}=1141 \text{ keV}$ ) of the outgoing  $^{19}\text{N}$ . For further description see section 4.10.



(a) Partial dissociation cross sections of  $^{20}\text{N}$  versus the mass number of the outgoing reaction fragment. The plot illustrates electromagnetic (EM) + Nuclear contribution as measured with the lead target (blue line) and the Nuclear contribution (as measured with the carbon target and scaled to the lead nuclei) after proper subtraction of the beamline contribution.

(b) Pure Coulomb excitation cross section of  $^{20}\text{N}$  derived by the subtraction of the histograms in (a).

Figure 40: Partial dissociation cross sections and Coulomb dissociation cross section of the  $^{20}\text{N}(\gamma, n)^{19}\text{N}$  reaction.

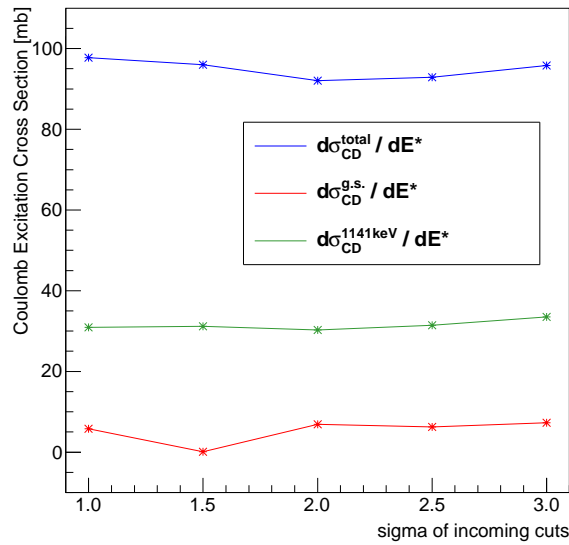


Figure 41: Coulomb excitation cross section in dependence of the sigma variation of the incoming Z and A/Z. Illustration of table 11.

## 4.10 Excitation Energy Spectrum

The excitation energy is calculated via

$$E^* = c^2 \sqrt{m_{\text{Frag}}^2 + m_n^2 + 2 \cdot \gamma_{\text{Frag}} \gamma_n m_{\text{Frag}} m_n (1 - \beta_{\text{Frag}} \beta_n \cos \theta_{\text{Frag},n})} - m_{\text{Proj}} c^2 + E_{\gamma, \text{sum}} , \quad (39)$$

where  $m_{\text{Frag}}$  is the rest mass of the outgoing heavy reaction fragment,  $m_n$  is the rest mass of the outgoing neutron,  $E_{\text{Frag}}$  is the kinetic energy of the outgoing heavy reaction fragment,  $E_n$  is the kinetic energy of the outgoing neutron,  $\beta_{\text{Frag}}$  is the velocity of the outgoing heavy reaction fragment,  $\beta_n$  is the velocity of the outgoing neutron,  $\gamma_{\text{Frag}} = (1 - \beta_{\text{Frag}}^2)^{-1/2}$ ,  $\gamma_n = (1 - \beta_n^2)^{-1/2}$ ,  $\theta_{\text{Frag},n}$  is the angle between the outgoing heavy reaction fragment and the neutron.  $E_{\gamma, \text{sum}}$  is the energy of all gamma quanta emitted during the reaction.

The mass of the incoming  $^{20}\text{N}$  and the outgoing  $^{19}\text{N}$  were extracted from G. Audi et al. (2003) [44]. Differences to the updated mass evaluation [40] amount to only 10 keV which cannot be resolved by the present LAND/R3B setup. The neutron mass was extracted from [45]. The other data were extracted from the measured data (velocity of the heavy fragment and the neutron, the angle between the fragment and the neutron, and  $E_{\gamma, \text{sum}}$ ). The  $E_{\gamma, \text{sum}}$  was calculated as described in section 4.8. Based on these derived gamma energies, a separation between ground state transitions and transitions into excited states was done.

For the calculation of the excitation energy spectrum the outgoing fragment mass number was required to be in the range of  $A_{\text{frag}} \in [18.5, 19.5]$ . Furthermore, the cuts described in section 4.9.1 and 4.5 were applied as well. If a gamma was detected, the gamma-sum energy (compare equation 35) was added as described in equation 39. If no gamma was detected at all, only the other properties of the referring event could be involved in the calculation of the excitation energy spectra. Anyway, each event, no matter whether a gamma was detected or not, contributed to the total (or inclusive) excitation energy spectrum and the total Coulomb dissociation cross section. The total excitation energy spectrum of the Coulomb dissociation of  $^{20}\text{N}$  is illustrated in figure 42.

The statistical uncertainty of each bin  $u_{\text{bin}}$  in the histograms were derived by calculating the square root of the sum of the squares of the weights,  $u_{\text{bin}} = \sqrt{\sum_{i=1}^n w_i^2}$  with  $w_i$  the weights of the bin entry  $i$  (see [46] for further explanation). As the weights of the entries are always one, these errors reflect the square root of the bin content of each bin.

Transitions into any excited state of  $^{19}\text{N}$  were defined to fulfill  $E_{\gamma, \text{sum}} > 0.4$  (figure 43) and corrected with the mean Crystal Ball detection efficiency of  $(85 \pm 8) \%$  (figure 54).

The excitation energy spectrum of  $^{20}\text{N}$  into the first excited state at 1141 keV (figure 45) was derived as follows. In the  $E_{\gamma, \text{sum}}$ -spectrum (figure 36), a Gaussian fit was applied in the range of 1.05 MeV and 1.30 MeV resulting in a mean of 1.15 MeV and a  $\sigma_{\text{Gauss}} = 0.15$  MeV. Afterwards, the excitation energy spectrum was calculated for all events which fulfill  $E_{\gamma, \text{sum}} \in [0.7; 1.6]$  (figure 45). These data were corrected with the Crystal Ball detection efficiency of  $(80 \pm 5) \%$  (referring to the energy of 1.15 MeV).

Transitions into the ground state of  $^{19}\text{N}$  were derived by subtracting the efficiency corrected spectrum of all excited states from the total spectrum (figure 44).

Thus, the total excitation energy spectrum was separated into three parts: First, transitions into any excited state (including the first excited state). Second, transitions into the first excited state and third, transitions into the ground state of  $^{19}\text{N}$ . Afterwards, each excitation energy spectrum was integrated to derive the cross sections of each part of the



Coulomb dissociation. Variations on the incoming particle identification were performed to derive uncertainties of the cross sections stemming from these cuts (compare table 11). The Coulomb dissociation cross sections for each part of the reactions with their specific uncertainties are given in table 12.

## 4.11 Discussion

From table 12 one perceives that 95 % of the Coulomb dissociating  $^{20}\text{N}$  nuclei pass into excited states of  $^{19}\text{N}$ . 33 % of the total Coulomb dissociation cross section are caused by transitions into the first excited state of  $^{19}\text{N}$  at 1141 keV. Transitions into the ground state of  $^{19}\text{N}$  during the Coulomb dissociation of  $^{20}\text{N}$  contribute to only 4 % which is consistent with zero within the uncertainties (especially visible in figure 44).

The total excitation energy spectrum of the Coulomb dissociation of  $^{20}\text{N}$  (figure 42b) shows no entries in the energy range between 0 and 2.0 MeV as expected. At 2.0 MeV there is a notable increase of the Coulomb dissociation cross section representing the one neutron separation threshold ( $S_{1n}$ ) of  $^{20}\text{N}$  at 2.16 MeV [40]. Afterwards, there is a bumpy structure visible between 2.0 and 12.0 MeV before decreasing to values which are compatible with zero within the uncertainties. A small enhancement arises at an energy of 16.5 MeV which cannot be explained entirely by the uncertainties. Behind 18.0 MeV the spectrum becomes zero as the amount of virtual photon with 18.0 MeV energy is only 15 % of the amount of virtual photons with an energy of 3.0 MeV.

The excitation energy spectrum for transitions of  $^{20}\text{N}$  into any excited state of  $^{19}\text{N}$  (figure 43) shows similar behavior as the total spectrum as it dominates the total spectrum. Figure 43 shows an increase of the cross section above zero at 3.0 MeV, slightly above the one neutron separation threshold observed in the total spectrum. Again, an irregular structure occurs at excitation energies between 3.0 and 14.0 MeV. Peaks are visible at 5.5 MeV and again at 16.5 MeV which cannot be explained entirely by uncertainties. At 18 MeV the spectrum drops to zero as the number of virtual photons decreased dramatically.

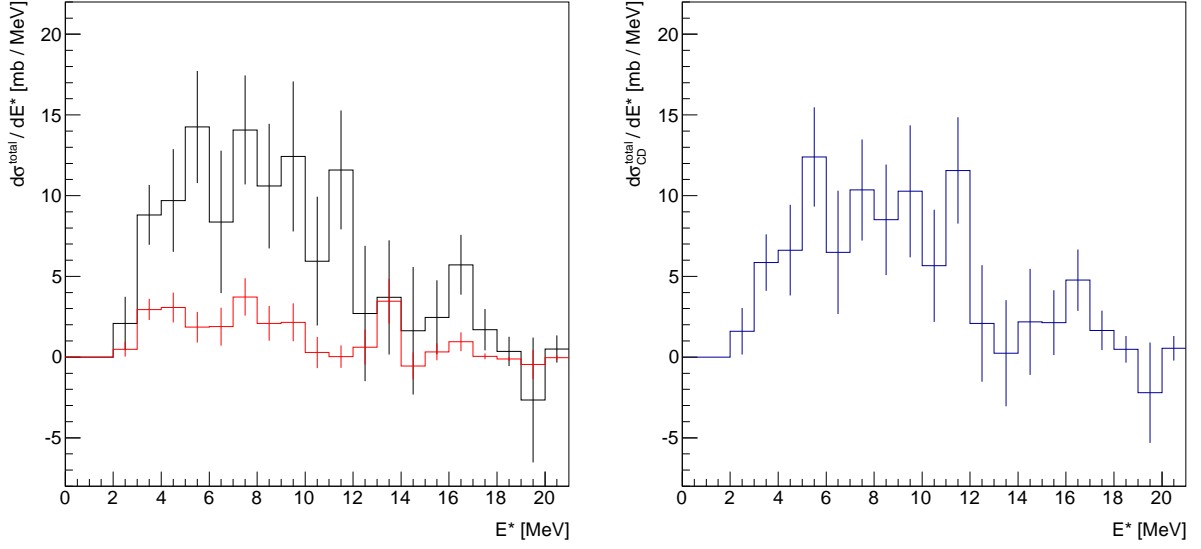
Transitions into the ground state of  $^{19}\text{N}$  (figure 44) amount to only 4 %. Within the statistical uncertainties this is consistent with zero. Thus, no further statement on these transitions is possible.

The excitation energy spectrum of transitions of  $^{20}\text{N}$  into the first excited state of  $^{19}\text{N}$  at 1141 keV are shown in figure 45. Again, the spectrum first arises above zero at 3.0 MeV slightly above the one neutron separation threshold. Furthermore, a structure is visible at energies between 3.0 and 14 MeV although only the peaking structure between 3.0 MeV and 6 MeV rise significantly above zero within the uncertainties.

CDCS (total)	(94.9	$\pm 7.7^{\text{stat}}$	$\pm 2.4^{\text{sys}}_{\text{inPID}}$	$\pm 4.9^{\text{sys}}_{\text{LAND}}$ )		mb
CDCS (all excited states)	(89.6	$\pm 7.5^{\text{stat}}$	$\pm 4.3^{\text{sys}}_{\text{inPID}}$	$\pm 5.4^{\text{sys}}_{\text{LAND}}$	$\pm 7.2^{\text{sys}}_{\text{CB}}$ )	mb
CDCS (ground state)	(5.3	$\pm 1.8^{\text{stat}}$	$\pm 2.9^{\text{sys}}_{\text{inPID}}$	$\pm 0.3^{\text{sys}}_{\text{LAND}}$	$\pm 0.4^{\text{sys}}_{\text{CB}}$ )	mb
CDCS ( $E_{\gamma,\text{sum}}=1141$ keV)	(31.5	$\pm 4.5^{\text{stat}}$	$\pm 1.2^{\text{sys}}_{\text{inPID}}$	$\pm 1.9^{\text{sys}}_{\text{LAND}}$	$\pm 1.6^{\text{sys}}_{\text{CB}}$ )	mb

Table 12: Summary of the Coulomb dissociation cross section (CDCS) of the  $^{20}\text{N}$  for a) the total reaction, b) transitions into any excited state of the outgoing  $^{19}\text{N}$ , c) transitions into the ground state of the outgoing  $^{19}\text{N}$ , d) transitions into the first excited state of the outgoing  $^{19}\text{N}$  with proper uncertainties.

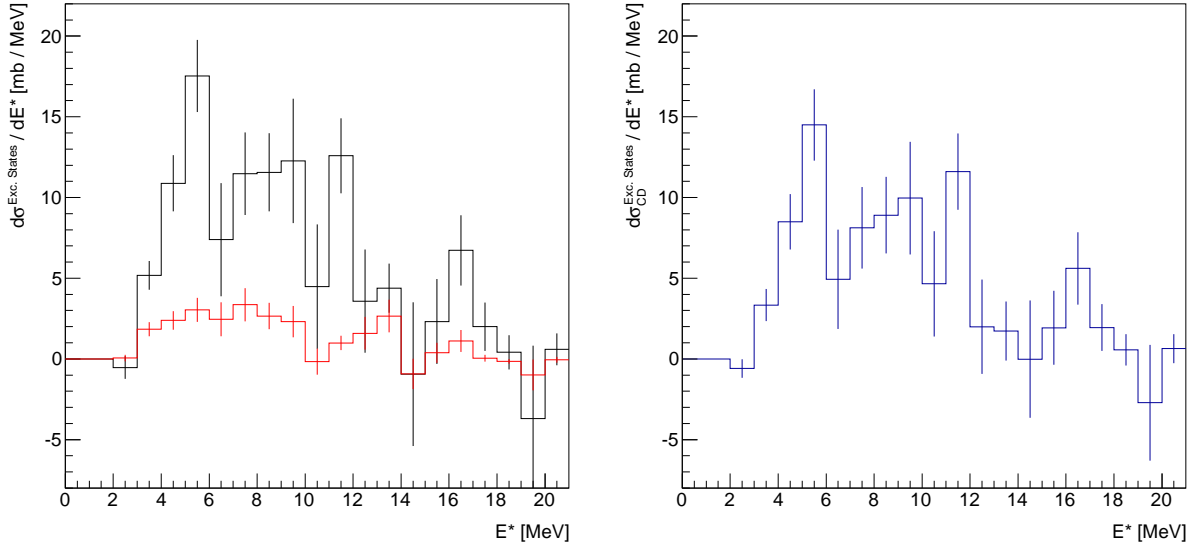




(a) Total excitation energy spectrum of  $^{20}\text{N}$  impinging onto the Pb target (black line) for visualization of the Coulomb+Nuclear contribution and onto the C target (red line) for visualizing the Nuclear contribution, each after subtraction of the beamline background.

(b) Final total Coulomb dissociation excitation energy spectrum (derived from the subtraction of the histograms to the left).

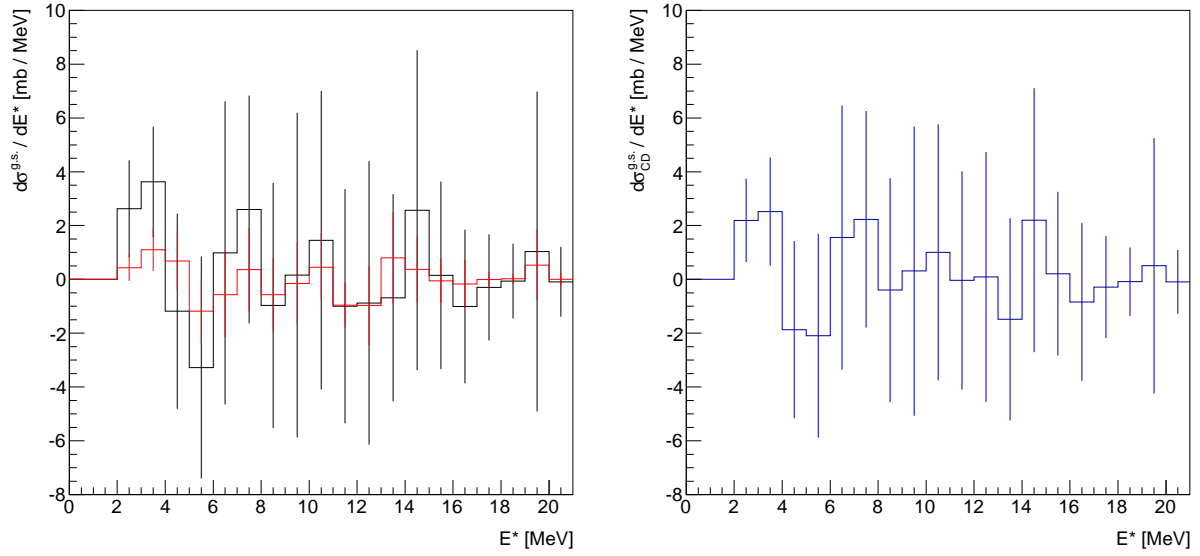
Figure 42: Excitation energy spectra for the total Coulomb dissociation of  $^{20}\text{N}$ .



(a) Excitation energy spectrum of  $^{20}\text{N}$  impinging onto the Pb target (black line) for visualization of the Coulomb+Nuclear contribution and onto the C target (red line) for visualizing the Nuclear contribution, each after subtraction of the beamline background.

(b) Coulomb dissociation excitation energy spectrum (derived from the subtraction of the histograms to the left).

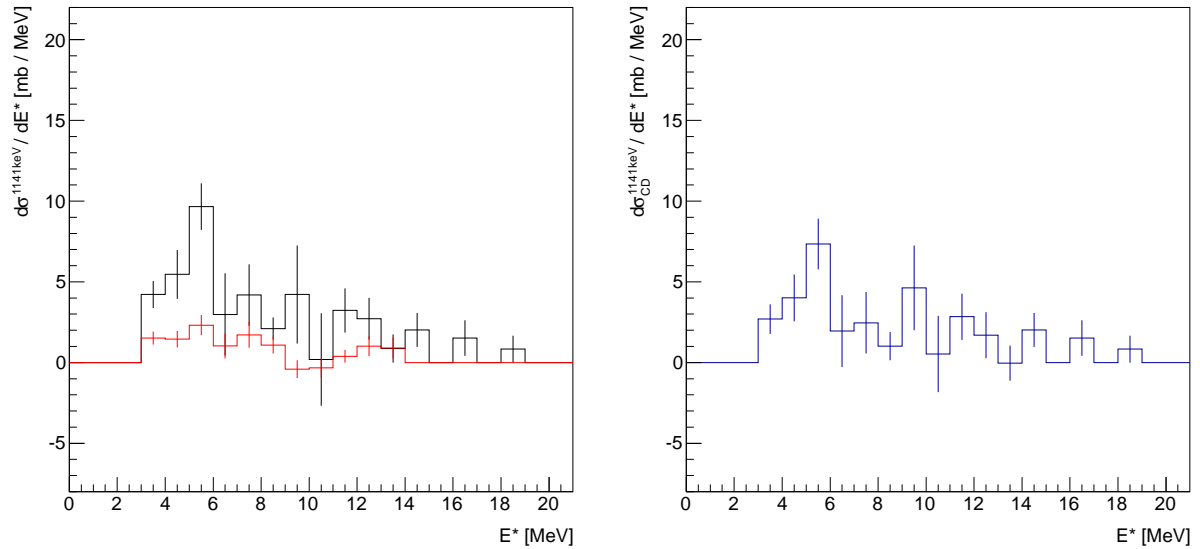
Figure 43: Excitation energy spectra for the Coulomb dissociation of  $^{20}\text{N}$  in any excited state.



(a) Excitation energy spectrum of  $^{20}\text{N}$  impinging onto the Pb target (black line) for visualization of the Coulomb+Nuclear contribution and onto the C target (red line) for visualizing the Nuclear contribution, each after subtraction of the beamline background.

(b) Final Coulomb dissociation excitation energy spectrum for only Ground State transitions (derived from the subtraction of the histograms to the left).

Figure 44: Excitation energy spectra for Ground State transitions of the  $^{20}\text{N}(\gamma, n)^{19}\text{N}$  reaction.



(a) Excitation energy spectrum of  $^{20}\text{N}$  impinging onto the Pb target (black line) for visualization of the Coulomb+Nuclear contribution and onto the C target (red line) for visualizing the Nuclear contribution, each after subtraction of the beamline background.

(b) Final Coulomb dissociation excitation energy spectrum for transitions into the first excited state of the  $^{19}\text{N}$  at 1141 keV (derived from the subtraction of the histograms to the left).

Figure 45: Excitation energy spectra for transitions into the first excited state of the  $^{19}\text{N}$  at 1141 keV of the  $^{20}\text{N}(\gamma, n)^{19}\text{N}$  reaction.

## 4.12 Photo Absorption and Neutron Capture Cross Section

From the previous measurements, especially the excitation energy spectra of the Coulomb dissociation, one can derive the astrophysically relevant neutron capture cross section.

First, the differential photo absorption cross section needs to be calculated via the virtual photon theorem which reads [47]

$$\frac{d\sigma_{CD}}{dE_\gamma} = \frac{1}{E_\gamma} n_{\text{E1}}(E_\gamma) \sigma_{\text{E1}}^{\text{photo}}, \quad (40)$$

Here,  $\frac{d\sigma_{CD}}{dE_\gamma}$  is the differential Coulomb dissociation cross section as a function of the excitation energy (where  $E_\gamma = E^*$ ) as calculated in the last section (section 4.10),  $n_{\text{E1}}(E_\gamma)$  is the number of virtual photons and  $\sigma_{\text{E1}}^{\text{photo}}$  is the photo absorption cross section for multipolarity E1 as a function of the excitation energy.

As the cross sections of higher multiplicities are found to be three orders of magnitude lower than for E1 [48], multiplicities higher than E1 can be neglected.

Then, the equation can be rewritten as

$$\frac{d\sigma_{CD}}{dE^*} = \frac{1}{E^*} n_{\text{E1}}(E^*) \sigma_{\text{E1}}^{\text{photo}}, \quad (41)$$

and the photo absorption cross section can be calculated via

$$\sigma_{\text{E1}}^{\text{photo}} \equiv \sigma_{\gamma, \text{n}} = \frac{d\sigma_{CD}}{dE^*} \frac{1}{n_{\text{E1}}(E^*)} E^*. \quad (42)$$

The virtual photon spectrum for the E1 multipolarity can be calculated as described in ref. [47] via

$$n_{\text{E1}}(E^*) = \frac{2}{\pi} Z_{\text{T}}^2 e^2 \alpha \left( \frac{c}{v} \right)^2 \left( \xi K_0(\xi) K_1(\xi) - \frac{v^2 \xi^2}{2c^2} [K_1^2(\xi) - K_0^2(\xi)] \right), \quad (43)$$

where  $K_i$  are the Bessel functions of the order  $i$ ,  $\alpha$  the fine-structure constant, and  $\xi$  the adiabaticity parameter which reads

$$\xi = \frac{E^* b}{\hbar \gamma \beta c}, \quad (44)$$

where  $b$  is the impact parameter.

The virtual photon spectrum of  $^{20}\text{N}$  impinging onto a lead target with an energy of 490 AMeV is depicted in figure 46.

Utilizing the fact that nuclear reactions are invariant under time reversal, the neutron capture cross section can be determined via the theorem of detailed balance [47]

$$\sigma_{\text{n}, \gamma} = \frac{2(2J_{\text{A}} + 1)}{(2J_{\text{B}} + 1)(2J_{\text{n}} + 1)} \frac{k_\gamma^2}{k_{\text{c.m.}}^2} \sigma_{\gamma, \text{n}}, \quad (45)$$

where  $\sigma_{\gamma, \text{n}}$  is the photo absorption cross section (compare eq. 42),  $k_\gamma = E^*/(\hbar c)$ ,  $k_{\text{c.m.}}^2 = 2\mu(E^* - S_{\text{1n}})/\hbar^2$  with  $E^* = E_{\text{c.m.}} + S_{\text{1n}}$  and  $\mu = (M_{^{19}\text{N}} * M_{\text{n}})/(M_{^{19}\text{N}} + M_{\text{n}})$  is the reduced mass of the system  $^{19}\text{N} + \text{n}$ . Additionally,  $J$  are the spins of the incoming and outgoing particle. With  $^{20}\text{N}$  as incoming nucleus, index A stands for  $^{20}\text{N}$  with  $J_{\text{A}} = 2$  for the ground state, index B represents the outgoing  $^{19}\text{N}$  with  $J_{\text{B}} = 1/2$  for the ground state and  $J_{\text{B}} = 3/2$  for the first excited state, and index n indicates the neutron with  $J_{\text{n}} = 1/2$ .

Integrating over energies of  $E^* \in [0, 20]$  MeV, the neutron capture cross section of the ground state of  $^{19}\text{N}$  amounts to  $\sigma_{\gamma,n}(^{19}\text{N}, \text{g.s.}) = (0.0050 \pm 0.3035^{\text{stat}})$  mb. As the statistical uncertainty is too large, only an upper limit with 90 % confidence level can be given  $\sigma_{\gamma,n}(^{19}\text{N}, \text{g.s.}) \leq (0.395)$  mb.

The neutron capture cross section of the first excited state of  $^{19}\text{N}$  amounts to  $\sigma_{\gamma,n}(^{19}\text{N}, 1\text{st}) = (0.092 \pm 0.028^{\text{stat}})$  mb.

The ground state is supposed to be the most populated state of  $^{19}\text{N}$  in astrophysical sites. Thus, it is the most interesting cross section to be investigated for the r-process. Due to the high statistical uncertainty only an upper limit could be presented. As the first excited state of  $^{19}\text{N}$  with 1141 MeV is rather high energetic, this state is supposed to be not significantly populated. Therefore, in both cases, a statement about the impact of the measured values to astrophysic scenarios cannot be given.

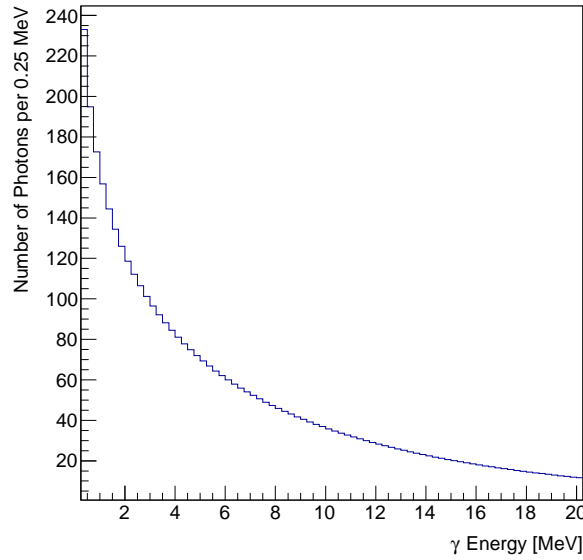


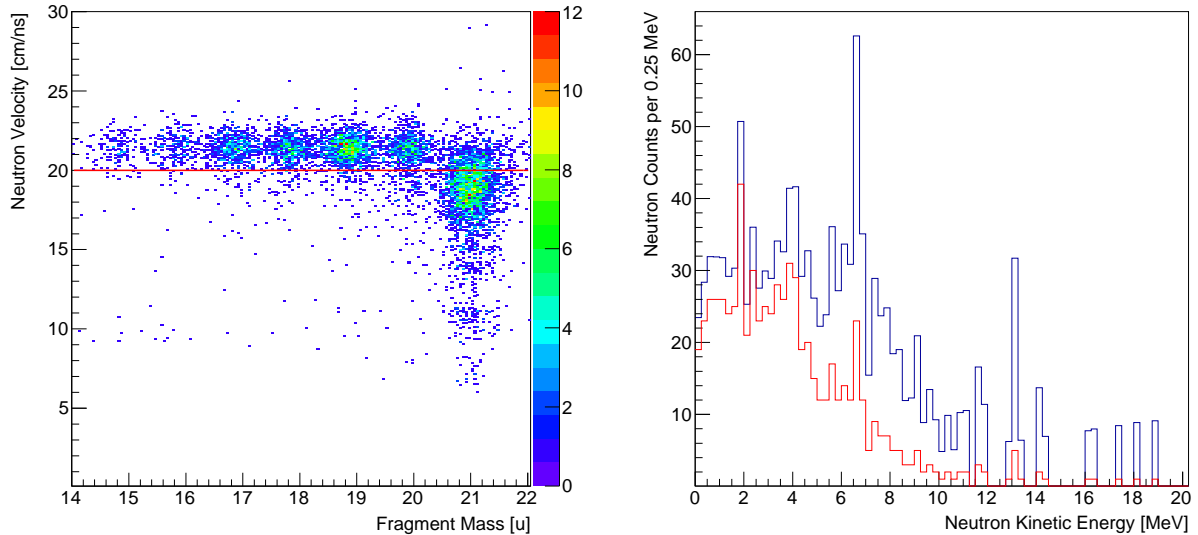
Figure 46: Virtual photon spectrum of E1 multipolarity for  $^{20}\text{N}$  impinging onto a Pb target with a beam velocity of  $\beta = 0.74$ .

## 5 Data Analysis for $^{21}\text{N}(\gamma, n)^{20}\text{N}$ reaction

The analysis of the Coulomb dissociation of  $^{21}\text{N}$  was basically similar to the procedures described in the previous chapter 4. Here, small differences are only mentioned briefly. For details on the basic procedures, a reference to the proper previous section will be given.

The incoming particle identification was similar as described in section 4.1. Here, a cut on the A/Z ratio between 2.95 and 3.08 was performed. Both the cuts on the charge of the incoming particle (4.1) and the charge of the outgoing heavy charged reaction fragment (4.2) were identical to the previous analysis.

Although the distribution of the neutron velocity was slightly different compared to the one in the previous chapter 4.3, due to a different kinetic energy of the impinging particle, the same cut on the neutron velocity at 20 cm/ns was applied to exclude scattered neutrons (figure 47a).



(a) Fragment mass number in relation to the neutron velocity to identify scattered neutrons. All events with a neutron velocity lower than 20 cm/ns were excluded (indicated by red line). Here,  $^{21}\text{N}$  impinge onto a Pb target, requiring one hit in LAND, accepting only outgoing heavy fragments of charge number  $Z=7$ .

(b) One-neutron emission spectrum of  $^{21}\text{N}$  impinging onto a Pb target measured with LAND (red line) and corrected for the LAND efficiency (dark blue line).

Figure 47: Neutrons emitted during reactions of  $^{21}\text{N}$  with the Pb target.

For the identification of the masses of the outgoing heavy fragments, the tracker calibration was kept identically as described in section 4.5.1. The measured masses of the outgoing fragments and their mass resolution are summarized in table 13.

The correction for the total efficiency of LAND was similar to the procedure described in section 4.7. The energy distribution of the neutrons emitted during  $^{21}\text{N}(\gamma, n)^{20}\text{N}$  reactions is illustrated in figure 47b. The efficiency in relation to the kinetic energy of the neutron in the system of the impinging  $^{21}\text{N}$  is given in figure 35a (red line).

Nucleus	Mean [u]	Sigma [u]	Mass Resolution [%]
$^{21}\text{N}$	21.02	0.30	1.40
$^{20}\text{N}$	19.90	0.22	1.12
$^{19}\text{N}$	18.86	0.23	1.24

Table 13: Masses and mass resolution derived by the tracker. A Gaussian fit was applied to extract the mean and the sigma. Here, incoming  $^{21}\text{N}$  impinge onto a Pb target, the charge of the heavy fragment is  $Z=7$ , requiring one hit in LAND and accepting only events with a neutron velocity  $v_n > 20 \text{ cm/ns}$ .

## 5.1 Gamma Spectra

The gamma spectrum of deexciting  $^{20}\text{N}$  nuclei were derived in a similar way as described in section 4.8, especially, the threshold of the single crystals ( $E_{\gamma, \text{crystal}} > 0.3 \text{ MeV}$ ) to be added to a cluster (resulting in the cluster energy  $E_\gamma$ ) was identical. Afterwards, the cluster energies of all identified clusters  $i$  per one impinging nucleus were summed up to  $E_{\gamma, \text{sum}}$  (compare equation 35 in section 4.8) if they exceeded the single cluster threshold of  $E_{\gamma, i} > 0.4 \text{ MeV}$  (depicted in figure 48 blue line).

Furthermore, the background radiation was estimated by utilizing the  $E_{\gamma, \text{sum}}$ -spectrum of non-reacted  $^{21}\text{N}$  nuclei (see figure 48 red line).

Figure 48 reveals a signal at 850 keV which refers to the first excited state of  $^{20}\text{N}$  (measured by D. Sohler et al. [43], depicted in figure 49). Also a peak-like structure is visible in the background spectrum estimated with  $^{21}\text{N}$ . As there, the intensity is much lower than in the spectrum of  $^{20}\text{N}$  this did not disturb the identification and the separation between the first excited state and other excited states.

It is obvious that a large part of the gamma spectrum of  $^{20}\text{N}$  is concentrated in the peak at 850 keV. Almost no higher energetic photons were detected. Only a small peak-like structure is occurring at an energy of 1.35 MeV which was already measured by [43]. D. Sohler et al. measured a few additional signals in the close vicinity of 850 keV belonging to other excited states. Therefore, it cannot clearly be stated that the signal at 850 keV originates only from the first excited state. Anyway, for further analysis this structure was utilized to identify transitions into the first excited state.

Again, an efficiency correction had to be applied. Here, a photo peak efficiency of 74 % ( $\pm 5 \%$ ) was extracted out of figure 38 for 850 keV. As almost no higher energetic gammas were detected, a mean gamma energy of 1.1 MeV was extracted in the range of 0.4 to 5 MeV resulting in a mean detection efficiency of 81 % ( $\pm 8 \%$ ).

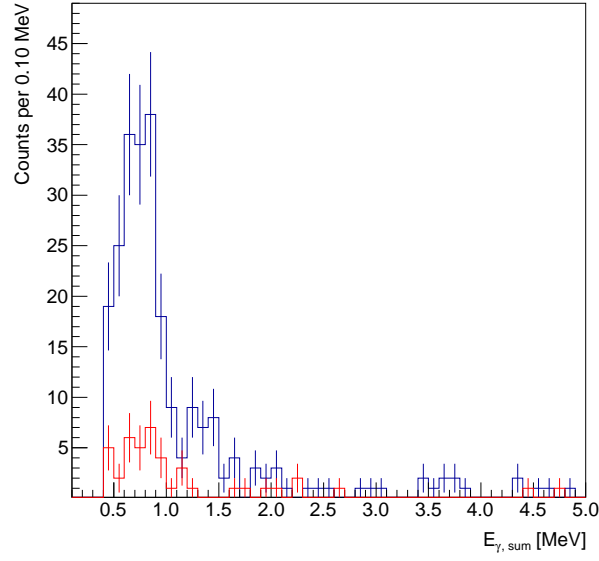


Figure 48: Gamma Sum Spectrum of outgoing  $^{20}\text{N}$  on a Pb target (blue line) and gamma background of  $^{21}\text{N}$  (red line).

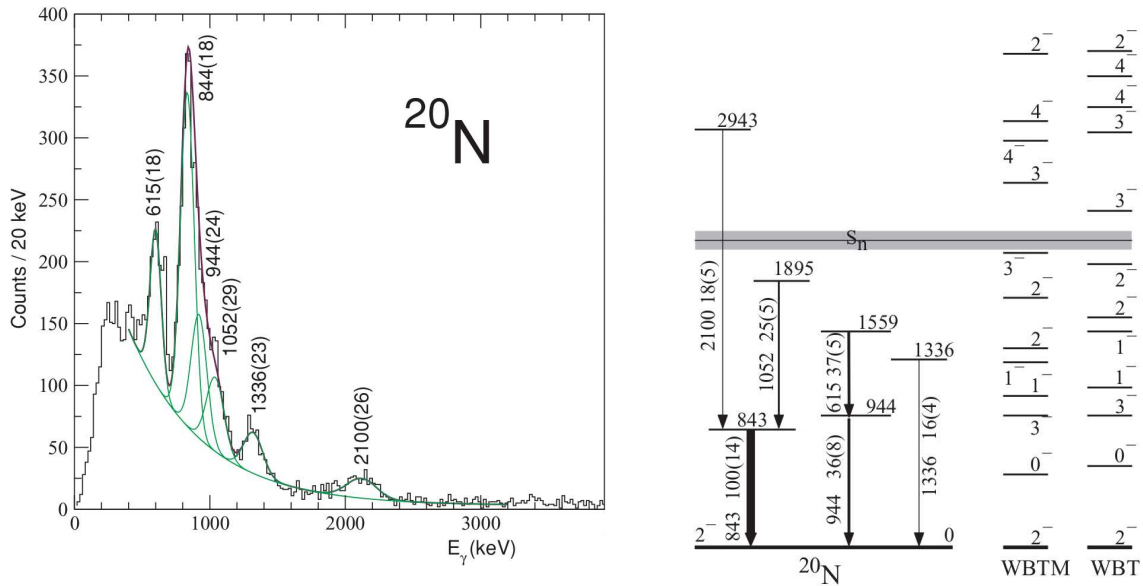


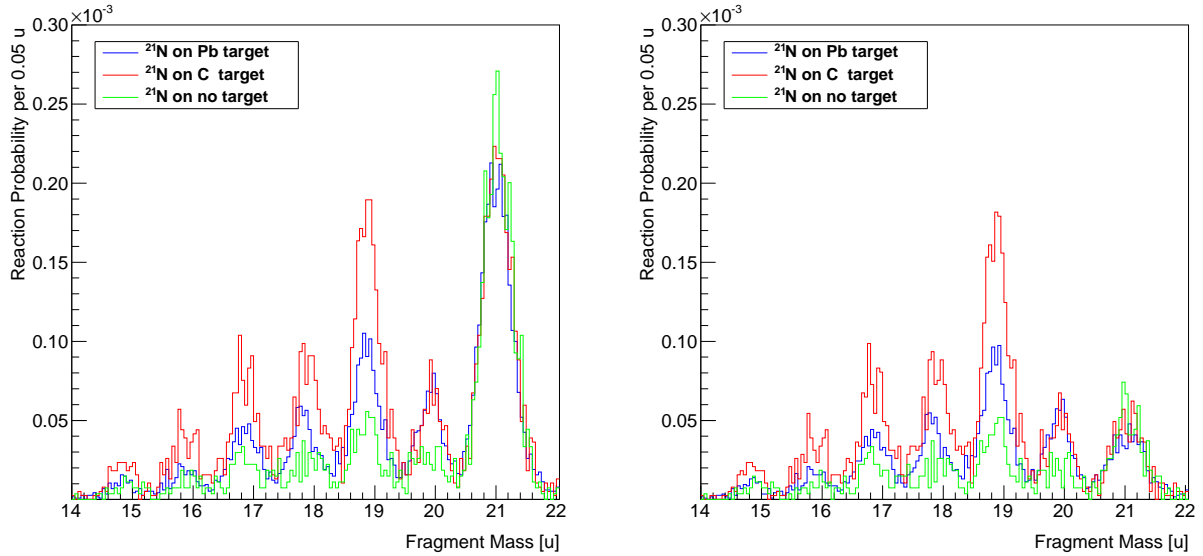
Figure 49: Gamma spectrum (left panel) and level scheme (right panel) of  $^{20}\text{N}$  derived by D. Sohler et al. 2008 [43].

## 5.2 Coulomb Excitation Cross Section

The Coulomb excitation cross section was derived similarly as described in section 4.9.

### 5.2.1 Data Normalization and Reaction Probabilities

The number of incoming particles was estimated from the tracked data counting all outgoing N-isotopes (as described in detail in section 4.9.1). This number, then, was utilized to normalize the derived spectra to get the reaction probabilities of the  $^{21}\text{N}$  nuclei to react with the Pb-, C-, and empty target (see figure 50).



(a) Reaction probability without cut on the neutron velocity

(b) Reaction probability with cut on neutron velocity at 20 cm/ns.

Figure 50: Reaction probability distribution of incoming  $^{21}\text{N}$  impinging on different targets.

### 5.2.2 Scaling Factor

The scaling factor which scales the nuclear contribution of the  $^{21}\text{N}$  measured with the C target relative to the nuclear contribution of the Pb target was calculated via formula 37 (section 4.9.2) to  $\alpha = 1.718$ . This tiny difference to the scaling factor of  $^{20}\text{N}$  ( $\alpha = 1.725$ ) is negligible as it only changes the final Coulomb dissociation cross section by 0.1 %.

### 5.2.3 Error Estimation

The statistical and systematic errors were estimated by the procedure mentioned in section 4.9.3. A summary of the statistical uncertainties with respect to the variation of the width of the cuts on the incoming particle identification is given in table 14. Furthermore, systematic uncertainties were derived by the variation of the cuts on the incoming particle identification while observing the resulting cross section (table 15). Again, the uncertainty of the LAND efficiency amounting to 6 % was taken into account. Furthermore, the uncertainty of the Crystal Ball efficiency had to be taken into account. It amounted to 5 % for the photo peak efficiency and 8 % for the mean detection efficiency.



Target	acceptance window	in Z	in A/Z	#incoming	#outgoing	$u_{stat}$
Pb	$3\sigma$	[6.34 ; 7.44]	[2.95 ; 3.07]	1151312	701	4.0 mb
C				385200	219	2.4 mb
empty				269600	76	7.6 mb
Pb	$1\sigma$	[6.71 ; 7.07]	[2.99 ; 3.03]	559264	340	5.7 mb
C				188032	95	3.3 mb
empty				133328	37	10.8 mb

Table 14: Number of incoming and outgoing events for the lead, carbon and empty target with respect to a 1 sigma and 3 sigma cut on the incoming particle properties (Z and A/Z). Furthermore, the contribution to the statistical uncertainty is given (last column). The total statistical uncertainty amounts to  $u_{stat}(3\sigma)=8.9$  mb and  $u_{stat}(1\sigma)=12.6$  mb.

#### 5.2.4 Results of the Coulomb Excitation Cross Section

Afterwards, the reaction probabilities were scaled with the target properties and the nuclear scaling factor to derive the Coulomb dissociation cross section (compare section 4.9.4). The partial contributions of the targets utilized for the analysis of the  $^{21}\text{N}(\gamma, n)^{20}\text{N}$  cross section are illustrated in figure 51a while the mass distribution versus the final Coulomb dissociation cross section is given in figure 51b.

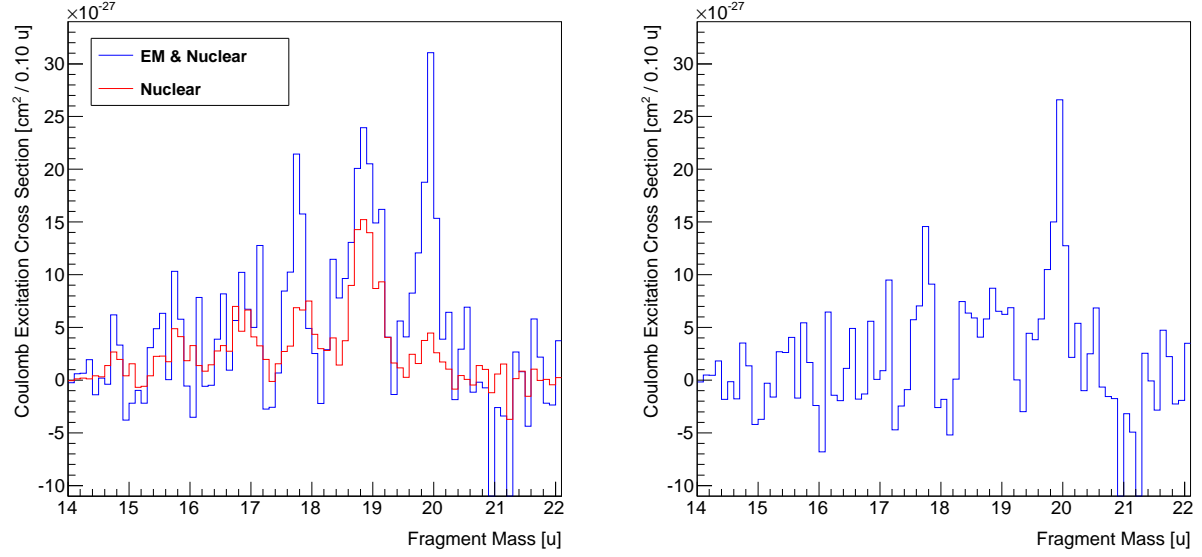
In order to estimate the Coulomb cross section of the  $^{21}\text{N}(\gamma, n)^{20}\text{N}$  reaction, the integral of the peak without any fit was extracted in the range of  $A \in [19.5; 20.5]$ .

The results of the Coulomb excitation cross section and systematic uncertainties derived by sigma variations of the parameters of the incoming particle identification, are summarized in table 15. Beside that, Coulomb dissociation cross sections of transitions into excited and non-excited states of the outgoing  $^{20}\text{N}$  nucleus (discussed in section 5.3) are provided therein.

The Coulomb dissociation cross section of the  $^{21}\text{N}(\gamma, n)^{20}\text{N}$  reaction amounts to  $\sigma_{\text{CoulEx}, ^{21}\text{N}} = (79.1 \pm 8.9^{\text{stat}} \pm 6.1^{\text{sys}}_{\text{inPID}} \pm 4.9^{\text{sys}}_{\text{LANDefficiency}})$  mb.

acceptance window		3.0	2.5	2.0	1.5	1.0	mean	standard deviation
		$\sigma$	$\sigma$	$\sigma$	$\sigma$	$\sigma$		
Coul. Ex. (total)	[mb]	83.5	84.8	78.6	69.2	79.1	79.1	6.1
Coul. Ex. (all excited states)	[mb]	53.4	53.0	53.4	47.0	55.3	52.4	3.1
Coul. Ex. (ground state)	[mb]	30.2	31.8	25.2	22.2	23.8	26.6	4.2
Coul. Ex. ( $E_{\gamma, \text{sum}}=850$ keV)	[mb]	48.5	48.7	47.0	44.7	54.6	48.7	3.7

Table 15: Coulomb excitation cross section in correlation with sigma variations on the incoming Z and A/Z-ratio for estimation of systematic uncertainties. The first row represents the results derived in section 5.2 which represents the total Coulomb dissociation cross section while the last three rows represent the results described in section 5.3: transitions into only excited states, the ground state, the first excited state (with  $E_{\gamma, \text{sum}}=843$  keV) of the outgoing  $^{20}\text{N}$ . For further description see section 5.3.



(a) Partial dissociation cross sections of  $^{21}\text{N}$  versus the mass number of the outgoing reaction fragment. The plot illustrates electromagnetic (EM) + Nuclear contribution as measured with the lead target (blue line) and the Nuclear contribution (as measured with the carbon target and scaled to the lead nuclei) after proper subtraction of the beamline contribution.

(b) Pure Coulomb excitation cross section of  $^{21}\text{N}$  derived by the subtraction of the histograms in (a).

Figure 51: Partial dissociation cross sections and Coulomb dissociation cross section of the  $^{21}\text{N}(\gamma, n)^{20}\text{N}$  reaction.

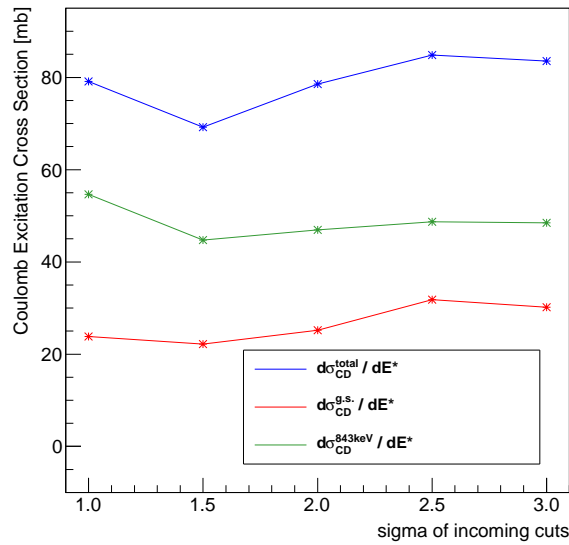


Figure 52: Coulomb excitation cross section of  $^{21}\text{N}$  in dependence of the sigma variation of the incoming Z and A/Z. Illustration of table 15.

### 5.3 Excitation Energy Spectrum

The excitation energy spectra for the Coulomb dissociation of  $^{21}\text{N}$  into excited and non-excited states of  $^{20}\text{N}$  were derived by utilizing equation 39 in section 4.10. Details on the analysis procedure can be found in section 4.10.

The total (or inclusive) excitation energy spectrum also includes events when no gamma was detected. In that case,  $E_{\gamma, \text{sum}}$  was set to zero and only the kinematics without the gamma energy were utilized to compute the excitation energy spectrum.

In order to separate transitions into the ground state and excited states of  $^{20}\text{N}$ , the  $E_{\gamma, \text{sum}}$ -spectrum was employed. Transitions into any excited state were defined to fulfill  $E_{\gamma, \text{sum}} \geq 0.4 \text{ MeV}$ . The derived excitation energy spectrum was corrected for the mean detection efficiency of the Crystal Ball of  $(81 \pm 8) \%$  (at a mean gamma energy of 1.1 MeV). The excitation energy spectrum of transitions into any excited state is depicted in figure 54.

Transitions of  $^{21}\text{N}$  into the ground state of  $^{20}\text{N}$  were derived by subtracting the efficiency corrected spectrum of all excited states from the total excitation energy spectrum (figure 55).

The excitation energy spectrum of the first excited state at 843 keV was derived, too (figure 56). Here, events which fulfill  $E_{\gamma, \text{sum}} \in (0.4; 1.3]$  were selected from the measured  $E_{\gamma, \text{sum}}$ -spectrum. Afterwards, a Crystal Ball detection efficiency of  $(74 \pm 5) \%$  for the gamma energy of 850 keV was applied.

Each excitation energy spectrum was integrated to derive the Coulomb dissociation cross sections for the total reaction, for Ground state transitions, transitions into all excited states and the transition into the first excited state. Variations on the incoming particle identification were performed to derive uncertainties of the cross sections stemming from these cuts (compare table 15). The Coulomb dissociation cross sections for each part of the reactions with their specific uncertainties are given in table 16.

### 5.4 Discussion

Table 16 indicates, that 66 % of total Coulomb dissociation cross section of  $^{21}\text{N}$  transit into excited states of  $^{20}\text{N}$  which is significantly less than for the Coulomb dissociation of  $^{20}\text{N}$ . Furthermore, 33 % of all Coulomb dissociating  $^{21}\text{N}$  nuclei pass into the ground state of  $^{20}\text{N}$ . This is significantly more than for the Coulomb dissociation of  $^{20}\text{N}$ . 62 % of the total Coulomb dissociation cross section are governed by transitions into the first excited state of  $^{20}\text{N}$ . These represent 93 % of the transitions into any excited state. Thus, transitions into the first excited state are more prominent for the Coulomb dissociation of  $^{21}\text{N}$  than for  $^{20}\text{N}$ .

The total excitation energy spectrum of the Coulomb dissociation of  $^{21}\text{N}$  (figure 53b) does not show any entry in the energy range between 0 and 4 MeV. The first bin at 4.5 MeV consists of values that are consistent with zero within the uncertainties. As the one neutron separation energy of  $^{21}\text{N}$  is  $S_{1n}=4.59 \text{ MeV}$  [40], this is expected. Afterwards, there is a structure significantly above zero for excitation energies between 5.0 MeV and 11.0 MeV peaking at 6.5 MeV. Another small peak is visible at 13.5 MeV. The cross section becomes consistent with zero for excitation energies higher than 16 MeV.

The excitation energy spectrum for transitions into any excited state of  $^{20}\text{N}$  (figure 54) show a significant increase at 5.0 MeV (slightly above  $S_{1n}$ ) while no entries are present for lower excitation energies. There is a structure for excitation energies between 5.0 and

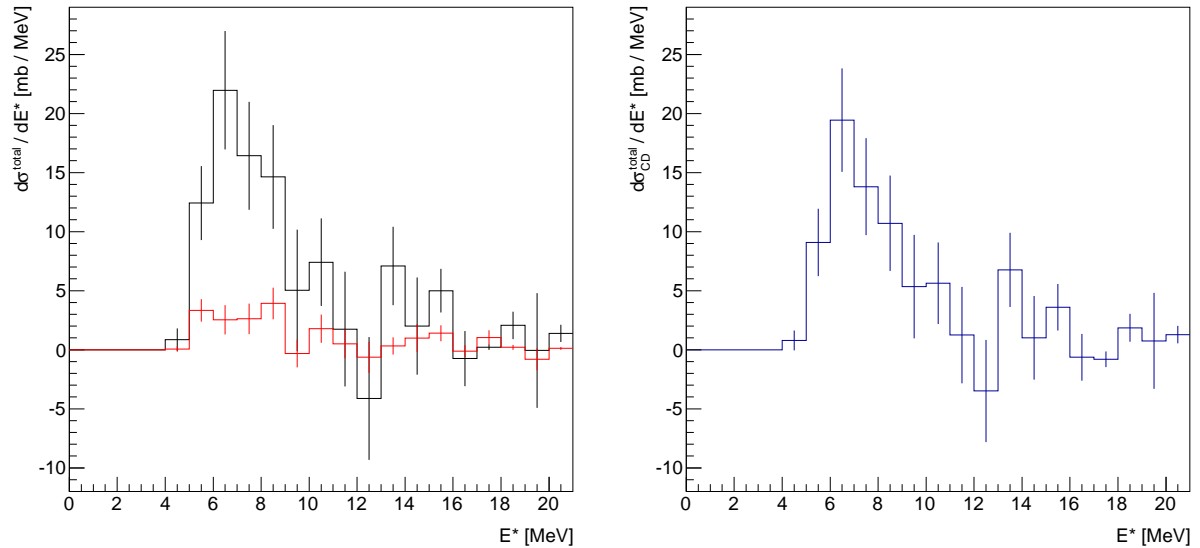
12.0 MeV with a peak at 6.5 MeV. A second elevation is visible for excitation energies between 13.0 and 16.0 MeV. Afterwards, the spectrum decreases to zero consistence.

Transitions into the ground state of  $^{20}\text{N}$  (figure 44) do not show entries between 0 and 4.0 MeV. From 4.0 to 9 MeV there is a plateau-like structure without any dominant peak. After 9 MeV values are consistent with zero. Small peaks occurring for energies higher than 9 MeV vanish almost entirely within the uncertainty of the data.

The excitation energy spectrum of transitions of  $^{21}\text{N}$  into the first excited state of  $^{20}\text{N}$  at 843 keV are shown in figure 56. The spectrum begins at 5.0 MeV (slightly above  $S_{1n}$ ) and shows a significant irregular structure up to values of 12 MeV with a peak at 6.5 MeV. A small elevation at 13.5 MeV is visible. For excitation energies greater than 16 MeV the spectrum becomes consistent with zero.

CDCS (total)	(79.1 $\pm 8.9^{\text{stat}}$ $\pm 6.1^{\text{sys}}_{\text{inPID}}$ $\pm 4.9^{\text{sys}}_{\text{LAND}}$ )	mb
CDCS (all excited states)	(52.4 $\pm 7.1^{\text{stat}}$ $\pm 3.1^{\text{sys}}_{\text{inPID}}$ $\pm 3.1^{\text{sys}}_{\text{LAND}}$ $\pm 4.2^{\text{sys}}_{\text{CB}}$ )	mb
CDCS (ground state)	(26.6 $\pm 5.0^{\text{stat}}$ $\pm 4.2^{\text{sys}}_{\text{inPID}}$ $\pm 1.6^{\text{sys}}_{\text{LAND}}$ $\pm 2.1^{\text{sys}}_{\text{CB}}$ )	mb
CDCS ( $E_{\gamma,\text{sum}}=850$ keV)	(48.7 $\pm 6.8^{\text{stat}}$ $\pm 3.7^{\text{sys}}_{\text{inPID}}$ $\pm 2.9^{\text{sys}}_{\text{LAND}}$ $\pm 2.4^{\text{sys}}_{\text{CB}}$ )	mb

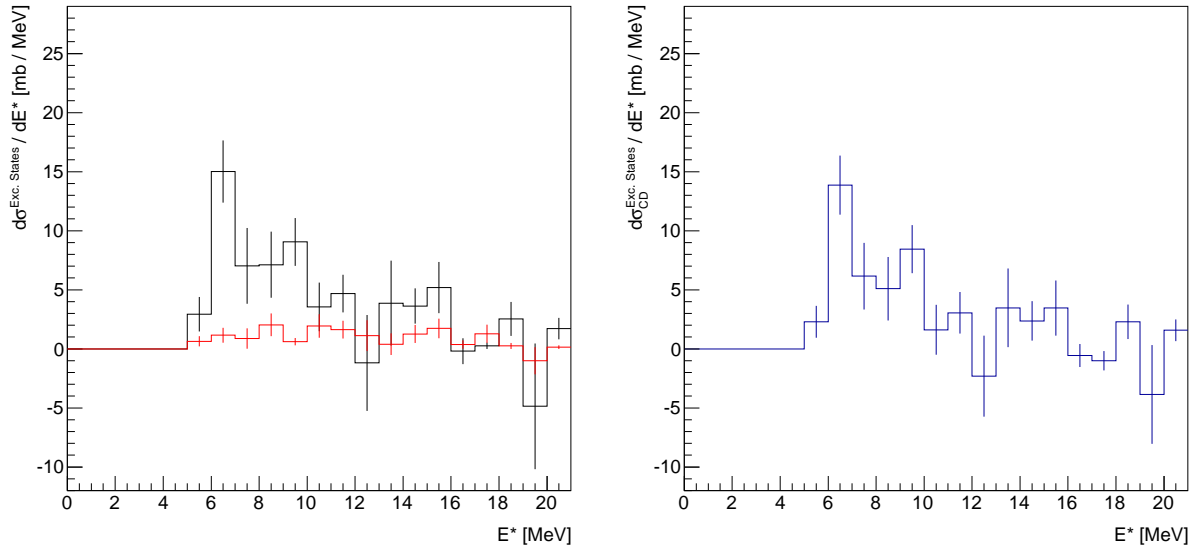
Table 16: Summary of the Coulomb dissociation cross section of the  $^{21}\text{N}$  for a) the total reaction, b) transitions into any excited state of the outgoing  $^{20}\text{N}$ , c) transitions into the ground state of the outgoing  $^{20}\text{N}$ , d) transitions into the first excited state of the outgoing  $^{20}\text{N}$  with proper uncertainties.



(a) Total excitation energy spectrum of  $^{21}\text{N}$  impinging onto the Pb target (black line) for visualization of the Coulomb+Nuclear contribution and onto the C target (red line) for visualizing the Nuclear contribution, each after subtraction of the beamline background.

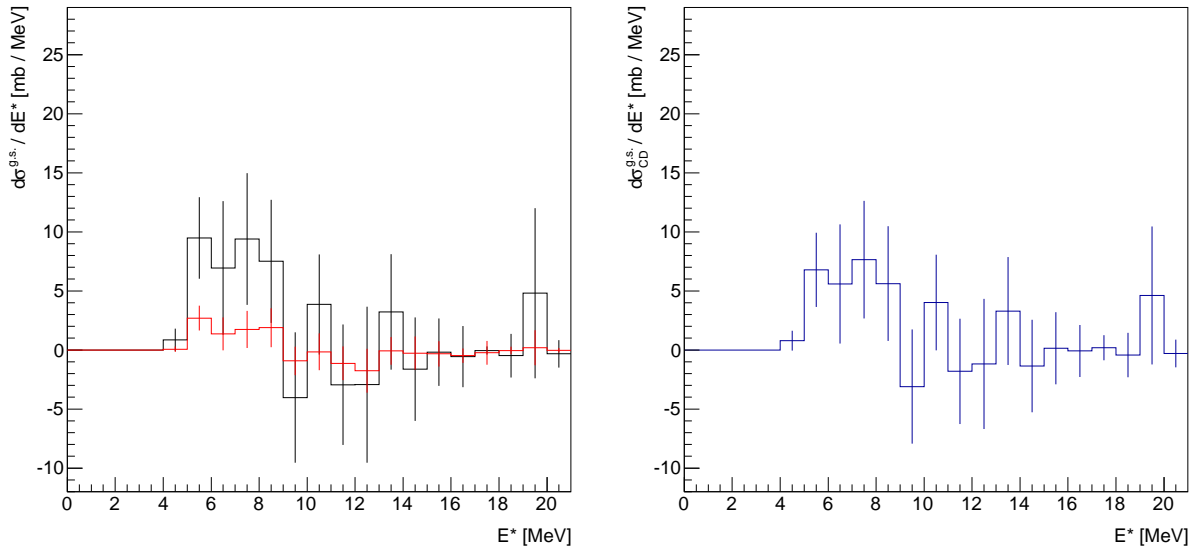
(b) Final total Coulomb dissociation excitation energy spectrum (derived from the subtraction of the histograms to the left).

Figure 53: Excitation energy spectra for the total Coulomb dissociation of  $^{21}\text{N}$ .



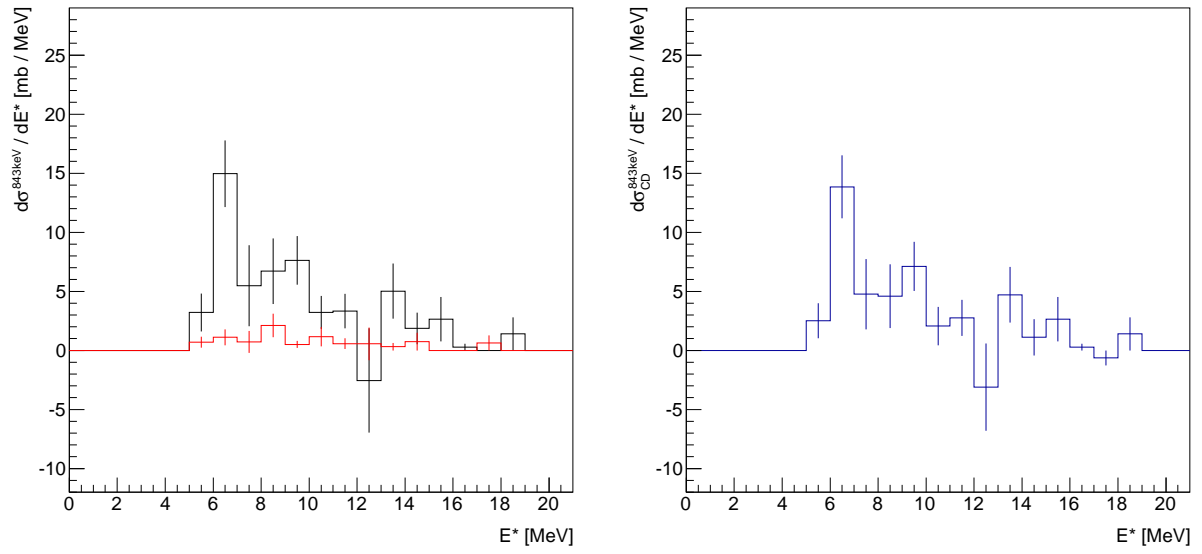
(a) Excitation energy spectrum of  $^{21}\text{N}$  impinging onto the Pb target (black line) for visualization of the Coulomb+Nuclear contribution and onto the C target (red line) for visualizing the Nuclear contribution, each after subtraction of the beamline background. (b) Coulomb dissociation excitation energy spectrum (derived from the subtraction of the histograms to the left).

Figure 54: Excitation energy spectra for the Coulomb dissociation of  $^{21}\text{N}$  into any excited state.



(a) Excitation energy spectrum of  $^{21}\text{N}$  impinging onto the Pb target (black line) for visualization of the Coulomb+Nuclear contribution and onto the C target (red line) for visualizing the Nuclear contribution, each after subtraction of the beamline background. (b) Final Coulomb dissociation excitation energy spectrum of  $^{21}\text{N}$  for ground state transitions (derived from the subtraction of the histograms to the left).

Figure 55: Excitation energy spectra for ground state transitions of the  $^{21}\text{N}(\gamma, n)^{20}\text{N}$  reaction.



(a) Excitation energy spectrum of  $^{21}\text{N}$  impinging onto the Pb target (black line) for visualization of the Coulomb+Nuclear contribution and onto the C target (red line) for visualizing the Nuclear contribution, each after subtraction of the beamline background.

(b) Final Coulomb dissociation excitation energy spectrum for transitions into the first excited state of the  $^{20}\text{N}$  at 843 keV (derived from the subtraction of the histograms to the left).

Figure 56: Excitation energy spectra for transitions into the first excited state of the  $^{20}\text{N}$  at 843 keV of the  $^{21}\text{N}(\gamma, n)^{20}\text{N}$  reaction.

## 5.5 Photo Absorption and Neutron Capture Cross Section

Following the derivations described in section 4.12, the neutron capture cross section can be calculated via equation 45:

$$\sigma_{n,\gamma} = \frac{2(2J_A + 1)}{(2J_B + 1)(2J_n + 1)} \frac{k_\gamma^2}{k_{\text{c.m.}}^2} \sigma_{\gamma,n} .$$

Here, index A denotes the impinging  $^{21}\text{N}$  with  $J_A = 1/2$  for the ground state, index B represents the outgoing  $^{20}\text{N}$  with  $J_B = 2$  for the ground state and  $J_B=3$  for the first excited state.

An integration over the excitation energies  $E^* \in [0, 20]$  MeV was performed resulting in a neutron capture cross section of the ground state of  $^{19}\text{N}$  of  $\sigma_{\gamma,n}(^{20}\text{N}, \text{g.s.}) = (0.072 \pm 0.078^{\text{stat}})$  mb. Again, the statistical uncertainty is larger than the value itself. Thus, only an upper limit with 90 % confidence level can be given with  $\sigma_{\gamma,n}(^{20}\text{N}, \text{g.s.}) \leq 0.172$  mb.

The neutron capture cross section of the first excited state of  $^{19}\text{N}$  was found to be  $\sigma_{\gamma,n}(^{20}\text{N}, 1\text{st}) = (0.073 \pm 0.026^{\text{stat}})$  mb.

As already pointed out in section 4.12, the impact on astrophysical scenarios is hard to determine because the interesting neutron capture cross section of the ground state of  $^{20}\text{N}$  can only be given with an upper limit due to high statistical uncertainties and the first excited state  $^{20}\text{N}$  with an energy of 843 keV is supposed to be rarely populated in astrophysical sites.





## References

- [1] R. Reifarth, C. Lederer, and F. Käppeler. Neutron reactions in astrophysics. *Journal of Physics G: Nuclear and Particle Physics*, **41**: p. 053101, 2014.
- [2] K. Takahashi, J. Witti, and H.-T. Janka. Nucleosynthesis in neutrino-driven winds from protoneutron stars. 2. The R-process. *Astronomy and Astrophysics*, **286**: p. 857, 1994.
- [3] T. Sasaqui, T. Kajino, G. J. Mathews, K. Otsuki, et al. Sensitivity of r-Process Nucleosynthesis to Light-Element Nuclear Reactions. *The Astrophysical Journal*, **634**: p. 1173, 2005.
- [4] J. J. Cowan, F.-K. Thielemann, and J. W. Truran. The R-process and nucleochronology. *Physics Reports*, **208**: p. 267, 1991.
- [5] M. Terasawa, K. Sumiyoshi, T. Kajino, G. J. Mathews, et al. New Nuclear Reaction Flow during r-Process Nucleosynthesis in Supernovae: Critical Role of Light, Neutron-rich Nuclei. *The Astrophysical Journal*, **562**: p. 470, 2001.
- [6] T. Aumann. Prospects of nuclear structure at the future GSI accelerators. *Progress in Particle and Nuclear Physics*, **59**: p. 3, 2007. International Workshop on Nuclear Physics 28th Course Radioactive Beams, Nuclear Dynamics and Astrophysics Ettore Majorana Center for Scientific Culture.
- [7] The R3B Collaboration. Technical Report for the Design, Construction and Commissioning of NeuLAND: The High-Resolution Neutron Time-of-Flight Spectrometer for R3B. submitted to FAIR in 2011.
- [8] The R3B Collaboration. Technical Proposal for the Design, Construction, Commissioning and Operation of R3B. submitted to FAIR in 2005.
- [9] P. Fonte, R. F. Marques, J. Pinhão, N. Carolino, et al. High-resolution RPCs for large TOF systems. *Nuclear Instruments and Methods in Physics Research Section A: Accelerators, Spectrometers, Detectors and Associated Equipment*, **449**: p. 295, 2000.
- [10] Proceedings of the XI Workshop on Resistive Plate Chambers and Related Detectors. Frascati (Rome), Italy, 5-10 February 2012.
- [11] S. An, Y. Jo, J. Kim, M. Kim, et al. A 20ps timing device-A Multigap Resistive Plate Chamber with 24 gas gaps. *Nuclear Instruments and Methods in Physics Research Section A: Accelerators, Spectrometers, Detectors and Associated Equipment*, **594**: p. 39, 2008.
- [12] A. Blanco, R. Ferreira-Marques, C. Finck, P. Fonte, et al. A large area timing RPC. *Nuclear Instruments and Methods in Physics Research Section A: Accelerators, Spectrometers, Detectors and Associated Equipment*, **485**: p. 328, 2002.
- [13] D. Yakorev, T. Aumann, D. Bemmerer, K. Boretzky, et al. Prototyping and tests for an MRPC-based time-of-flight detector for 1GeV neutrons. *Nuclear Instruments and Methods in Physics Research Section A: Accelerators, Spectrometers, Detectors and Associated Equipment*, **654**: p. 79, 2011.

- [14] M. Röder, T. Aumann, D. Bemmerer, K. Boretzky, et al. Prototyping a 2m x 0.5m MRPC-based neutron TOF-wall with steel converter plates. *Journal of Instrumentation*, **7**: p. P11030, 2012.
- [15] M. Röder, Z. Elekes, T. Aumann, D. Bemmerer, et al. Efficiency determination of resistive plate chambers for fast quasi-monoenergetic neutrons. *The European Physical Journal A*, **50**: 112, 2014.
- [16] Z. Elekes, T. Aumann, D. Bemmerer, K. Boretzky, et al. Simulation and prototyping of 2m long resistive plate chambers for detection of fast neutrons and multi-neutron event identification. *Nuclear Instruments and Methods in Physics Research Section A: Accelerators, Spectrometers, Detectors and Associated Equipment*, **701**: p. 86, 2013.
- [17] A. V. Prokofiev, J. Blomgren, O. Byström, C. Ekström, et al. The TSL neutron beam facility. *Radiation Protection Dosimetry*, **126**: p. 18, 2007.
- [18] R. Bevilacqua, S. Pomp, V. Simutkin, M. Hayashi, et al. Medley spectrometer for light ions in neutron-induced reactions at 175MeV. *Nuclear Instruments and Methods in Physics Research Section A: Accelerators, Spectrometers, Detectors and Associated Equipment*, **646**: p. 100, 2011.
- [19] V. Eismont, A. Prokofyev, and A. Smirnov. Thin-film breakdown counters and their applications (review). *Radiation Measurements*, **25**: p. 151, 1995. Nuclear Tracks in Solids.
- [20] M. Ciobanu, A. Schuttauf, E. Cordier, N. Herrmann, et al. A Front-End Electronics Card Comprising a High Gain/High Bandwidth Amplifier and a Fast Discriminator for Time-of-Flight Measurements. *Nuclear Science, IEEE Transactions on*, **54**: p. 1201, 2007.
- [21] M. Ciobanu, N. Herrmann, K. Hildenbrand, M. Kis, et al. PADI, a fast Preamplifier - Discriminator for Time-of-Flight measurements. In *Nuclear Science Symposium Conference Record, 2008. NSS '08. IEEE*, p. 2018–2024. 2008.
- [22] F. Gabriel, P. Gippner, E. Grosse, D. Janssen, et al. The Rossendorf radiation source ELBE and its FEL projects. *Nuclear Instruments and Methods in Physics Research Section B: Beam Interactions with Materials and Atoms*, **161–163**: p. 1143, 2000.
- [23] R. Kotte, U. Lehnert, L. Naumann, and A. Wagner. Anordnung und Verfahren zur Erzeugung einzelner relativistischer Elektronen. Patent DE 102008054676A1, 2008.
- [24] K. Koch, H. Hardel, R. Schulze, E. Badura, et al. A new TAC-based multichannel front-end electronics for TOF experiments with very high time resolution. *Nuclear Science, IEEE Transactions on*, **52**: p. 745, 2005.
- [25] C. Caesar. New LAND electronics - TacQuila17 - Version 0.8. TacQuila-manual, GSI, private communication, July 2011.
- [26] L. Naumann, R. Kotte, D. Stach, and J. Wüstenfeld. High-rate timing RPC with ceramics electrodes. *Nuclear Instruments and Methods in Physics Research Section A: Accelerators, Spectrometers, Detectors and Associated Equipment*, **635**: p. S113, 2011. PhotonDiag 2010.

- 
- [27] RP-408 PLASTIC SCINTILLATOR Data Sheet.  
[http://www.rexon.com/RP\\_408.pdf](http://www.rexon.com/RP_408.pdf), visited 08.05.2014.
- [28] R8619 Photomultiplier Assembly Data Sheet.  
[http://www.hamamatsu.com/resources/pdf/etd/R8619\\_TPMH1331E03.pdf](http://www.hamamatsu.com/resources/pdf/etd/R8619_TPMH1331E03.pdf),  
visited 08.05.2014.
- [29] O. Ershova. *Coulomb Dissociation Reactions on Molybdenum Isotopes for Astrophysics Applications*. Ph.D. thesis, University of Frankfurt, 2012.
- [30] F. Wamers. *Quasi-Free-Scattering and One-Proton-Removal Reactions with the Proton-Dripline Nucleus  $^{17}\text{Ne}$  at Relativistic Beam Energies*. Ph.D. thesis, Technical University of Darmstadt, 2011.
- [31] C. Langer. *Coulomb Dissociation of  $^{31}\text{Cl}$  and  $^{32}\text{Ar}$  - constraining the  $rp$  process*. Ph.D. thesis, University of Frankfurt, 2012.
- [32] C. Caesar. *Beyond the Neutron Drip-Line: Superheavy Oxygen Isotopes*. Ph.D. thesis, Technical University of Darmstadt, 2012.
- [33] <http://web-docs.gsi.de/~rplag/land02/img/POS-00.gif>,  
visited 16.12.2013.
- [34] [http://web-docs.gsi.de/~rplag/land02/img/ROLU\\_offen.gif](http://web-docs.gsi.de/~rplag/land02/img/ROLU_offen.gif),  
visited 16.12.2013.
- [35] V. Metag, R. Fischer, W. Kühn, R. Mühllhans, et al. Physics with  $4\pi$ - $\gamma$ -detectors. *Nuclear Physics A*, **409**: p. 331, 1983.
- [36] K. Boretzky, A. Grünschloß, S. Ilievski, P. Adrich, et al. Two-phonon giant resonances in  $^{136}\text{Xe}$ ,  $^{208}\text{Pb}$ , and  $^{238}\text{U}$ . *Phys Rev C*, **68**: p. 024317, 2003.
- [37] T. Blaich, T. Elze, H. Emling, H. Freiesleben, et al. A large area detector for high-energy neutrons. *Nuclear Instruments and Methods in Physics Research Section A: Accelerators, Spectrometers, Detectors and Associated Equipment*, **314**: p. 136, 1992.
- [38] H. T. Johansson. *The DAQ always runs*. Licenciate thesis, Chalmers University of Technology, 2006.
- [39] S. Altstadt.  *$^{13,14}\text{B}(n,\gamma)$  via Coulomb Dissociation to Constrain the Astrophysical  $r$ -Process*. Ph.D. thesis, University of Frankfurt, 2014.
- [40] M. Wang, G. Audi, A. Wapstra, F. Kondev, et al. The Ame2012 atomic mass evaluation. *Chinese Physics C*, **36**: p. 1603, 2012.
- [41] D. Rossi. *Investigation of the Dipole Response of Nickel Isotopes in the Presence of a High-Frequency Electromagnetic Field*. Ph.D. thesis, Johannes Gutenberg-Universität Mainz, 2010.
- [42] V. Panin. *Fully Exclusive Measurements of Quasi-Free Single-Nucleon Knockout Reactions in Inverse Kinematics*. Ph.D. thesis, Technical University of Darmstadt, 2012.

- [43] D. Sohler, M. Stanoiu, Z. Dombrádi, F. Azaiez, et al. In-beam  $\gamma$ -ray spectroscopy of the neutron-rich nitrogen isotopes N19-22. *Phys Rev C*, **77**: p. 044303, 2008.
- [44] G. Audi, A. Wapstra, and C. Thibault. The Ame2003 atomic mass evaluation: (II). Tables, graphs and references. *Nuclear Physics A*, **729**: p. 337, 2003. The 2003 {NUBASE} and Atomic Mass Evaluations.
- [45] [http://physics.nist.gov/cgi-bin/cuu/Value?mn|search\\_for=neutron+mass](http://physics.nist.gov/cgi-bin/cuu/Value?mn|search_for=neutron+mass), visited at 03.04.2014.
- [46] <http://root.cern.ch/root/html/TH1.html>, visited at 03.04.2014.
- [47] G. Baur, C. Bertulani, and H. Rebel. Coulomb dissociation as a source of information on radiative capture processes of astrophysical interest. *Nuclear Physics A*, **458**: p. 188 , 1986.
- [48] S. Typel and G. Baur. Higher order effects in electromagnetic dissociation of neutron halo nuclei. *Phys Rev C*, **64**: p. 024601, 2001. Equivalence of reactions induced by virtual and real photons.

## **Erklärung**

Diese Arbeit wurde am Institut für Kern- und Teilchenphysik der Technischen Universität Dresden unter wissenschaftlicher Betreuung von Prof. Dr. Kai Zuber und am Institut für Strahlenphysik des Helmholtz-Zentrum Dresden-Rossendorf unter der Leitung von PD Dr. Daniel Bemmerer und Dr. Andreas Wagner im Zeitraum von November 2010 bis Juni 2014 erarbeitet.

Ich versichere, dass ich die vorliegende Arbeit ohne unzulässige Hilfe Dritter und ohne Benutzung anderer als der angegebenen Hilfsmittel angefertigt habe; die aus fremden Quellen direkt oder indirekt übernommenen Gedanken sind als solche kenntlich gemacht. Die Arbeit wurde bisher weder im Inland noch im Ausland in gleicher oder ähnlicher Form einer anderen Prüfungsbehörde vorgelegt.

Es fanden keine früheren erfolglosen Promotionsverfahren statt.

Ich erkenne die Promotionsordnung der Fakultät Mathematik und Naturwissenschaften an der Technischen Universität Dresden an.

Dresden, den 12. Dezember 2014

Marko Röder